FACULTY
OF MATHEMATICS
AND PHYSICS
Charles University

DOCTORAL THESIS

Yuliia Kosto

Study of cerium oxide thin films for biosensing applications

Department of Surface and Plasma Science
Supervisor of the doctoral thesis: Prof. RNDr. Vladimír Matolín, DrSc.
Study program: Physics
Study branch: F5 - Physics of Surfaces and Interfaces

Prague 2021

Acknowledgments

I would like to express deep gratitude to my supervisor, Vladimír Matolín, and head of the Nanomaterials group, Iva Matolínová, for their support and mentoring during my study, and also for giving an opportunity to travel to various laboratories to conduct the measurements.

My special thanks go to Nataliya Tsud, who spent a vast amount of time with me discussing the experiments and, following, the obtained results. Thank you for your guidance, patient sharing of your knowledge, and support, both scientific and personal. I appreciate it a lot.

I would like to thank Mykhailo Vorokhta and Filip Dvořák, who helped me with my first steps in our department and provided a friendly environment in the NAP XPS laboratory.

Many thanks to Stefano Franchi, Tomáš Skála, Peter Matvija, and Viacheslav Kalinovych, who accompanied me during long experiments at Materials Science Beamline. Also, I thank Ivan Khalakhan for SEM and AFM measurements and Yurii Yakovlev for excellent sample preparation.

Furthermore, I would like to thank the Electrochemistry group from the University of Bologna, especially Alessandra Zanut and Giovanni Valenti, for their insightful consultations about the electrochemical part of the current work.

And last but not least, I am deeply grateful to my family, who believes in me no matter what, for everyday care and love. And to my friends for letting me know that you are always there, ready to cheer me up.

I declare that I carried out this doctoral thesis independently, and only with the cited sources, literature and other professional sources. It has not been used to obtain another or the same degree.

I understand that my work relates to the rights and obligations under the Act No. 121/2000 Sb., the Copyright Act, as amended, in particular the fact that the Charles University has the right to conclude a license agreement on the use of this work as a school work pursuant to Section 60 subsection 1 of the Copyright Act.

In . . . . date . . . .

Author’s signature

Title: Study of cerium oxide thin films for biosensing applications
Author: Yuliia Kosto
Department: Department of Surface and Plasma Science
Supervisor: Prof. RNDr. Vladimír Matolín, DrSc.

Abstract:

The presented scientific work was conducted in two main directions. The first one is an investigation of the simple biomolecules (glycine and sarcosine) bonding to cerium oxide model films by surface science techniques: photoelectron and near-edge X-ray absorption spectroscopies. Adsorption chemistry and thermal stability of the molecules on the oxides were studied in relation to the oxidation state of ceria cations, film morphology, and molecular deposition method. The oxygen vacancies in the oxide were shown to affect the adsorption geometry of glycine and stimulate molecular decomposition. The polycrystalline oxide morphology provided stabilizing effect on the glycine adlayer. Sarcosine deposited in vacuum formed densely packed adlayer with the molecules directed outwards. Interestingly, the results revealed that molecular film deposited from the aqueous solution, in contrast to deposition in vacuum, induces continuous reduction of the cerium oxide during thermal annealing. The second part is a study of polycrystalline cerium oxide thin films as an electrode for electrochemical and electrochemiluminescent detection of hydrogen peroxide and sarcosine, respectively. We confirmed the enzymatic properties of the cerium oxide in electrochemical oxidation of hydrogen peroxide. For sarcosine detection, the polycrystalline CeO_2 film was demonstrated to be an efficient cathode material for the model electroluminescent sensing systems.

Keywords:
Cerium oxide, biosensor, hydrogen peroxide, amino acid, photoelectron spectroscopy.

Název práce: Studium tenkých vrstev oxidu ceru pro biosenzorické aplikace
Autor: Yuliia Kosto
Katedra: Katedra fyziky povrchů a plazmatu
Vedoucí disertační práce: Prof. RNDr. Vladimír Matolín, DrSc.

Abstrakt:

Prezentovaná vědecká práce probíhala ve dvou hlavních směrech. Prvním z nich je zkoumání vazby jednoduchých biomolekul (glycin a sarkosin) na modelových vrstvach oxidu ceru povrchovými technikami: fotoelektronovou spektroskopií a absorpční rentgenovou spektroskopií v blízkosti hrany. Byla studována adsorpční chemie a tepelná stabilita molekul na oxidech v závislosti na oxidačním stavu kationů ceru, morfologii vrstev a na způsobu depozice molekul. Ukázalo se, že kyslíkové vakance v oxidu ovlivňují adsorpční geometrii glycinu a stimulují rozklad molekuly. Morfologie polykrystalického oxidu vykazovala stabilizační účinek na adsorbované vrstvě glycinu. Sarkosin deponovaný ve vakuu vytvořil hustě uspořádanou adsorbovanou vrstvu s molekulami směřujícími ven. Zajímavou skutečností plynoucí z naměřených výsledků je fakt, že molekulární vrstva nanesená z vodného roztoku, na rozdíl od depozice ve vakuu, indukuje kontinuální redukci oxidu ceru během tepelného žíhání. Druhým směrem této práce je studium polykrystalických tenkých vrstev oxidu ceru jako elekrody pro elektrochemickou a elektrochemiluminiscenční detekci peroxidu vodíku a sarkosinu. Potvrdili jsme enzymatické vlastnosti oxidu ceru při elektrochemické oxidaci peroxidu vodíku. Pro detekci sarkosinu bylo prokázáno, že polykrystalická vrstva CeO_2 je účinným katodovým materiálem pro modelové elektrochemiluminiscenční senzorické systémy.

Klíčová slova:
Oxid ceru, biosensor, peroxid vodíku, aminokyselina, fotoelektronová spektroskopie.

Contents

1. Introduction

Recently, inorganic nanomaterials have attracted a lot of attention in biological applications. They are already used in various medical diagnostics, both *in vitro* and *in vivo*. They made possible a single cell analysis, are used in imaging, in biosensors in general, and in micro fluids testing in particular. In therapy, they are actively applied in targeting drug delivery. Nanomaterials offer a route for further development of personalized medicine, which might assist in establishing a suitable treatment for each patient according to his individual profile.

One of the promising materials for applications in nanomedical field is cerium oxide. Cerium oxide is well-known mainly for its catalytic properties, oxygen storage capacity, and ability to quickly change its oxidation state from Ce^{4+} to Ce^{3+} and vice versa in response to environmental conditions. It is actively used in numerous industrial applications such as solid electrolyte fuel cells,[1,2] gas sensors,[3] UV screens,[4] solar cells,[5] catalysis,[6,7] etc. A few decades ago, cerium oxide has also attracted attention in biomedical field. It was discovered that ceria nanoparticles (NPs) could mimic properties of several natural enzymes that appear in mammals' bodies and have a vast potential to be used as an antioxidative agent in treatment of various severe diseases such as some types of cancer, Alzheimer's, and Parkinson's diseases, diabetes, etc.[8,9] It was shown that CeO_2 NPs provided good compatibility with biological systems, but other studies revealed that such materials could be hazardous and toxic for the living cells.[10–12] Nature of different behavior of CeO_2 NPs in different bio-related systems is not completely clear yet. Thus, understanding the interaction between cerium oxide and biological materials is necessary for further knowledge-driven development of nanomaterials that are safe for biomedical applications. Since the real systems are complicated and, thus, difficult to analyze, the simplified model systems, e.g., single biomolecules bound under controlled conditions to inorganic surfaces at a different level of complexity, are often considered. It formed the basis of the research approach applied in the current work. Another area of cerium oxide application is sensor systems in biomedicine. It has been shown that cerium oxide can be used as a sensing material for detection of glucose,[13–15] hydrogen peroxide,[16–18] cholesterol,[19] tributyrin,[20] for diagnosis of colorectal cancer.[21] Since the CeO_2 electrode is placed in biological environment that can influence the oxide properties, understanding the ceria-organic interface is essential.

1.1. Biosensing setups with the use of cerium oxide

In recent years, development of biological sensors has received a lot of attention in the fields of nanotechnology and materials science. The main effort was directed to the fabrication and characterization of inorganic materials for novel bioelectrodes with well-defined morphology and physicochemical properties in reactions with biomolecules and other derivatives of bio recognition events. Electrochemical techniques are well-developed analytical methods widely used for biosensor operation due to their high sensitivity, fast time response, simplicity, and accurate determination of specific analytes (cholesterol, glucose, urea, hydrogen peroxide, etc.).[22] Cerium oxide is among the most promising materials for biological sensing devices. It possesses many bio-related properties like catalytic activity, good biocompatibility, oxygen storage capacity, high isoelectric point, electron transfer capability, etc.[9,23]

Enzymes are often applied as the transduction elements, which promote the electrochemical detection of biochemical compounds. The advantages of sensing with enzymes are high efficiency, resolution, and specificity, but enzymes' catalytic activity is unstable as a function of time and sensitive to environmental conditions. Recently, cerium oxide has been actively used for glucose sensor development and improvement. Moumene et al. have reported an enzymatic glucose electrochemical sensor based on pulsed laser deposited nanoceria with glucose oxidase (GOx) physisorbed on an electrode surface.[14] Ansari et al. have fabricated bioelectrodes for glucose detection by deposition of sol-gel derived nanosized CeO_2 films on a gold electrode followed by immobilization of GOx.[15] It demonstrated linearity in the range 50 – 400 mg/dl of glucose. The same group has reported a cholesterol biosensor constructed by cholesterol oxidase (ChOx) immobilization on sol-gel derived nanostructured cerium oxide film prepared on an indium-tin-oxide coated glass substrate.[19] The electrode’s activity has been evaluated as a function of pH, and the data revealed the highest activity at pH 7.0, which corresponded to the natural structure of ChOx. Patil et al. have developed a mediator-less enzymatic glucose biosensor based on a cerium oxide nanorods film electrophoretically deposited onto an indium-tin-oxide coated glass substrate.[24] The electrode demonstrated fast response time and linearity in the range 2 – 26 mM of glucose. Saha et al. have investigated nanoporous ceria thin films deposited onto Pt coated glass plates with immobilized GOx for glucose detection.[13] Results showed a linear range for glucose detection from 25 to 300 mg/dl and good stability of the bioelectrode.

An alternative approach to enzyme chemistry, based on different inorganic materials possessing enzyme-mimetic properties, is being actively developed and investigated. Such materials are robust to stringent conditions, cheap, and have high operational stability, but reveal lower sensitivity and selectivity in comparison with enzymatic electrodes.[25] In the last decades, it has been found found that nanostructured metal oxides exhibit biocatalytic properties and could be used as artificial enzymes or nanozymes.[26,27] The Pd-CeO_2 platform has been investigated as a biosensing electrode, and electrocatalytic activity toward ascorbic and uric acids, glucose, and dopamine was detected.[28] Cerium oxide-based bioelectrodes sensitive to sulfamethoxazole (SMX) in food,[29] triglyceride,[30] butyrin,[20] ochratoxin-A[31] have been investigated. An electrochemical sulfamethoxazole biosensor based on a nano-CeO_2/chitosan composite demonstrated very good selectivity, sensitivity, and stability during determination of SMX in egg, milk, and honey samples.[29]

This work will show that polycrystalline cerium oxide thin film prepared by magnetron sputtering on a glassy carbon substrate can be used as an electrode for electrochemical detection of hydrogen peroxide. That is a distinct preparation method of the cerium oxide-based working electrode, since in the majority of the mentioned above researches the electrode was prepared on a base of CeO_2 nanoparticles or nanorods that were further immobilized on the conductive surface. It will also be shown that the cerium oxide electrode prepared in the same way can be used for detection of sarcosine by electrochemiluminescence (ECL) technique.

1.2. Electrochemical detection of hydrogen peroxide and sarcosine

Hydrogen peroxide

One of the analytes chosen for electrochemical detection by cerium oxide electrode in the current work is hydrogen peroxide. The annual production of hydrogen peroxide in the world is estimated to be 4.5 million metric tons in 2020 year, and is predicted to reach 5.7 million metric tons by 2027.[32] Detection of hydrogen peroxide is vital since it is involved in numbers of applications in chemical industry, electronics, waste treatment, metal processing, food industry, medicine, etc. It is also a product of many biochemical processes in living organisms, and in higher concentrations it creates free radicals and induces oxidation of molecules, leading to oxidative stress and inflammations.[33] Hydrogen peroxide is a source of hydroxyl radicals – the second strongest oxidant after fluorine. Thus, it is of great importance to develop and construct simple, cheap, fast, sensitive, and precise devices for H_2O_2 detection.[34] The most reliable and easy way for H_2O_2 detection is electrochemical, and several such sensors have been reported.

Frontera and co-workers fabricated an electrode for H_2O_2 detection by modifying a planar screen-printed carbon electrode by TiO_2/CNTs/Pt nanocomposite dispersed in Nafion solution.[35] It works at a low potential of 0.3 V and can minimize interference with other oxidizable species. The sensor revealed good sensitivity (120 μA mM^{-1} cm^{-2}), linearity from 70 μM to 6 mM, and detection limit lower than 5 μM. Mehta et al. developed a 3-terminal amperometric enzyme-free hydrogen peroxide sensor with Au working electrode covered by cerium oxide nanoparticles (NPs) synthesized by a water-in-oil microemulsion technique.[36] The sensor showed linearity in the range from 1 μM to 30 mM H_2O_2. Ansari et al. reported a bioelectrode for hydrogen peroxide detection based on horseradish peroxidase (HRP) enzyme immobilized on nanosized cerium oxide deposited onto an indium-tin-oxide substrate.[18] The electrode revealed linearity in the range 1 – 170 μM.

It has been reported that cerium oxide could also be used as a sensing material for H_2O_2 detection. Neal et al. have studied an enzyme-free cerium oxide NPs-based electrochemical sensor for H_2O_2 detection.[17] The catalytic response to picomolar concentrations of H_2O_2 of NPs with different Ce^{3+}/Ce^{4+} ratio has been investigated. The electrode demonstrated an ultra-low detection limit (around 0.1 pM) and linear range from 0.1 pM to 0.1 μM. Nanosized structures with a lower Ce^{3+}/Ce^{4+} ratio have been shown to reveal higher electrochemical activity, which is in line with results of a catalase assay standard test for evaluation of H_2O_2 neutralization by the same ceria NPs.[17]

The cerium oxide electrodes modified by enzymes have been reported to reveal a good sensitivity and selectivity toward H_2O_2.[18,37,38] However, due to previously mentioned reasons, such as expensive production of enzymes, complex procedure of their immobilization on the electrode, and short lifetime of the enzymes, there is a need in development of enzyme-free electrodes.

There are several works reporting creation of the exclusively inorganic-based cerium oxide electrodes for H_2O_2 detection. One of them is single-walled carbon nanohorns modified cerium oxide (CeO_2-SWCNHs).[39] This electrode has been shown to reach sensitivity of 160 μA cm^{-2} mM^{-1} and remained 82% of its activity after two weeks.[39] Another research has reported the cerium oxide-based electrode that was prepared by using CeO_2 nanoparticles synthesized from two different capping agents, fructose and hexamethylene-tetra-amine (HMTA), and sprayed onto ITO substrate.[40] Both types of electrodes revealed good stability (in time and temperature) and reproducibility of the results. The amperometric selectivity test was done with several interfering materials (acetic acid, lactic acid, glucose, sucrose), and the electrodes didn't show any detectable response. Sensitivity of the CeO_2-fructose and CeO_2-HMTA was reported to be 9.6 and 21.13 μA cm^{-2} mM^{-1}, respectively.

Sarcosine

Another part of this thesis is dedicated to the electrochemiluminescent detection of sarcosine using cerium oxide as a working electrode. Sarcosine is known to be a potential marker for prostate cancer detection.

According to World Health Organization, prostate cancer (PCa) is the fourth most commonly occurred cancer overall and the second in men part of the Earth human population. During the lifetime, it develops in 1 man of 9, the more likely in older (over 65 years) African-American men. Nowadays, the PCa screening is done through the prostate specific antigen (PSA) testing. The PSA appears in minor concentrations when prostate is in a normal state and notably increases when PCa develops. The amount of PSA in serum depends on the size of the tumor and stage of cancer. However, the PSA test may often lead to false-positive results since the PSA concentration can be increased in serum of men with benign prostatic hyperplasia or prostatitis. These results decrease the test reliability.[41] Thus, there is a need to find alternative biomarkers for more accurate PCa diagnosis. In the last decades, non-invasive urine tests for cancer metabolites became a promising direction for PCa screening. It has been found that sarcosine can be used as a biomarker molecule for PCa detection since its concentration in urine increases during cancer progression.[42,43] Its role in the PCa progression is actively studied. It leads to a need for sarcosine sensor development.

A high-performance chromatography is generally used for sarcosine detection.[44] There are many reports of enzyme-linked assays for sarcosine detection in urine, blood, and serum samples. Sarcosine oxidase is the most actively used enzyme in sarcosine detection assay kit.[45] One study reported indirect colorimetric determination of sarcosine by detection of H_2O_2 that was catalyzed by 3,3′,5,5′-tetramethylbenzidine with palladium nanoparticles as a catalyst instead of horseradish peroxidase.[46] However, determination of sarcosine in urine samples is challenging since it requires discrimination of sarcosine molecules from the rest of the organic matrix. Previous work proposed a direct binding tetraphosphonate cavitand system on Si substrate for fluorescence detection of sarcosine.[47] The supramolecular complex is able to recognize sarcosine and glycine in water and urine and is a good alternative to immunoassays. A similar supramolecular approach was used by Valenti et al.[48] for electrochemiluminescent detection of sarcosine with good selectivity in a concentration range used for medical diagnosis of PCa. They used sarcosine as a co-reactant in ECL systems with $(Ru(bpy)_3)^{2+}$ as a luminophore.[48]

1.3. Model studies of glycine and sarcosine films on inorganic surfaces

In the current work, we studied adsorption chemistry and thermal stability of the two similar molecules on the cerium oxide substrates: glycine and sarcosine. Glycine (NH_2-CH_2-COOH) is the simplest proteinogenic amino acid and is an example of biomolecule consisting of α-carbon, carboxylic and amino functional groups only (see Fig. 1.3.1 a). In addition to the important function of glycine as a building block of proteins in living organisms, its adsorption on metal or oxide films has applications in surface functionalization for solar cell,[49,50] sensing systems for Cu^{2+} ions detection,[51] and as a corrosion inhibitor.[52] The second selected molecule is sarcosine (CH_3-NH_2-CH_2-COOH), also known as N-methylglycine (Fig. 1.3.1 b). This molecule was chosen as a derivative of glycine. Apart from the model study of molecule/oxide substrates prepared in well-defined conditions by surface science techniques, this molecule was considered as an analyte for an ECL sensing system with the use of polycrystalline cerium oxide electrode. Sarcosine is a byproduct of synthesis and degradation of glycine. Structure of the molecule is similar to glycine, but with the additional methyl group connected to the amino nitrogen. As it was previously mentioned, sarcosine is a promising marker for prostate cancer diagnosis at early stages.[53,54] Sarcosine is also used in treatment of schizophrenia and depression and as an ingredient in cosmetics. To our knowledge, there are no PES studies done on characterization of sarcosine molecules adsorbed on inorganic substrates.

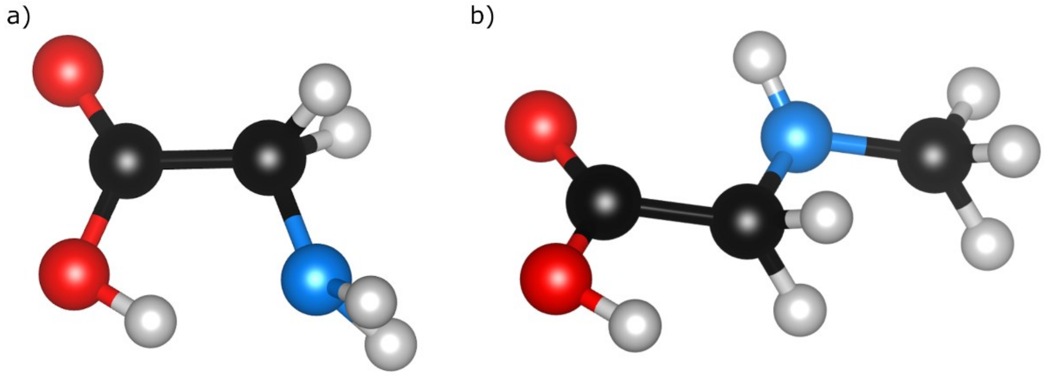

__Fig. 1.3.1.__ a) Glycine and b) sarcosine molecules in a neutral state. Black, red, blue, and light gray spheres correspond to carbon, oxygen, nitrogen, and hydrogen atoms, respectively.

At the same time, glycine is a classical model molecule for the basic research in surface science due to the simple structure, stability, and similarity to the small organic molecules (e.g., acetic acid, CH_3-COOH, etc.). The primary objective of a model study in ultra-high vacuum (UHV), in which molecules are deposited from the vapor phase on a substrate, is the characterization of the bonding of the molecule to a surface, with the aim to define the geometry, stability, and adsorption energy. Numerous studies of the glycine adsorption on the well-defined substrates have been published, among them surfaces of metals[55–59] and oxides.[60–62] On Cu(111), Cu(110), and Cu(100), independent of the surface orientation, glycine undergoes deprotonation at 25 °C adsorbing upward in unidentate coordination at saturation coverage via one carboxylic oxygen accompanied by the formation of intermolecular hydrogen bonds. Annealing to 125 °C changes considerably the glycine adsorption geometry in which bonding occurs via two oxygen and nitrogen atoms with a molecular plane parallel to the surface.[55–57] For the Pt(111) and Pd(111) surfaces, saturation monolayer of glycine is formed by molecules in zwitterionic phase bound via carboxylic and amino groups.[58,59]

The glycine adlayer on (110) and (011) surfaces of TiO_2 at 25 °C consists of zwitterionic ($^+NH_3$-CH_2-COO^-) and deprotonated (NH_2-CH_2-COO^-) molecules. The protonated molecules are less stable and converted to the dissociated phase after annealing at higher temperatures.[60,61] The glycinate adlayer on TiO_2 is formed through two oxygen atoms of the carboxylate group bridging two Ti atoms, while the dissociated proton binds to oxygen atom on the surface resulting in an additional OH group; the amino group is directed upward from the surface and is not involved in the interface.[60–62] The DFT calculations[62] have confirmed that glycine bonding to the TiO_2(110) surface is more stable in dissociated anionic form than in zwitterionic. Lausmaa et al.[63] have also argued that the appearance of the oxygen molecules on the TiO_2 surface does not play any significant role in the glycine adsorption chemistry and dissociation in course of the thermal treatment by TDS study. Glycine adsorption geometry on Al_2O_3/NiAl(110)[64] has been shown to be similar to the case of TiO_2(110). The DFT calculations of glycine adsorption on the Cr_2O_3(0001) surface[65] have reported the formation of the glycinate adlayer up to 1 ML coverage through carboxyl and amino groups binding to surface Cr atoms. The molecules lie parallel to the surface at low coverage and bend upward at high coverage. In case of Cr_2O_3(0001) functionalized with OH groups,[66] the glycine molecules are adsorbed mainly in zwitterion form at low and saturation coverages.

In this work, we present results of the study of thermal stability and adsorption chemistry and geometry of glycine and sarcosine adlayers on cerium oxide thin films of different stoichiometry and surface morphology.

One of the closely related to glycine molecules is histidine. The model study on histidine, one of the principal amino acids, adlayers on the cerium oxide films of different oxidation state[67] and morphology[68] was previously done by our group. On the well-ordered $CeO_2(111)/Cu(111)$ oxide, histidine, deposited in UHV, has been shown to adsorb via the deprotonated carboxylic group, the imino nitrogen atom of the imidazole (IM) ring and the α-amino group at 25 °C. The deprotonation of the IM amino nitrogen occurred to be thermally induced and dependent on the surface concentration of the Ce^{4+} cations. On a stoichiometric CeO_2 film, clear orientation of the molecule with the imidazole ring lying almost parallel to the surface was observed, while on the partially reduced cerium oxide, histidine was bonded to the surface in anionic form without the clear orientation to the surface. A charge exchange between the histidine molecule and the oxide has been connected with the increased amount of the Ce^{3+} centers on the surface[67]. Later, it has been demonstrated that on the polycrystalline CeO_2 film,[68,69] histidine deposited both from solution and in UHV binds via the carboxylic acid group only with the imidazole ring involved in the intermolecular hydrogen network.

Acetic acid adsorption and reactions on $CeO_2(111)$ and CeO_x ($1.5<x<2$) oxide films[70] are other closely related systems. The formation of acetate adsorbed species together with surface hydroxyl groups has been observed at 25 °C with further decomposition to mainly CO, CO_2, ketene, and water at elevated temperatures. Acetates on the $CeO_2(111)$ and CeO_x oxides are stable up to 150 and 175 °C, respectively. Annealing at 425 °C stimulates complete desorption of adsorbates from $CeO_2(111)$ and leaves some residual carbon on the CeO_x oxide. The C-O bond scission has been proposed as an explanation of the CeO_x film reoxidation and formation of strongly adsorbed C_2H_x species, observed as a residual C 1s signal.

To the best of our knowledge, there are no other studies on glycine and sarcosine adsorption chemistry on cerium oxide surfaces.

1.4. Goal and structure of the thesis

In the current work, two different approaches were applied to the investigation of cerium oxide thin films for biosensing applications: the study of planar molecule/cerium oxide systems in vacuum with the use of surface science technique (Chapter 3.1) and electrochemical characterization of the model cerium oxide working electrodes in reaction with hydrogen peroxide and sarcosine (Chapter 3.2). The first one was aimed to provide and extend to already existing knowledge about simple biological molecules' interaction with cerium oxide. Two amino acids were chosen as model molecules: glycine, the simplest proteinogenic amino acid, and sarcosine, a byproduct of glycine synthesis with a high potential in medical applications as a marker in diagnostics of prostate cancer. The study was done on cerium oxide films of different structure, chemical state, composition, and morphology. Influence of the molecular deposition technique on the adlayer bonding and stability on the oxide film was investigated as well. It is a fundamental research that aims to provide basic information within a bottom-up strategy for further better understanding of more complex systems where the biomolecules' bonding to the inorganic materials is expected. The second approach is dedicated to the potential application of cerium oxide thin films prepared by radiofrequency magnetron sputtering in sensing systems. It will be shown that polycrystalline cerium oxide films could be used as an electrode for electrochemical detection of hydrogen peroxide (Chapter 3.2.1) and for ECL detection of sarcosine (Chapter 3.2.2).

The experimental results of the work are presented in four chapters. The Chapter 3.1.1 is devoted to glycine adsorption on cerium oxide films of different stoichiometry and composition studied by means of synchrotron radiation photoelectron spectroscopy (SRPES), and near-edge X-ray absorption fine structure spectroscopy (NEXAFS). The effect of the glycine adlayers on the oxidation state of cerium oxide cations was monitored by resonant photoelectron spectroscopy (RPES) and X-ray photoelectron spectroscopy (XPS) using an ordinary X-ray source. The ordered stoichiometric $CeO_2(111)/Cu(111)$, partially $CeO_{1.7}(111)/Cu(111)$ and fully reduced $Ce_2O_3(111)/Cu(111)$ surfaces, and mixed oxide $Ce_6WO_{12}(100)/W(110)$ prepared *in situ* were chosen as the model substrates. Glycine was deposited onto the oxide films at 25 °C by evaporation from a Knudsen cell in UHV. The glycine atoms' involvement in the interface formation on different oxides together with thermal stability of the molecular adlayers were analyzed. The presence of oxygen vacancies in the oxide film was shown to play a crucial role in the adsorption chemistry of glycine. In the Chapter 3.1.2, the results on glycine and sarcosine bonding to polycrystalline cerium oxide films prepared *ex situ* by nonreactive magnetron sputtering are presented. The deposition of the molecules was done both by evaporation in vacuum and by deposition from the aqueous solution under inert atmosphere in a glove bag. Adsorption chemistry and thermal stability of the molecules and their effect on the oxidation state of the surface cations were investigated by SRPES, RPES, XPS, and NEXAFS. The last two chapters (Chapters 3.2.1 and 3.2.2) of the results section are dedicated to application of the cerium oxide films as electrodes for detection of hydrogen peroxide and sarcosine using electrochemical-based techniques. The surface chemistry of the electrodes was characterized by SRPES and XPS, the structure and morphology by SEM and AFM. The sensing properties of cerium oxide films for hydrogen peroxide detection were investigated by cyclic voltammetry (CV) and chronoamperometry (CA). The ability of polycrystalline cerium oxide to detect sarcosine was studied by means of the ECL technique.

2. Description of the techniques and experimental details

In this chapter, we give a brief description of the experimental techniques used in the work. The principles of the synchrotron radiation photoelectron and near edge X-ray absorption fine structure spectroscopies, low energy electron diffraction, as well as secondary electron and atomic force microscopies, are addressed. The classical surface science approach was combined with *ex situ* electrochemistry for the comprehensive characterization of the model systems for biosensing applications of cerium oxide. The cyclic voltammetry, chronoamperometry, and electrochemiluminescence, three basic electrochemical methods are described here. The details on sample preparation and data analysis are also presented.

2.1. Photoelectron spectroscopy

Photoelectron spectroscopy (PES) is the principal technique used in the current work for characterization of model systems. Its principle is based on the photoelectric effect that was discovered by Hertz in 1887 and described by Einstein in 1905. Electrons, called the photoelectrons, are excited by the electromagnetic radiation, then emitted from the matter to vacuum, and detected. The photoemission process (see Fig. 2.1.1 a) can be described by a three-step model, which includes: 1) absorption of the photon and excitation of the electron with binding energy E_b at the specific electronic level, 2) traveling of the excited electron in the matter to its surface, 3) escape of the electron through the surface barrier to vacuum overcoming the work function of the material W with resulting kinetic energy E_{kin} and its detection by the analyzer. The change of the kinetic energy and momentum of the photoelectrons provides information about the chemical composition and electronic structure of the investigated material. Relation between the binding energy and detected kinetic energy of the emitted photoelectron is given by the equation:

$$E_{kin} = h\nu - E_b - W_S, \qquad \textbf{Eq. 1}$$

where $h\nu$ is the energy of the incident photons and W_S is a work function of the spectrometer used in the measurements. A typical PES spectrum (see Fig. 2.1.2) represents an intensity distribution of photoelectrons with respect to their binding energy calculated according to the **Eq. 1**. In other words, intensity of the detected electrons with kinetic energy E_{kin} provides information about their density of states (DOS) at the specific electronic level corresponding to binding energy E_b.

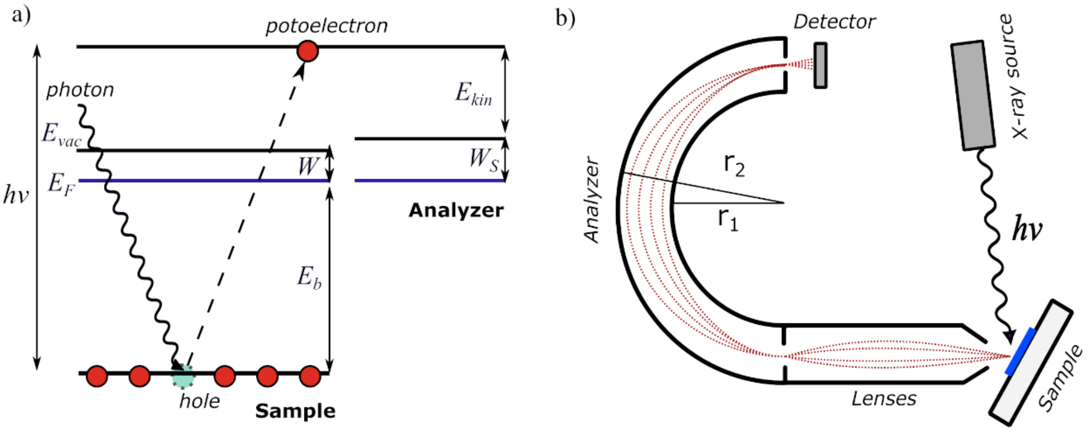

Fig. 2.1.1. *Schematic illustration of the a) photoemission process and b) PES experimental setup.*

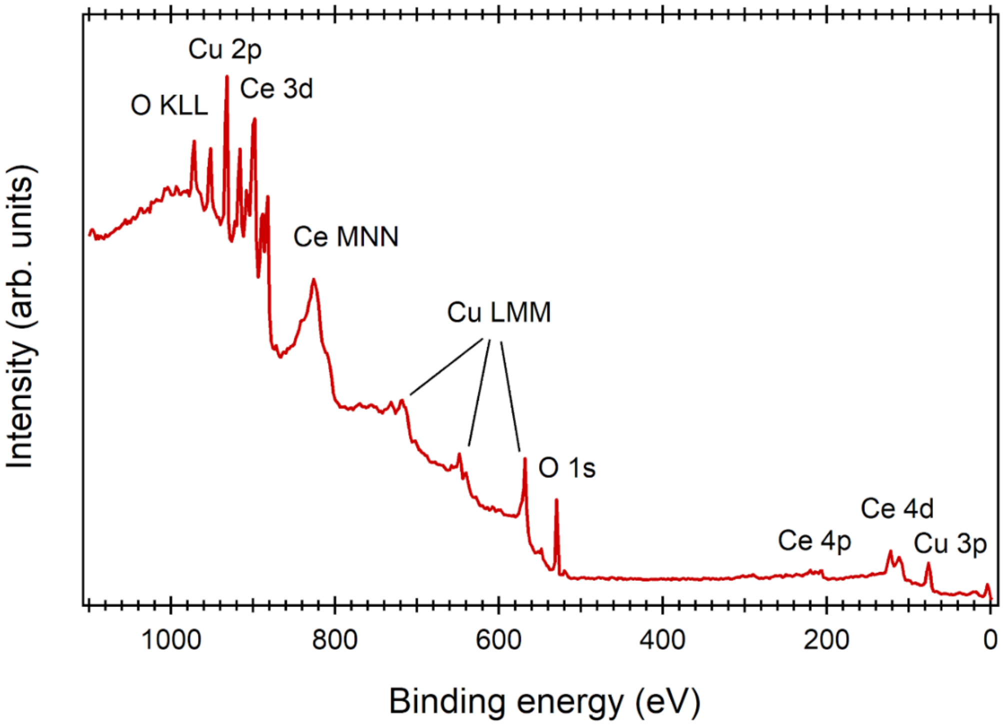

Fig. 2.1.2. *Survey PES spectrum of cerium oxide thin film prepared on Cu(111) substrate by e-beam vapor deposition. Photon energy 1486.6 eV.*

A survey PES spectrum from the clean cerium oxide thin film deposited on Cu(111) is presented in the Figure 2.1.2. Each photoelectron peak, e.g. O 1s, Cu 2p, Ce 3d, etc., corresponds to a specific energy level labeled *1s*, *2p*, *3d*, etc. accordingly to quantum numbers

nl_j of the original electron shell. Here, n is the principal quantum number, l is the angular momentum quantum number associated with the s, p, d, and f orbitals, and j is the total momentum quantum number. The total momentum number j equals the absolute value of the sum of the angular momentum number l and the spin momentum number s. The spin momentum of $+1/2$ or $-1/2$ leads to the spin-orbit splitting and appearance of doublets in the spectra (e.g. Cu 2p, Ce 3d, Ce 4d, etc.), i.e. cases when the angular momentum number l is different from zero. Otherwise, there are singlets (e.g. O 1s, C 1s, etc.). Besides the core level peaks, there are other essential components in the PES spectrum - Auger peaks (O KLL, Ce MNN, and Cu LMM in Fig. 2.1.2). The Auger electrons are created in the process that includes filling a hole, created in the core level after photoelectron emission, by an electron from the higher level. The released energy can be used for excitation and emission of the third electron called Auger electron. Thus, the kinetic energy of the Auger electrons is independent of the incident photon energy and is determined by an energy difference between involved electronic levels. The stepwise background of the PES spectrum is created by the secondary electrons, which undergo multiple inelastic collisions on their route to the vacuum. The background has to be subtracted during the data analysis.[71]

The basic PES experimental setup (Fig. 2.1.1 b) consists of the electromagnetic radiation source, grounded sample, and the electron energy analyzer with a detector. Depending on the photon source, the commonly applied PES techniques are X-ray photoelectron spectroscopy (XPS), ultraviolet photoelectron spectroscopy (UPS), and synchrotron radiation photoelectron spectroscopy (SRPES). The photon sources for laboratory PES experiments employ X-rays provided by electron bombardment of such materials as Al, Mg, Cr, Zr, Ag, etc. The Al/Mg X-ray tube for XPS, which generates photons of energies 1486.6 eV (Al $K\alpha_{1,2}$) and 1253.6 eV (Mg $K\alpha_{1,2}$), became the most commonly used. A gas discharge lamp of the UPS spectrometer is used for generation of the photons in the ultraviolet range. More sophisticated synchrotron facilities provide a possibility to use the SRPES technique with a wide range of monochromatic highly intense polarized X-rays: from soft (10-1000 eV) to hard (up to tens of keV) radiation. The possibility to choose the photon energy allows to analyze the DOS and/or molecular orbitals in the valence region of the surface layers as well as core atomic levels in the bulk material.

The photoelectrons emitted from the surface are collected depending on their kinetic energy. Nowadays, a hemispherical analyzer is the most widely used for this purpose (Fig. 2.1.1 b). Before entering the hemispheres, electrons are decelerated by retarding electric field to the energy E_0 called pass energy. The two hemispheres are charged in a way that only electrons with energy E_0 can reach detector. Potential difference between them equals to:

$$U_1 - U_2 = \frac{E_0}{e}\left(\frac{r_2}{r_1} - \frac{r_1}{r_2}\right) \qquad \textbf{Eq. 2}$$

where e is the elementary charge, r_1 and r_2 are radii, and U_1 and U_2 are applied potentials to the inner and outer hemispheres, respectively. There are two modes of measurement: the fixed retard ratio (FRR) and the fixed analyzer transmission (FAT). The FRR operation provides data with constant E_{kin}/E_0 ratio and reduced background at low kinetic energies, it is generally applied for the Auger spectroscopy. In the FAT mode, the photoelectrons are retarded to the same pass energy E_0 which remains constant during acquisition. The constant resolution for the whole spectrum is the most prominent characteristic feature of this mode which turned out to be a huge advantage for the qualitative and quantitative chemical analysis of surfaces with the use of PES techniques.[72]

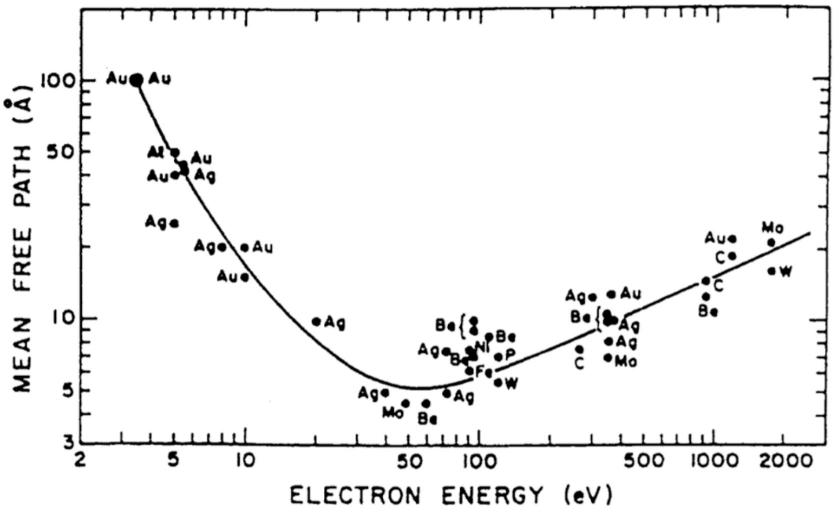

Fig. 2.1.3. The universal curve of the IMFP of chemical elements as a function of photoelectron kinetic energy taken from Ref.[73]

Surface sensitivity of the PES technique, i.e. the sampling depth, is defined by the inelastic mean free path (IMFP) of the electrons in a given material. Only photoelectrons that do not undergo any inelastic collisions on the way to the vacuum provide specific information on the surface electronic structure and contribute to the intensity of the corresponding core levels or valence states. The IMFP value of electrons in different materials, determined mainly by their kinetic energy, is represented by the "universal curve" shown in the Figure 2.1.3. The kinetic energy range of 10 – 1000 eV corresponds to IMFP within 5-20 Å, ensuring the highest surface sensitivity. Another parameter to consider is the photoionization cross-section that is the probability of the electron excitation at the original electronic level. The photoionization cross-section, in turn, depends on the photon energy.

2.1.1. Synchrotron radiation photoelectron spectroscopy

The synchrotron radiation photoelectron spectroscopy (SRPES) technique is based on the use of a synchrotron facility as a source of tunable excitation light. The synchrotron radiation sources of third-generation consist of an electron gun, a linear accelerator, a booster, and a storage ring with magnetic components. The electrons, generated by an electron gun, are accelerated to several MeV and introduced to a booster where their energy is increased up to GeV. From the booster ring, high-energy electrons are inserted into a storage ring. Here, electrons move with relativistic speed in a circular orbit. Magnetic field, provided by bending magnets, undulators or wigglers, forces electrons to maintain their circular trajectory. At each deviation from the linear direction by Lorentz forces, the electrons generate radiation distributed mainly in the tangential direction and collected at the exit by the beamline optical system. The energy of photons produced by electrons circulating in a storage ring can vary from meV (infrared light) to tens of keV (hard X-rays). The radiation is highly intense with excellent brightness, coherency, variable polarization, and broad energy spectrum. The monochromator of a beamline is designed to allow for the experimental work at the end station with the use of a desired photon energy. The PES technique benefits enormously from the possibility of adjustment of the parameters such as surface sensitivity and photoionization cross-section. We can see in the Figure 2.1.3 that the electrons with kinetic energy of 50 – 100 eV provide the lowest IMFP and, thus, the highest surface sensitivity. The specific photoionization cross-section value might enhance or diminish the PES sensitivity toward discrete elements. Other advantages of SRPES are highly focused beam of the incident light and good resolving power. In general, the photon flux of the synchrotron radiation is much higher than the one provided by conventional laboratory X-ray sources. That contributes to the acquisition of well-resolved photoemission spectra.[74]

2.1.2. Resonant photoelectron spectroscopy

Resonant photoelectron spectroscopy (RPES) is a technique that employs resonant enhancement of the photoemission from a specific electronic level. The resonance effect is caused by irradiation of the matter with photons of energy near the photoabsorption threshold of the core level electrons. First, electrons absorb energy from incident photons; then, they move to the excited states, which quickly decay via autoionization, releasing enough energy for emission of photoelectrons from higher energy levels. On the other hand, direct photoemission could be present as well. Both mechanisms lead to the same final state. In certain circumstances, quantum mechanical interference of these processes can take place, resulting in a stronger or weaker probability of photoemission.[75] The RPES is an element selective technique[76] and is often used to enhance intensity of specific electronic states in the valence band spectrum, which are closely related to the surface composition of the matter. Values of the excitation energy, at which the RPES features have maximum intensity, are estimated from the constant initial state curves acquired at the corresponding photon energy range. Due to the necessity of a tunable light source, the synchrotron facility is required for RPES measurements.

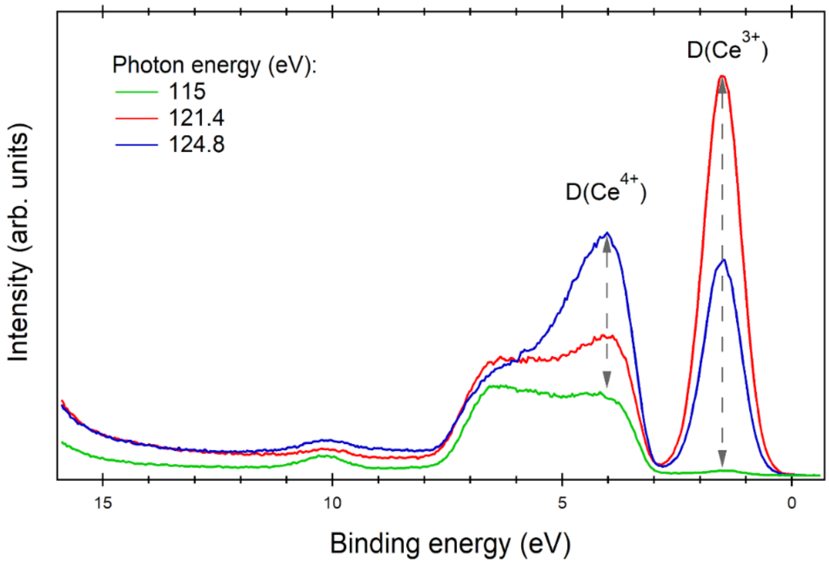

Fig. 2.1.4. *RPES valence band spectra of partially reduced cerium oxide film measured with photon energies: 115 eV (off-resonance), 121.4 eV (Ce^{3+} resonance), and 124.8 eV (Ce^{4+} resonance). The arrows show resonance enhancements D(Ce^{3+}) and D(Ce^{4+}).*

The RPES technique is frequently applied to estimate the relative amount of Ce^{3+} and Ce^{4+} ions in the surface layers of the cerium oxide films. The resonant enhancement from the Ce 4f state is possible when the photon energy is around or above an absorption threshold from the specific core level. In the case of cerium oxide, the Ce 4d→4f transition is used most often. The main features of cerium oxide in the valence band are spread between 1 and 8 eV (Fig. 2.1.4, green line). This spectrum corresponds to off-resonance transition for both cations and is measured with photon energy 115 eV. The electron configuration of cerium cations is $[Xe]4d^{10}4f^{0}$ in Ce^{4+} state and $[Xe]4d^{10}4f^{1}$ in Ce^{3+} state. In the case of the resonance enhancement, electrons excited to the unoccupied states during recombination with a hole in the 4d level can provide energy to another electron in 4f state, leading to its emission. The Ce^{3+} resonance occurs due to super Coster-Kronig decay, when photon energy of 121.4 eV is used, and appears at binding energy of 1.5 eV (Fig. 2.1.4, red line). The Ce^{4+} resonance occurs due to electron emission from Ce 4f - O 2p hybridized states at photon energy 124.8 eV. It is observed as a feature located at binding energy ~4 eV (Fig. 2.1.4, blue line).[77] The resonant enhancements of Ce^{3+} and Ce^{4+} ions can be determined from the spectra as a difference between intensity values of on- and off-resonance spectra at corresponding binding energies (shown in Fig. 2.1.4. as $D(Ce^{3+})$ and $D(Ce^{4+})$, respectively). The resonant enhancement ratio (RER), equal to $D(Ce^{3+})/D(Ce^{4+})$, provides information about reduction state of the surface cerium cations.

2.1.3. Data acquisition and analysis

For the model experiments in this work, the molecular adlayers were characterized by SRPES, RPES, and XPS, after deposition on the oxide films at 25 °C. The thermal stability of molecular films was then studied by annealing at 75, 100, 125, 150, 175, 200, and 250 °C for 1 min. The O 1s, N 1s, and C 1s core level spectra were acquired with photon energies of 630, 475, and 410 eV, respectively. The photoemission spectra were normalized to the incidence photon flux. After each annealing step, the measured spot on the sample was changed. Thus the radiation damage was considered negligible. The total intensity of N 1s or C 1s core levels was calculated as the integrated area under the spectrum after subtraction of the background and then divided by corresponding cross-section value. Cu $2p_{3/2}$, W $4f_{7/2}$, Ce 3d, O 1s, C 1s, and N 1s core levels were also measured by Al Kα X-ray source. Information about the reduction state of the top surface of the oxide film was obtained from the RER values calculated as shown in the Chapter 2.1.2.

Information on the degree of oxidation/reduction of the cerium oxide within the whole film was obtained from the Ce 3d core level spectra. Since the photoelectron spectrum contains information on both initial and final states of the emitted electron, the Ce 3d core level has quite a complex structure. For cerium oxide with cations only in 4+ state, Ce has $4f^0$ configuration in a ground state.[78–80] In the case of reduced oxide, the Ce^{3+} cation configuration is $4f^1$.[81–83] After photoexcitation of the core level electron, the Ce^{4+} state can reveal three final states: $4f^0$, $4f^1$, and $4f^2$, and the Ce^{3+} state may have two final states: $4f^1$ and $4f^2$.[79] As a result, the five final states can be expected in case of mixed cerium oxide with Ce^{3+} and Ce^{4+} cations. For each final state, the different shielding of a core hole results in a distinct spectral component at the specific binding energy.[81] Due to the spin-orbit splitting of *d*-level spectra, the peak components have a doublet structure. Thus, the Ce 3d peak obtained from the CeO_{2-x} ($0 < x < 0.5$) film consists of three $3d_{3/2}$-$3d_{5/2}$ spin-orbit split doublets corresponding to Ce^{4+} and two doublets coming from Ce^{3+} state. An example of the Ce 3d spectrum obtained from $CeO_{1.7}$/Cu(111) is shown in the Figure 2.1.5. The spectrum was fitted with five Voight doublets in the KolXPD software using the procedure described in details in Ref.[84] The blue doublet at the lowest binding energy assigned to the $4f^2$ final state configuration of Ce^{4+} cations is built by a combination of the two Voight doublets due to its asymmetrical nature.[84] The split between the components of a doublet was found to be 18.4 eV. Since the spectra were measured with a non-monochromatized X-ray source, normalized spectrum recorded from the clean Cu(111) substrate with satellites from Cu 2p level was subtracted.

The relative amount of the Ce^{3+} cations, $c(Ce^{3+})$, was derived from the fitted spectra as:

$$c(Ce^{3+}) = I(Ce^{3+})/I(Ce^{all}), \qquad \textbf{Eq. 3}$$

where $I(Ce^{3+})$ is the intensity of the components corresponding to the Ce^{3+} states, and $I(Ce^{all})$ is the total intensity of the Ce 3d spectrum after background subtraction.

The stoichiometry ratio of the CeO_{2-x} film was estimated in the following way:

$$x = 0.5 * I(Ce^{3+})/I(Ce^{all}) = 0.5 * c(Ce^{3+}), \qquad \textbf{Eq. 4}$$

where $0 \le x \le 0.5$.

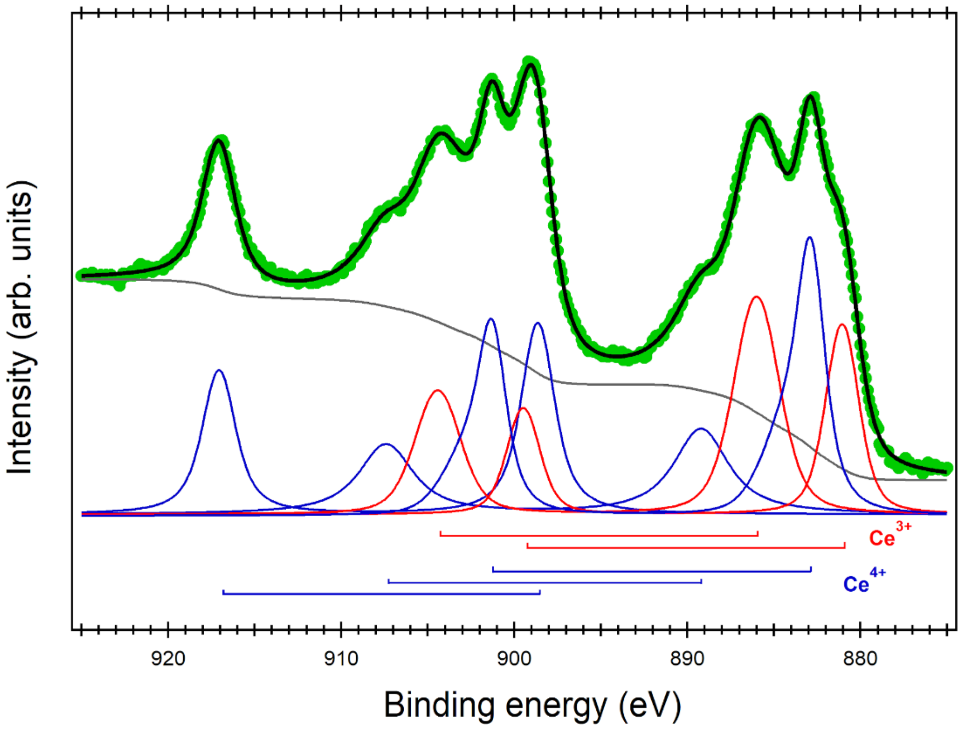

Fig. 2.1.5. *Ce 3d spectra of the* $CeO_{1.7}$ *thin film. Green circles correspond to the experimental data, the black line is the resulting fit, the grey line is a Shirley background, the three blue doublets correspond to the peaks of* Ce^{4+} *states, and the two red lines correspond to the* Ce^{3+} *states.*

The effective thickness d of the cerium oxide-based thin films was calculated using the following equation under assumption that the film is homogeneous and flat:

$$I_d = I_0\, e^{\frac{-d}{\lambda_m}}, \qquad \textbf{Eq. 5}$$

where I_0 and I_d are the intensity of the Cu $2p_{3/2}$ or W $4f_{7/2}$ peak from the substrate before and after deposition of the cerium oxide film, respectively. The inelastic mean free path (IMFP) λ_m of photoelectrons from the Cu $2p_{3/2}$ or W $4f_{7/2}$ orbitals passing through the cerium oxide film was estimated to be 11.2 or 22.8 Å, respectively, using TPP-2M formula.[85]

The effective thickness d of the glycine adlayers on the cerium oxide-based thin films was also estimated using the equation (**Eq. 5**), but in this case I_0 and I_d are the intensity of the Cu $2p_{3/2}$ or W $4f_{7/2}$ peak from the oxide before and after deposition of glycine, respectively. The IMFP λ_m of photoelectrons passing through the molecular adlayer was calculated using the equation for organic materials:[86]

$$\lambda_m = \frac{49}{E_k^2} + 0.11\,E_k^{1/2}\ \text{mg/m}^2, \qquad \textbf{Eq. 6}$$

where E_k is the kinetic energy of the Cu $2p_{3/2}$ or W $4f_{7/2}$ core level photoelectrons. To convert λ_m to distance units, it was divided by the density of glycine powder (1.607×10^9 mg/m^3). The IMFP of the photoelectrons from the Cu $2p_{3/2}$ and W $4f_{7/2}$ orbitals passing through the glycine adlayer was estimated to be 16.1 and 26.1 Å, respectively.

The effective thickness of glycine and sarcosine adlayers on the polycrystalline cerium oxide samples was estimated from the attenuation of the O 1s signal measured with photons of 1486.6 eV using **Eq. 5**. The IMFP was calculated to be 21.2 Å and 31.1 Å for glycine and sarcosine, respectively, using the **Eq. 6**.

As the effective thickness of the molecular film has only qualitative character, we further estimated the molecular coverage in monolayers (MLs) under assumption of the adlayer growth in the form of islands. In this case, the coverage of the cerium oxide surface by glycine molecules was estimated by analyzing the ratio of the N 1s intensity to the topmost surface contribution of the Ce 3d signal from the clean oxide film. Both spectra were acquired with a photon energy of 1486.6 eV. The idea was to relate the number of nitrogen atoms to the number of cerium cations on the surface. The coverage was evaluated for each model system after molecular adlayer deposition and after annealing at 75 °C, with an aim to minimize the contribution from the weakly bound or physisorbed species. The topmost surface $(Ce\ 3d_{clean})_{surf}$ signal, which accounts for the photoelectrons from the first O–Ce–O trilayer of thickness 3 Å, was derived from the Ce 3d peak area, taking into account the IMFP value of Ce 3d photoelectrons in cerium oxide (11.7 Å) and layered structure of the film.[87]

The integrated intensity of the N 1s spectrum acquired from the adsorbed molecules is considered to be proportional to the glycine coverage θ (see Fig. 2.1.6). The surface component $I(Ce\ 3d_{clean})_{surf}$ accounts for the photoelectrons escaping from uncovered oxide $(1-\theta)$ and from the surface underneath the molecular adlayer $\theta \times \exp(-4/\lambda)$ (Fig. 2.1.6). The intensity ratio can be represented by the following equation:

$$\frac{I(N\ 1s)}{I(Ce\ 3d_{clean})_{surf}} = \frac{\theta}{((1-\theta) + \theta \times \exp(-4/\lambda))}, \qquad \textbf{Eq. 7}$$

where 4 Å is the size of the glycine molecule according to Ref.[88] and λ is the IMFP of Ce 3d photoelectrons in glycine calculated from the equation **Eq. 6** and equals to 16.6 Å.

For instance, for the glycine/CeO_2 system annealed at 75 °C, the coverage of 0.23 ML was found. Since glycine contains only one nitrogen atom, 0.23 ML means 1 molecule per 4 or 5 cerium cations on the surface. Size of the glycine molecule reported in the literature varies between 3.5×3.9 Å[89] and a sphere with a diameter 4 Å.[88] According to Ref.[90] size of the surface unit cell of cerium oxide is 3.82 Å. Therefore, it is obvious to expect that one glycine molecule may cover from 2 to 4 unit cells of cerium oxide in the case of flat adsorption geometry which is in agreement with the estimated coverage value.

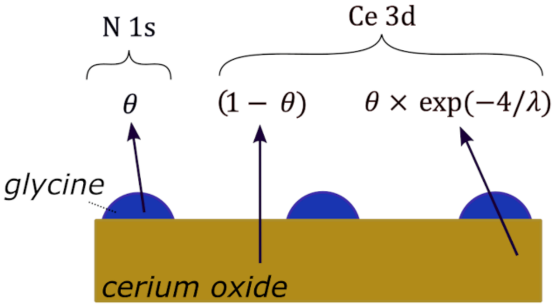

Fig. 2.1.6. *Schematic diagram of the coverage estimation for the glycine adlayer on the cerium oxide film.*

Taking into account similarity in behavior of the N 1s and C 1s core level spectra of glycine adlayers on CeO_2 and Ce_6WO_{12} and based on the coverage value for CeO_2, we estimated molecular coverage on the Ce_6WO_{12} surface by comparison of the integrated N 1s intensities for the two systems.

2.2. Near edge X-ray absorption fine structure spectroscopy

The near edge X-ray absorption fine structure (NEXAFS) spectroscopy is a relatively young technique that was introduced in the 1980s. NEXAFS is an efficient tool for investigation of the electronic structure and spatial orientation of adsorbed molecules. The NEXAFS is the most commonly used for organic molecules consisting of atoms with low atomic number, $\boldsymbol{Z}$, such as C, N, O, F. The NEXAFS spectra represent dependence of the photoabsorption cross-section on the incoming photon energy and reveals strong characteristic features just below and up to a few tens electronvolts above the absorption edge.

The main principle of the NEXAFS spectroscopy is absorption of electromagnetic radiation by matter through excitation of the core level electrons (usually K-shell) to unoccupied bound or continuum states. It leads to creation of a core hole with a short lifetime.

The hole is then filled by an electron either through Auger process or radiatively by emission of a fluorescent photon. For detection of core hole annihilation both, fluorescence photons and Auger electrons, as well as electrons inelastically scattered in the material (secondary electron yield), can be used. For atoms with low ***Z*** number, the Auger electron yield is considerably higher than the fluorescence yield.[91] Detection of the Auger electrons provides element-specific information and also leads to the highest surface sensitivity due to relatively low kinetic energy of the electrons and their IMFP in the material. The fluorescence yield detection mode is actively used for studying samples in liquid or gaseous form.

A schematic illustration of the nature of characteristic features in the NEXAFS spectrum is shown in the Figure 2.2.1. A step-like increase of the signal intensity occurs as the photon energy passes an ionization threshold. Excitation of a core electron to a bound state takes place as a transition from 1s atomic level to unoccupied (usually antibonding) molecular orbitals of π or σ symmetry, or as a transition into Rydberg states. Transitions to empty bound states can happen only in case when the energy of the incident photons equals exactly to energy difference between the initial electron orbital and the unoccupied one (usually marked as π* or σ*). Transition from 1s to π* orbital, also called π*-resonance transition, is possible only in systems with π-bonding, e.g., in systems with double or triple bonds between atoms, but never for single bound systems. The π*-states usually occur below the ionization edge due to electron-hole Coulomb interaction[92] and are the lowest unoccupied molecular orbitals for diatomic structure with π-bond. Rydberg states are located between the π*-states and the ionization potential. The σ*-states take place at higher energies and give wide resonances due to overlapping with continuum states. The π* and Rydberg orbitals provide sharp narrow resonances caused by short lifetime of the excited electron. However, the latter are weak, especially in the case of chemisorbed molecules or in a condensed phase. If the hydrogen bonds are present, Rydberg orbitals are mixed with hydrogen-originated antibonding orbitals of the same symmetry that results in higher intensity of the corresponding resonant transitions. Molecules that contain C–H bonds produce highly intense features in C K-edge that are usually referred to a mixture of Rydberg and valence resonances.[93,94] Some systems reveal sensitivity of the σ*-resonances position on the energy scale to the length of the corresponding bond. It makes possible estimation of the bond lengths by the NEXAFS spectra analysis.[92]

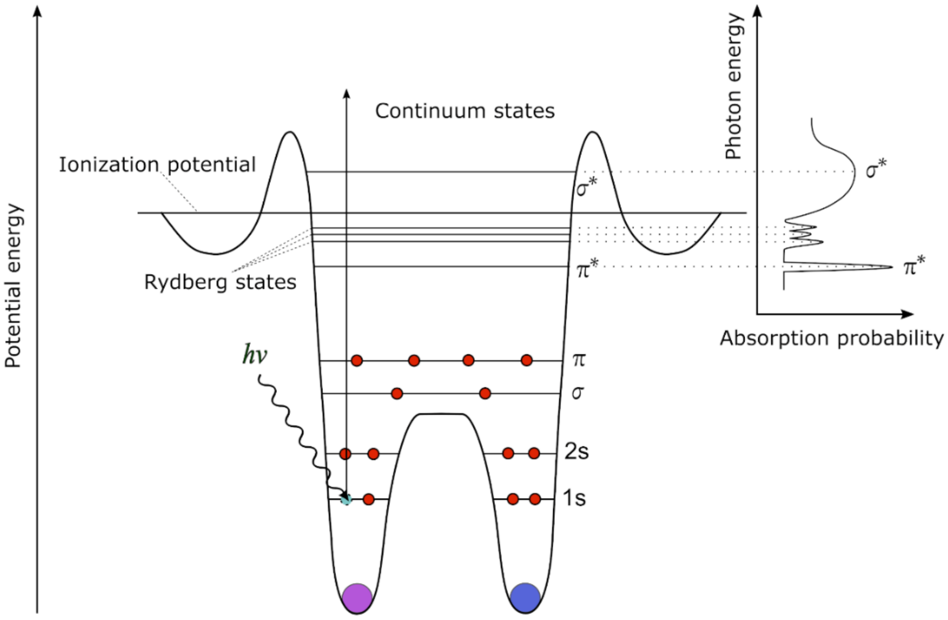

Figure 2.2.1. *Schematic illustration of potential (left) of diatomic molecule and corresponding NEXAFS K-edge spectrum (right).*

Additionally to the information about chemical state of the molecules or the molecular fragments, NEXAFS can provide information about their orientation on the surface. Intensities of the resulting π* and σ* resonances depend on the angular orientation of electric field vector of the incident light with respect to corresponding molecular bonds. Since intensity of transition, $\boldsymbol{I}$, due to Fermi's golden rule is proportional to the angle, $\boldsymbol{\delta}$, between direction of the final state molecular orbital and the electric field vector ($\boldsymbol{I} \propto \boldsymbol{cos^2 \delta}$),[95] thus, the highest intensity of a resonance transition can be achieved when direction of the final state orbital and electric field vector are parallel. When they are at a normal to each other, the transitional intensity vanishes. It is important to consider that σ* orbitals have a maximum amplitude in the direction along the bond and π* orbitals in direction perpendicular to the bond.

In this work, the NEXAFS spectra of the glycine and sarcosine adlayers on the oxide films were acquired at C and N K-edges in partial KVV Auger electron yield mode with a total energy resolution estimated to be 0.23 and 0.38 eV, respectively. The spectra were measured in two geometries: grazing incidence GI (10°, molecular orbitals perpendicular to the surface are mostly excited) and normal incidence NI (90°, molecular orbitals parallel to the surface are excited). The NEXAFS spectra were normalized to the incident photon flux. The corresponding spectra measured on the clean oxide surfaces were subtracted as a background.

2.3. Materials Science beamline at Elettra-Sincrotrone Trieste

Elettra is a third-generation synchrotron facility located in Trieste (Italy) that provides light since 1994 and runs in the top-up mode since 2010. The relativistic electrons in the storage ring circulate in two configurations: at energy 2.0 (75% of the time) and 2.4 (25% of the time) GeV with the current set to 310 and 140 mA, respectively. The injector consists of the linear accelerator and full energy booster and provides injection every 6 (for 2.0 GeV) and 20 (for 2.4 GeV) minutes, keeping the electric current in the ring constant to 3 and 7 %, respectively. 28 beamlines are currently operating at the Elettra synchrotron. They allow users from all over the world access to techniques based on photoelectron emission, absorption, scattering, diffraction, reflection/emission, imaging, and lithography with application of tunable, bright, and monochromatic synchrotron radiation.

All PES and NEXAFS experiments presented in the current work were performed at the Materials Science beamline (MSB) at Elettra-Sincrotrone Trieste. The synchrotron light of the beamline is provided by a bending magnet and a plane grating monochromator and is believed to be between 80 – 90% linearly polarized in the horizontal direction with photon energy from 22 to 1000 eV. The beamline was designed for surface science research on a wide range of materials and is well equipped for the photoelectron and absorption spectroscopy studies in UHV. The spot size of the beam on the sample surface is about 200 μm in vertical and 500 μm in horizontal direction.

The end station of the beamline consists of three UHV chambers (experimental, preparation, and load lock chambers) equipped with a Specs Phoibos 150 hemispherical electron energy analyzer, an X-ray source with Mg/Al dual anode, an e-beam evaporator, a gas inlet system, an ion gun, low energy electron diffraction (LEED) optics, a sample manipulator with a heating system and a K-type thermocouple attached to the rare side of the sample. A small load lock chamber is used for the fast entry of the sample. There is a possibility to mount additional equipment in case if needed. In our experiments, the Knudsen cell type evaporators were mounted in the preparation chamber for deposition of the molecules under UHV. During deposition of the molecules from solution, a glove bag filled with nitrogen was connected to the load lock chamber to minimize interaction of the studied system with ambient environment. A base pressure was 3×10^{-10} and 2×10^{-9} mbar in the experimental and preparation chambers, respectively.

MSB provides photon beam of moderate intensity in the soft X-ray range, a unique combination that is highly appropriate to the study of the bio or organic molecules adsorbed on surfaces. Tunability of the photon beam up to 1000 eV allows to choose optimal conditions for the acquisition of the well-resolved spectra using the photon flux, which is not particularly destructive for the systems under investigation. This setup is well suited for the study of the surface valence band features with enormous potential for the RPES technique, especially when applied for the characterization of the cerium oxide thin films. The measurements in this work were performed on samples in normal and grazing incidence and normal emission geometries. The total resolution of photoemission spectra, defined by the beamline settings and pass energy of the hemispherical analyzer, was determined by measuring the Fermi edge broadening at 25 °C, which gave the following values 0.69, 0.49, 0.38, and 0.17 eV for photon energy 630, 475, 410 and 115 eV, respectively. The Ce 3d core level spectra were always measured with the Al Kα X-ray source at the 20° emission (the angle between the analyzer and the sample normal) with the total resolution of about 1 eV.

2.4. Electrochemistry

The second part of the work is devoted to biosensing properties of the CeO_2 films studied with the use of the electrochemical techniques. The compact polycrystalline cerium oxide thin film was proposed as a working electrode for the biosensing systems. This chapter contains a short description of used electrochemical techniques: cyclic voltammetry (CV), chronoamperometry (CA), and electrochemiluminescence (ECL).

Part of the electrochemistry known as voltammetry was developed after discovering polarography by the Czech chemist J. Heyrovsky in 1922 that brought him the Nobel Prize in chemistry in 1959. In voltammetry, current is measured as a function of applied potential and provides information about the analyte. To apply the potential accurately and measure the current precisely, a three-electrode setup of the electrochemical cell is commonly used. The three important components engaged are working, counter, and reference electrodes. They are connected to a potentiostat on one side and immersed into a working solution on the other side. The potentiostat applies a potential to the working electrode, set correctly with assistance of the reference electrode, and, at the same time, detects current that flows between counter and working electrodes.

Cyclic voltammetry (CV) (firstly reported in 1938) is one of the potential sweep electrochemical methods. It is a very common and powerful technique for obtaining qualitative information about electrochemical processes. In particular, it allows the rapid detection of the redox potentials, provides information on kinetics of electron-transfer reactions and adsorption processes, and sheds light on thermodynamics of redox processes. In CV, the potential applied to the working electrode linearly changes from the initial $\boldsymbol{E_i}$ to the final $\boldsymbol{E_f}$ value, which is called a linear potential sweep, and then returns back to the $\boldsymbol{E_i}$ (Fig. 2.4.1 a). This process is cycled with a known sweep (or scan) rate. The final voltammogram is a plot of the measured current versus the applied potential with the characteristic peaks corresponding to redox processes. The typical shape of cyclic voltammogram of quasi-reversible processes is shown in the Figure 2.4.1 b. As the potential goes in the positive or anodic direction, oxidation of the analyte occurs. The sweep in the negative or cathodic direction of the applied potential leads to reduction of the analyte. Reversibility of the electrochemical process can be estimated from the difference between the anodic and cathodic peaks potentials that is called peak-to-peak separation ΔE_p, that is caused by the diffusion of the analyte from and to the electrode during the reaction in a working solution. In ideal conditions ΔE_p of the reversible process at 25 °C is equal to 57 mV. In quasi-reversible processes the ΔE_p is not constant and changes at different scan rates.[96,97]

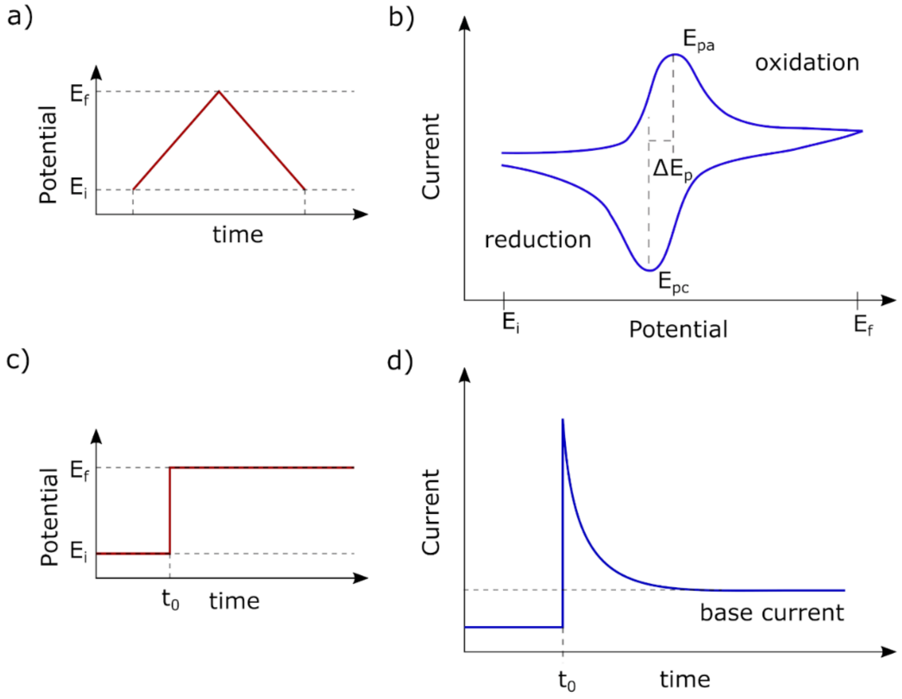

Figure 2.4.1. *Schematic diagrams of applied potential in a) CV and c) CA measurements; b) typical cyclic voltammogram of quasi reversible electrochemical process; d) scheme representing dropping of the current in CA experiment when the applied potential is kept constant.*

In the case of analyte species adsorbed on the electrode surface, no peak-to-peak separation is observed. Low-barrier electron transfer between the analyte and electrode results in a reversible electrochemical reaction. High-barrier electron transfer causes irreversibility of the electrochemical process since, in this case, higher potentials are needed to achieve oxidation or reduction. Usually, the recorded current is normalized to the surface area of the electrode and defined as a current density. The amplitude of the signal is proportional to the amount of analyte in a working solution, which permits an estimation of its concentration. The intensity also depends on the scan rate and can give insight into the role of adsorbates, diffusion processes, etc.[98]

Chronoamperometry (CA) is an electrochemical technique for which a similar setup is employed as for CV. In CA, a step potential is applied to the working electrode and resultant current is acquired as a function of time. Usually, prior to the CA measurements, a few scans of CV are recorded to identify the potentials at which reduction and oxidation peaks appear. Then the potential value at which a redox reaction occurs is chosen and used for CA. In conditions of constant potential, the measured current reflects variation in the analyte concentration near the electrode surface. There are two common ways of performing the CA experiments: by applying a single (current is acquired at potential on, shown in Fig. 2.4.1 c) or double (acquisition at potential off – it returns to the initial value after a certain amount of time) potential step. When the mass transport is controlled only by diffusion process, the diffusion layer of the reactive species near the electrode expands as reaction occurs. It leads to a decrease of the signal between the working and counter electrodes and reaching of the base current when the analyte is consumed (Fig. 2.4.1 d). Integration of the area under the recorded current curve and application of Faraday's law allows to estimate the total charge of the reaction. If solution in the cell is continuously stirred, intensity of the current will correspond to the concentration of the analyte in bulk. Thus, CA allows to estimate concentration of the reactive species in the solution and very often is used in biological sensors. Biosensors based on amperometric measurements can provide a good selectivity since every analyte has distinct potentials for reduction and oxidation reactions.[99]

Electrochemiluminescence (ECL), also known as electrogenerated chemiluminescence, is based on the generation of light by the analyte species at the electrode surface after applying of a potential. The essential component of the setup is chromophore species which help to enhance electrostimulated chemical reaction in the working solution. There are three different categories of chromophore mediator systems used in ECL: inorganic complexes (based on transition metals), organic systems (include polycyclic aromatic hydrocarbons), and nanostructured materials. When the potential is applied to the electrode, excited intermediate species are generated in course of the electrochemical reaction via the electron transfer. The photon emission occurs as a result of relaxation to the lower energy state. The most used chromophore in the ECL measurements is ruthenium(II)tris(2.2′-bipyridine) complex $(Ru(bpy)_3)^{2+}$, the first inorganic complex employed for the ECL signal enhancement.[100]

There are two general strategies for photon generation in ECL: annihilation and co-reactant. In the annihilation system, a double-potential step should be applied to activate highly energetic precursors that generate an excited molecule after the reaction. Both oxidized and reduced species are involved in the chemical reaction at the electrode. The co-reactant mechanism requires only one-potential step. During the potential sweep in one direction that causes the oxidation or reduction of co-reactant, an intermediate state, which further develops through the interaction with luminophore and formation of an excited state, is reached.[100] The narrow potential window, within which the working solution is stable, is a big advantage of this system. Thus, it allows to perform the ECL measurements in aqueous solutions, which is particularly suitable for medical tests.

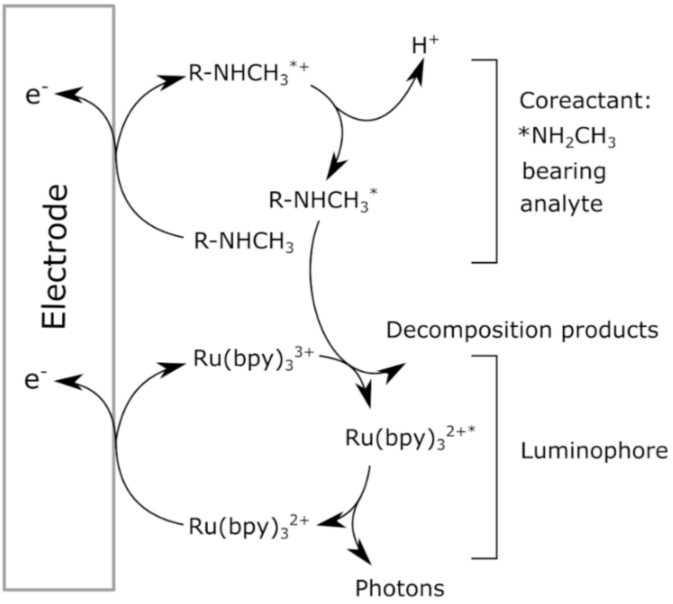

Fig. 2.4.2. *Schematic illustration of the excited* $(Ru(bpy)_3)^{2+}*$ *species generation by the co-reactant oxidation-reduction mechanism using amines.*

In the co-reactant ECL systems, the polypiridine Ru complexes (particularly $(Ru(bpy)_3)^{2+}$) combined with amines (the most commonly tropropylamine (TPrA))[48] are generally used. In this setup, the $Ru(bpy)_3)^{2+}$ luminophore can be oxidized at the electrode to $(Ru(bpy)_3)^{3+}$. The direct oxidation of the amine co-reactants is accompanied by deprotonation and formation of stable radical species, which eventually reduce the Ru complex to $(Ru(bpy)_3)^{+}$. After interaction of $(Ru(bpy)_3)^{3+}$ and $(Ru(bpy)_3)^{+}$ the excited molecule $(Ru(bpy)_3)^{2+}*$ is generated with subsequent relaxation and spontaneous light emission of 620 nm wavelength. A schematic illustration of the excited $(Ru(bpy)_3)^{2+}*$ species generation in the co-reactant ECL systems is shown in the Figure 2.4.2.

2.5. Characterization of the surface ordering and oxide film morphology

2.5.1. Low energy electron diffraction

Low energy electron diffraction (LEED) is a UHV technique used to characterize surface long-range crystal structure and symmetry of samples. The back-view LEED setup consists of an electron gun, a set of grids, a fluorescent screen, and a video camera. The electron gun provides a highly collimated beam of electrons with kinetic energy of 20-200 eV. The wavelength of the electrons is comparable with an interatomic distance in solid materials and does not exceed 3 Å. It allows the electrons to undergo diffraction on the crystalline surface after interaction with the matter. Since the inelastic mean free path for low energy electrons (20-200 eV) is about 1 nm, this technique is highly surface sensitive. The electrons inelastically back-scattered by the surface are selected and accelerated, depending on their energies, by the grids system and, after reaching the fluorescence screen, create a diffraction pattern recorded by a video camera. Thus, the LEED pattern with sharp diffraction spots is observed from the surface with atoms in a well-ordered periodical structure. Moreover, the LEED image displaying the reciprocal lattice of the surface brings information about surface reconstructions and relaxations with a possibility to estimate the lattice parameter, etc.[101]

In this work, the LEED technique was used for the qualitative analysis of the surface ordering of the cerium oxide-based thin films. The typical LEED patterns obtained from the $CeO_2(111)/Cu(111)$, $CeO_{1.7}(111)/Cu(111)$, $Ce_6WO_{12}(100)/W(110)$ and $Ce_2O_3(111)/Cu(111)$ thin films are shown in the Figure 2.5.1.

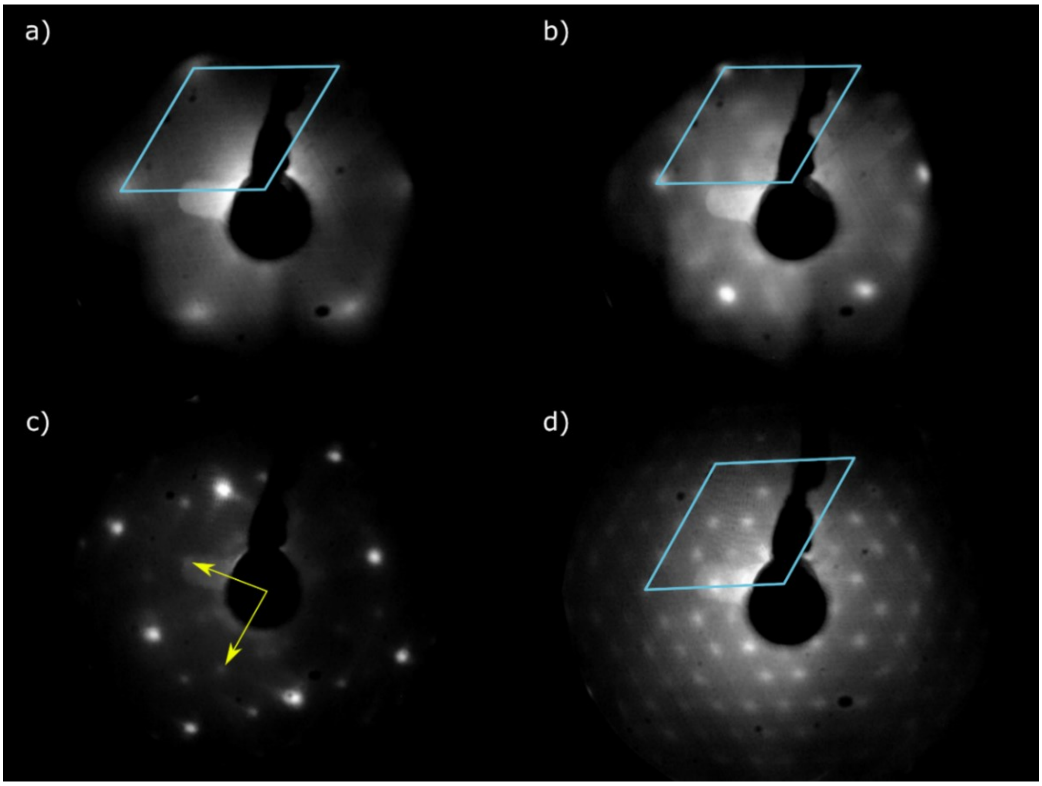

Fig. 2.5.1. *LEED images of cerium oxide-based thin films prepared on Cu(111) and W(110) single crystals: a) (1 × 1) CeO_2(111)/Cu(111), b) (3 × 3) $CeO_{1.7}$(111)/Cu(111), c) Ce_6WO_{12}(100)/W(110) and d) (4 × 4) Ce_2O_3(111)/Cu(111) taken with electron energy of 94, 102, 70, and 96 eV, respectively. The blue tetragon in a), b) and d) corresponds to the (1×1) CeO_2(111) unit cell; yellow arrows in c) represent unit vectors of Ce_6WO_{12}.*

2.5.2. Atomic force microscopy

Atomic force microscopy (AFM) is a high-resolution ambient pressure surface science technique used to characterize the sample topography, morphology, and roughness. Besides that, AFM allows to define the surface potential and mechanical properties of the materials. It can also be applied for controlled manipulations of the processes on the surface. An AFM image is obtained by scanning over the sample's surface with a probe that consists of a sharp tip (nm radius) connected to cantilever (µm size), which is placed on the holder (mm size). As the probe moves over the surface, it is deflected by atomic forces in consequence of the interaction between the tip and the sample. This deflection is monitored by a photodiode that registers reflection of the laser beam from the cantilever. The feedback loop receives a signal from the photodiode and adjusts the distance between the tip and the sample surface. Information from the photodiode is also used to build an image of the surface. There are several modes of AFM measurements: contact, tapping, and non-contact.[102]

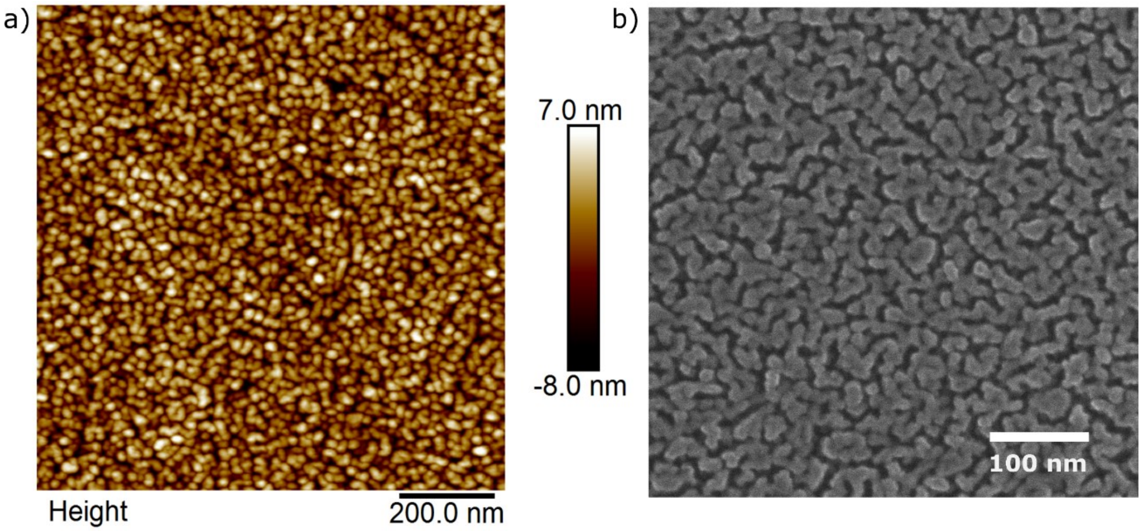

Fig. 2.5.2. *a) AFM and b) SEM images of polycrystalline* CeO_2 *film deposited on the glassy carbon electrode.*

In this work, morphology and roughness of the polycrystalline CeO_2 samples prepared *ex situ* on Si wafer or glassy carbon substrate were examined by means of Bruker MultiMode 8 AFM microscope in a tapping mode. The typical AFM image taken from the polycrystalline CeO_2 film prepared by magnetron sputtering is shown in the Figure 2.5.2 a.

2.5.3. Scanning electron microscopy

Scanning electron microscopy (SEM) is a high vacuum technique used to characterize the surface morphology and composition of the solid-state samples. The surface is bombarded with a focused electron beam, which moves on the sample in a raster scan pattern. The electrons interact with atoms in the material by elastic and inelastic scattering, emitting secondary electrons, inducing radiation, etc. These products carry information about the scanned area of the sample surface. The integrated information on the electron beam position combined with the intensity of the detected signal is analyzed by a software and used to build a SEM image. There are several modes of the measurement: using secondary electrons (allows to investigate morphology since intensity of the secondary electrons emission depends on the angle between the surface and incidence electron beam), using backscattered electrons (provides information about composition based on the intensity of electron scattering from lighter and heavier elements), and using X-ray radiation (allows to determine atomic composition of the material, the technique is called energy-dispersive X-ray spectroscopy).[103]

In the current work, morphology of the polycrystalline cerium oxide thin films prepared *ex situ* was studied by using the Tescan Mira 3 SEM microscope using the secondary electron mode and 30 kV accelerating voltage, working distance was 2-3 mm. Since kinetic energy of secondary electrons was about 50 eV, the information depth of measurements in this mode was about several nanometers. The typical SEM image taken from polycrystalline CeO_2 film prepared by magnetron sputtering is shown in the Figure 2.5.2 b.

2.6. Model systems preparation

In this chapter, preparation and characterization of the samples used in the thesis are described. All substrates were divided into two groups based on the preparation method: samples prepared *in situ* by e-beam physical vapor deposition and samples prepared *ex situ* by non-reactive RF magnetron sputtering. The *in situ* oxide films were deposited on Cu(111) and on preoxidized W(110) single crystals. The *ex situ* substrates were grown on Si(111) wafer covered with natural oxide and on a glassy carbon substrate. Information on the molecular adlayers preparation and H_2O_2 and sarcosine detection is also provided.

2.6.1. Cerium oxide films prepared *in situ* and *ex situ*

In total, four types of samples were prepared *in situ*: $CeO_2(111)/Cu(111)$, $CeO_{1.7}(111)/Cu(111)$, $Ce_2O_3(111)/Cu(111)$, and $Ce_6WO_{12}(100)/WO/W(110)$.

As a substrate for the CeO_2 epitaxial thin films, the Cu(111) single-crystal (99.999% purity, MaTecK, 8 mm diameter, 2 mm thickness) was used. Before deposition of cerium oxide, the crystal was cleaned by cycles of Ar^+ ion sputtering and annealing at 450 °C. The surface was considered clean when no C 1s and O 1s signal was observed by photoelectron spectroscopy. Deposition of the CeO_2 film was performed under oxygen atmosphere (5×10^{-7} mbar) by e-beam physical vapor deposition of cerium (99.99% purity, Goodfellow) on the Cu(111) crystal kept at 250 °C with following annealing at the same temperature under the same oxygen pressure for 10 min. The surface ordering was checked by LEED and revealed (1×1) $CeO_2(111)/Cu(111)$ pattern (Fig. 2.5.1 a). Thickness of the oxide film was estimated from the attenuation of the Cu $2p_{3/2}$ core level signal (for details, refer to the Chapter 2.1.3) and was about 21 Å.[104]

Partially reduced cerium oxide film $CeO_{1.7}(111)/Cu(111)$ was prepared by deposition of metallic Ce in UHV onto $CeO_2(111)/Cu(111)$ buffer and followed by annealing at 600 °C for 30 min.[105] Thermally stimulated mobility of oxygen atoms in the oxide film leads to the formation of an ordered partially reduced cerium oxide film with gradually decreasing concentration of vacancies from the surface to the bulk.[105] The total thickness of 38.5 Å was calculated from the attenuation of the Cu $2p_{3/2}$ peak intensity. The stoichiometry ratio of 1.7 was estimated from the fitting of the Ce 3d core level (more details in the Chapter 2.1.3). LEED measurements revealed (3 × 3) $CeO_{1.7}$(111)/Cu(111) pattern (Fig. 2.5.1 b).

The fully reduced epitaxial Ce_2O_3(111)/Cu(111) film was prepared in the same way as $CeO_{1.7}$ film by depositing cerium onto the CeO_2 buffer in situ, varying the amount of metallic Ce.[105] The oxide film contains exclusively Ce^{3+} cations and maximal density of oxygen vacancies through the whole thickness.[106] Estimated oxide thickness of the epitaxial stoichiometric (4 × 4) Ce_2O_3(111)/Cu(111) film (LEED pattern is shown in Fig. 2.5.1 d) was about 36.4 Å.

The epitaxial Ce_6WO_{12}(100) oxide was prepared on W(110) single crystal (99.999% purity, MaTecK, 10 mm diameter, 1.5 mm thickness), which was previously cleaned by cycles of Ar^+ sputtering and annealing at 900 °C in UHV and preoxidized to WO/W(110) by annealing at 600 °C in 5×10^{-7} mbar of oxygen. Cerium was evaporated on top at 500 °C under oxygen atmosphere (5×10^{-7} mbar) and then flashed to 900 °C.[106] The thermal treatment stimulates the diffusion of W atoms from the buffer oxide towards growing cerium oxide adlayer. In the cerium-tungsten mixed oxide Ce_6WO_{12}(100) tungsten is present in W^{6+} state and acts as high-valence dopants donating electrons to Ce^{4+} cations and causing their reduction to Ce^{3+}.[106] Thickness of the obtained film was calculated from the attenuation of the W $4f_{7/2}$ photoelectron peak intensity and was estimated to be about 6.5 Å. Photoemission and LEED (Fig. 2.5.1 c) measurements confirmed the formation of the Ce_6WO_{12}(100)/WO/W(110) oxide film with Ce atoms in Ce^{3+} state.

The polycrystalline cerium oxide films were prepared by nonreactive magnetron sputtering of a CeO_2 target (99.999%, Kurt J. Lesker). As the substrates, the single-crystalline Si(100) wafer with 4 nm thick natural oxide film and glassy carbon (>99.9%, Alfa Aesar, 1 mm thick, type 2) were used. The sputtering was done under Ar atmosphere (4×10^{-3} mbar). A growth rate of cerium oxide film of 1 nm min^{-1} was achieved by using a RF power of 80 and 65 W for Si(100) wafer and glassy carbon, respectively. The oxide film thickness was in the range 15 - 20 nm. The surface morphology and structure of the obtained ceria films was examined by Bruker MultiMode 8 AFM and Tescan Mira 3 SEM microscopes (Fig. 2.5.2). The estimated surface roughness was about 1.3 nm. The *ex situ* polycrystalline CeO_2 films were inserted in UHV and cleaned (soft Ar^+ sputtering and annealing in oxygen atmosphere at 250 °C) before deposition of the molecular adlayers.

2.6.2. Deposition of molecules *in situ* and *ex situ*

Glycine (NH_2-CH_2-COOH, 99.5 % purity, Alfa Aesar) and sarcosine (CH_3-NH-CH_2-COOH, ≥98 % purity, Sigma Aldrich) were used as received without further purification. UHV deposition of glycine/sarcosine was done in the preparation chamber by using a Knudsen-cell type evaporator. The glycine/sarcosine powder in the crucible was degassed at 85 °C, firstly, and heated to 95 °C/90 °C for deposition. Pressure in the chamber during deposition was about 4×10^{-8} mbar. The sample was held by a transfer rod at 25 °C during molecular deposition.

The molecular deposition from solution was carried out under nitrogen atmosphere in a glove bag connected to a fast entry chamber to avoid exposing the sample to ambient air. The 5 mM glycine and sarcosine solutions were prepared by addition of 18.77 mg and 22.27 mg of glycine and sarcosine powders, respectively, into 50 mL of MilliQ water (18.2 MΩ cm) with following stirring for 1 hour. One drop of the solution was placed on the studied substrate for 2 min and dried by N_2 flow. Then the sample was inserted into UHV chamber for measurements. 1 drop of pure MilliQ water was deposited on a clean surface in the same way for a reference. The multilayer coverage of glycine was prepared by depositing 1 drop of the glycine saturation solution (5 g glycine powder was added to 20 mL of MilliQ H_2O giving 3.3 M concentration, then stirring for 1 hour) on polycrystalline CeO_2 film, leaving for 2 min and drying with N_2 jet.

2.6.3. Cerium oxide electrodes for H_2O_2 and sarcosine detection

The polycrystalline CeO_2 films deposited on glassy carbon (GC) plate were used as an electrode for electrochemical biosensing. For this purpose, a custom cell with 10 mL volume was developed and constructed, in which the removable working electrode can be easily inserted for the electrochemical study (see Fig. 2.6.1 for details). Then the nanostructured CeO_2 working electrode was tested for H_2O_2 and sarcosine detection.

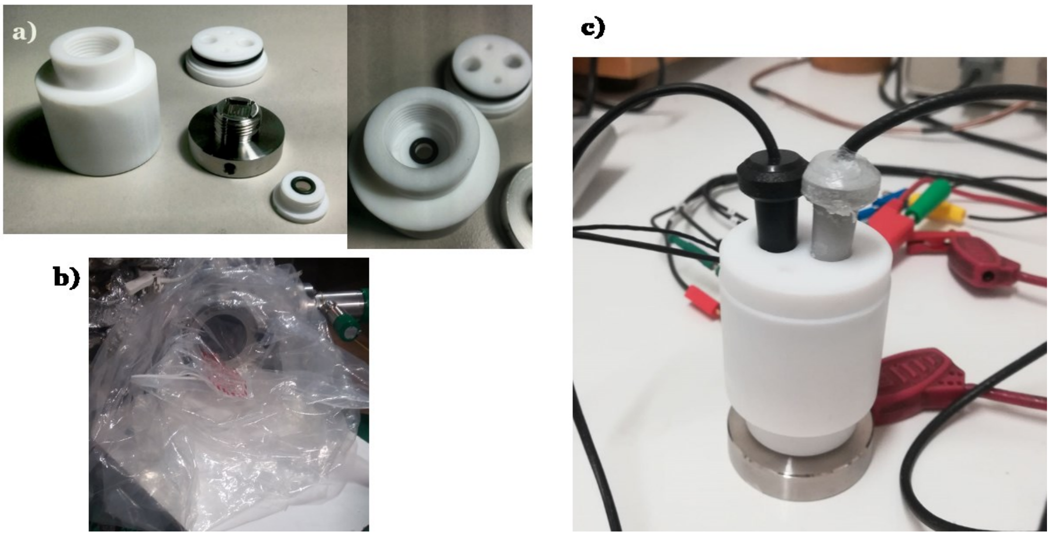

Fig. 2.6.1. *a) The dismounted electrochemical cell b) the load lock chamber with mounted* N_2 *filled glove bag for sample transfer in UHV, c) the cell during the electrochemical measurements.*

H_2O_2 detection

Electrochemical characterization of the CeO_2/GC electrode was performed at room temperature using a conventional cell with three electrodes. All potentials were measured versus the Ag/AgCl (3 M KCl) reference electrode purchased from BVT Technologies, and a Pt wire was used as a counter electrode. During the measurements, the working electrode was delimited by an o-ring (0.6 cm diameter), exposing to the solution an area equal to 0.28 cm^2. The measured current values were expressed as current densities considering the active surface area of the CeO_2/GC electrode. The working solution was phosphate buffered saline (PBS, heavy metals ≤ 5 ppm, BioPerformance Certified) with pH 7 and concentrations 200 mM and 10 mM. The ultrapure water (18.2 MΩ.cm from a Millipore MilliQ system, total organic content ≤ 5 ppb) was used to prepare the PBS solutions. Before each experiment, the solution was bubbled with nitrogen gas to obtain an oxygen-free environment. Experiments were carried out under nitrogen flow.

CV experiments were performed in the potential range swept between -0.35 V and 0.8 V at a scan rate of 50 mV/s. Furthermore, a set of CV curves was acquired at different pH (from 6 to 8) and at scan rates from 50 to 250 mV/s. The reference CV signals were obtained with the bare GC plate as a working electrode. In measurements with a mediator, 2 mM concentration of potassium ferricyanide ($K_3Fe(CN)_6$, 99 % purity, Sigma Aldrich) was added to the PBS working solution. Calibration curves were plotted as faradic current versus concentration of hydrogen peroxide.

Prior to CA measurements, two cycles of CV were performed in pure PBS solution to clean the electrode surface and check the functionality of the working electrode. CA experiments were conducted with constant stirring of the solution at potential 0.65 V against the Ag/AgCl electrode. Once a stable current was achieved for the CeO_2/GC electrode in PBS solution, the amperometric response was detected as a function of stepwise additions of H_2O_2 (30 %, Sigma Aldrich).

The CeO_2/GC electrode was characterized by XPS and RPES after 5 min immersion in the working solution and after performing CA measurements (about 30 min) in PBS with addition of low (0.05 mM) and high (8 mM) concentrations of H_2O_2. The samples were transferred to UHV under a nitrogen atmosphere (to minimize contamination from the ambient) after the indicated steps in CA.

Sarcosine detection

For the ECL sarcosine detection by the CeO_2/GC electrode, the sarcosine powder (≥98 % purity, Sigma Aldrich) and the tris(bipyridine)ruthenium(II) chloride mediator ($Ru(bpy)_3Cl_2 \cdot 6H_2O$, Sigma Aldrich) were used without further purification. Phosphate buffer solution (pH 7) with the concentration of 0.2 M was prepared by dissolving 27.6 g of KH_2PO_4 and 28.39 g of Na_2HPO_4 (both ≥98 % purity, Sigma Aldrich) in 1000 mL of distilled water. The ultrapure double distilled water (18 MΩ cm) was obtained from a SimplyLab water system (DIRECT-Q3 UV, Millipore). This part of the work was performed in collaboration with the group of prof. Paolucci at the University of Bologna (Italy), which is specialized in the applied electrochemistry.

During the electrochemical measurements, the CeO_2/GC electrode's surface contact with the working solution was delimited by o-ring to the area of 0.5 cm^2 (circle of 0.8 cm diameter). A conventional three-electrode cell assembly consisting of an Ag/AgCl reference electrode and a platinum wire counter electrode was used. The working electrode was either an unmodified glassy carbon electrode (GC) or a glassy carbon modified by CeO_2 film (CeO_2/GC). CV was taken by an AUTOLAB potentiostat interfaced to GPES software. Prior to the ECL characterization, the CV measurements were performed to estimate the position of the redox peaks. The cyclic voltammograms were taken with the scan rate of 100 mV/s in a potential window of 0–1.4 V. The test measurements with $Ru(bpy)_3^{2+}$ chromophore and TPrA co-reactant were performed on CeO_2/GC and GC electrodes to analyze the ability of cerium oxide to work as an electrode in such system. The ECL signals have been recorded in CA mode at potential 1.4 V. To amplify the photoluminescent signal, the photomultiplier tube (PMT, Hamamatsu R4220p) with bias voltage of 750 V was placed above the cell inside of a dark box and inserted in a dual-exit monochromator (ACTON RESEARCH model Spectra Pro2300i).

3. Results

3.1. Interaction of glycine and sarcosine with cerium oxide

3.1.1. Glycine on single-crystalline cerium oxide based surfaces

This chapter is dedicated to the results and their discussion obtained in the course of an experimental study of glycine adsorption on cerium oxide films of different stoichiometry and composition by means of SRPES, XPS with a laboratory source, RPES, and NEXAFS. The ordered stoichiometric $CeO_2(111)/Cu(111)$, partially $CeO_{1.7}(111)/Cu(111)$ and fully reduced $Ce_2O_3(111)/Cu(111)$ surfaces, and mixed oxide $Ce_6WO_{12}(100)/W(110)$ were chosen as the model substrates. Glycine was deposited by evaporation in vacuum on the oxide films kept at 25 °C. Preparation of the substrates and molecular adlayers is described in detail in the Chapter 2.6. The thermal stability of glycine bound to cerium oxide-based films was studied after annealing at 75, 100, 125, 150, 175, 200, and 250 °C.

Results - RPES, SRPES, XPS

Changes in the redox state of the cerium cations on the surface of the oxide films were tracked by analysis of the RPES VB features corresponding to the Ce^{3+} and Ce^{4+} resonances (for instance, see Fig. 2.1.4 in the Chapter 2.1.2). Results for CeO_2 and $CeO_{1.7}$ films before and after glycine deposition and then after thermal treatment are shown in the Figure 3.1.1 a-d. The RER ratio was not estimated for Ce_2O_3 and Ce_6WO_{12} since the Ce^{4+} centers are absent in these films; for these surfaces, only resonance enhancements $D(Ce^{3+})$ were analyzed and plotted in the Figure 3.1.1 e, f. The RER values change remarkably after deposition of glycine molecules (Fig. 3.1.1 a, b). In particular, the reduction (RER value grows from about 0 to 0.6) of CeO_2 and reoxidation (RER ratio drops from 8.4 to 5.4) of $CeO_{1.7}$ surface were observed. The similar extent of an increase of $D(Ce^{3+})$ and decrease of $D(Ce^{4+})$ for the glycine adlayer on CeO_2 (Fig. 3.1.1 c) may account for the Ce^{4+} cations reduction on the surface due to water desorption or charge transfer from the adsorbed molecule to the oxide. The RER behavior for the $CeO_{1.7}$ film after glycine deposition is quite different. While resonance enhancements $D(Ce^{3+})$ decrease notably after molecular adsorption, almost no changes are detected for $D(Ce^{4+})$ (Fig. 3.1.1 d). First of all, the $D(Ce^{3+})$ change accounts for the signal attenuation by the adlayer and then reflects the molecular bonding character, which might be closely related to electron transfer from the Ce^{3+} ions to the molecule or filling the surface vacancies by oxygen atoms from the molecule. Simultaneously with a decrease of D(Ce^{3+}), an increase of D(Ce^{4+}) is expected, but the experimental findings evidence against this hypothesis. Apparently, we have to take into account the vacations mobility in the reduced cerium oxide films.[105] For glycine adlayers on Ce_6WO_{12} and Ce_2O_3, the molecular deposition causes a rapid decrease of the D(Ce^{3+}) signals (Fig. 3.1.1 e, f) similarly as for $CeO_{1.7}$.

In course of thermal treatment of the glycine/CeO_2 system, the RER ratio remains stable with an average value of 0.6 (Fig. 3.1.1 a). In the case of glycine on $CeO_{1.7}$, the RER slowly increases from 5.4 to 6.0 at 150 °C, and then rapidly decreases to 3.5 at 250 °C (Fig. 3.1.1 b). The behavior of D(Ce^{3+}) versus annealing temperature for glycine adlayer on Ce_6WO_{12} (Fig. 3.1.1 e) indicates a slight rising of the signal up to 150 °C, and then the slope of the line became steeper for higher temperature. For glycine/Ce_2O_3, the D(Ce^{3+}) signal (Fig. 3.1.1 f) is stable between 75 and 200 °C, similarly as for $CeO_{1.7}$ (Fig. 3.1.1 d), and increased further after annealing at 250 °C.

No detectable changes in the Ce 3d core level spectra were observed after adsorption of glycine molecules (Fig. 3.1.2) for any of the studied films. After substrate annealing at 250 °C,

Table 3.1.1. *Effective thickness of glycine adlayers [d_{Gly}, Å], molecular coverage [Θ, ML], binding energy [E_b, eV] of the components of the N 1s and C 1s core levels, and the energy difference [Δ, eV] between components D and C of C 1s.*

oxide film/temperature	d_{Gly}, Å	θ_{Gly}, ML	E_b(N 1s), eV component A	E_b(C 1s), eV components D, C	Δ(C 1s), eV
CeO_2(111)/Cu(111)					
25 °C	3.8	0.21	400.1 (A)	286.4 (D), 288.8 (C)	2.4
75 °C	2.3	0.23	400.1 (A)	286.4 (D), 288.8 (C)	2.4
$CeO_{1.7}$(111)/Cu(111)					
25 °C	2.2	0.23	400.5 (A)	287.1 (D), 289.7 (C)	2.6
75 °C	2.1	0.20	400.7 (A)	287.2 (D), 289.8 (C)	2.6
Ce_2O_3(111)/Cu(111)					
25 °C	3.6	0.34	400.9 (A)	287.3 (D), 289.9 (C)	2.6
75 °C	3.9	0.36	400.9 (A)	287.4 (D), 290.0 (C)	2.6
Ce_6WO_{12}(100)/W(110)					
25 °C	2.8	0.29	400.40 (A)	286.9 (D), 289.4 (C)	2.5
75 °C	2.3	0.16	400.40 (A)	286.8 (D), 289.3 (C)	2.5

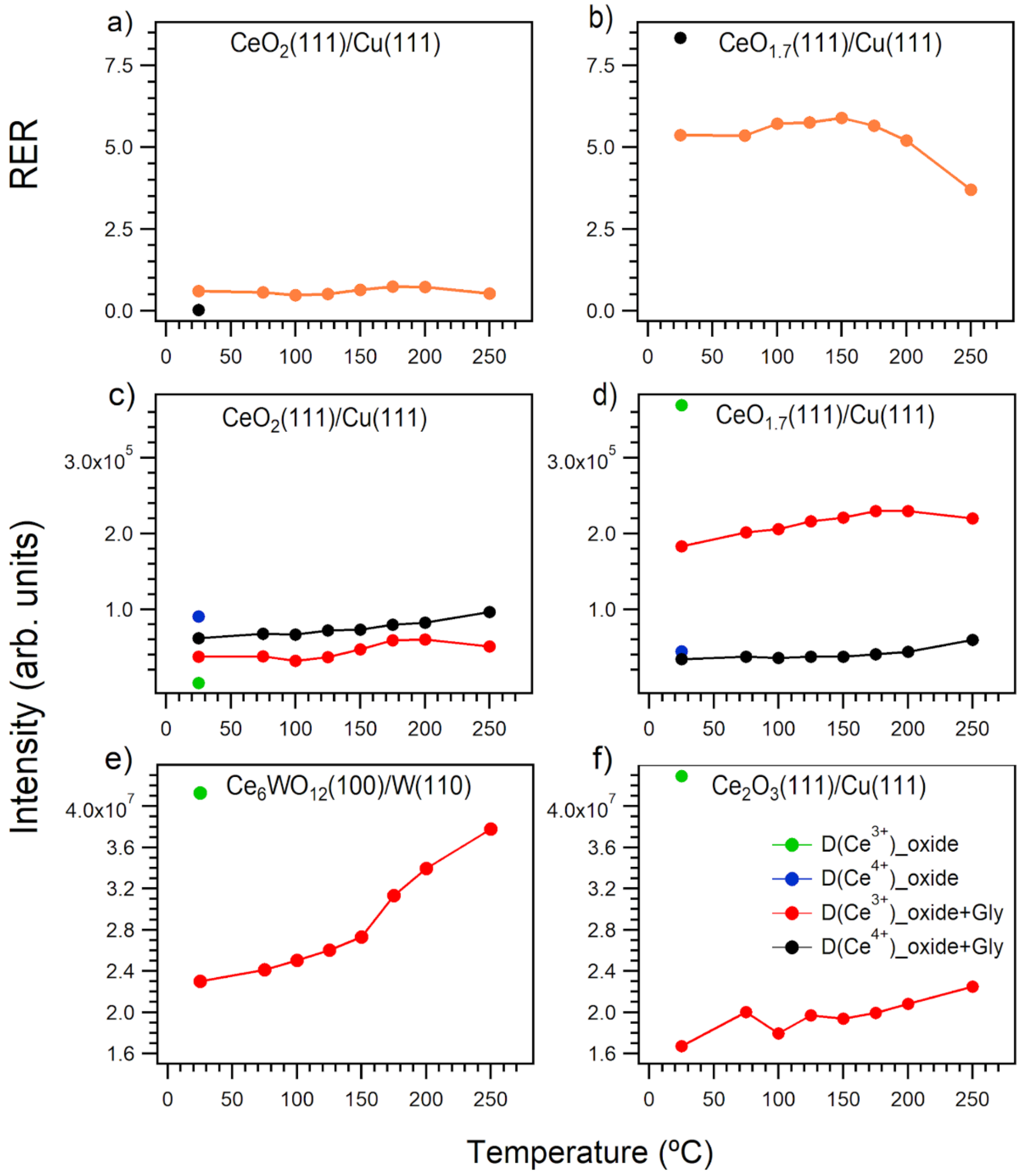

Fig. 3.1.1. *The resonance enhancement ratio D(Ce^{3+})/D(Ce^{4+}) of the glycine adlayer on (a) CeO_2 and (b) $CeO_{1.7}$ versus annealing temperature. The resonance enhancements D(Ce^{3+}) and D(Ce^{4+}) of the glycine on (c) CeO_2 and (d) $CeO_{1.7}$ as a function of annealing temperature. The resonance enhancements D(Ce^{3+}) of glycine on (e) Ce_6WO_{12} and (f) Ce_2O_3 as a function of annealing temperature. The black, blue and green circles represent the corresponding values for the clean oxide surfaces before deposition of glycine.*

minor changes of the Ce 3d spectral shape were observed, confirming slight reduction of CeO_2 and reoxidation of $CeO_{1.7}$ and Ce_2O_3 films within the whole oxide film thickness.

Adsorption chemistry and thermal stability of glycine molecules on cerium oxide-based surfaces were studied, analyzing the N 1s and C 1s core level spectra. After deposition of glycine, one component N 1s peak and two component C 1s core level were observed for all

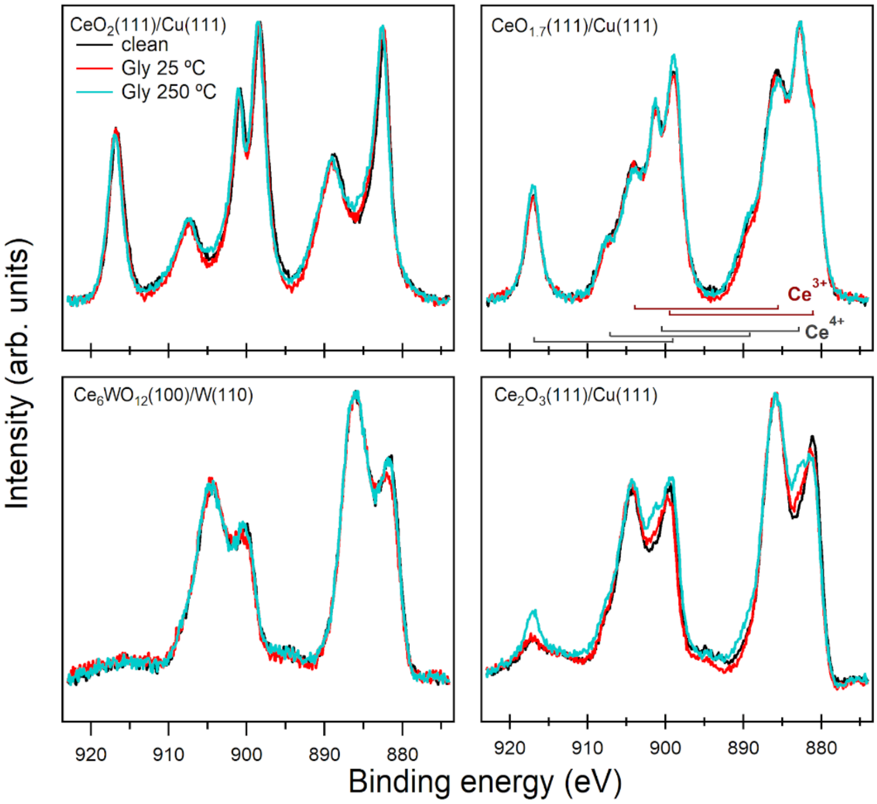

Fig. 3.1.2. *Ce 3d spectra of the cerium oxide films before and after glycine adsorption at 25 °C and after substrate annealing at 250 °C. The spectra are normalized to the maximum intensity. Photon energy 1486.6 eV.*

surfaces (Figs. 3.1.4 and 3.1.5), corresponding well to the molecular structure of glycine[107] (see Fig. 1.3.1 a). The integral intensity of C 1s and N 1s signals and their fitted components after different experimental steps are shown in the Figures 3.1.6 and 3.1.7 a, respectively. The binding energy of the N 1s and C 1s components are shown in the Table 3.1.1. The values are stated for systems at 25 °C and after annealing at 75 °C to ensure desorption of weakly bound molecules. The minor shift of the peak positions at different experimental steps was linked to the semiconducting band bending effect, similarly as in the published works.[70,108,109] The N 1s peak (*A*) was assigned to the nitrogen atom of the glycine amino group.[58,64] The C 1s components at high (*C)* and low (*D)* binding energy were assigned to carbon atoms of the carboxylic group and α-carbon connected to the amino group, respectively. The symmetric shape and comparable width of components C and D point on two different chemical states of carbon atoms of glycine well resolved by SRPES. The energy difference between the two components of C 1s for all substrates (see Table 3.1.1) is smaller than the one of 2.9 eV observed for glycine molecules in gaseous state,[107,110] and for glycine adsorbed in a neutral state on Pt(111),[111] indicating chemisorption of the molecule on the cerium oxide. Moreover,

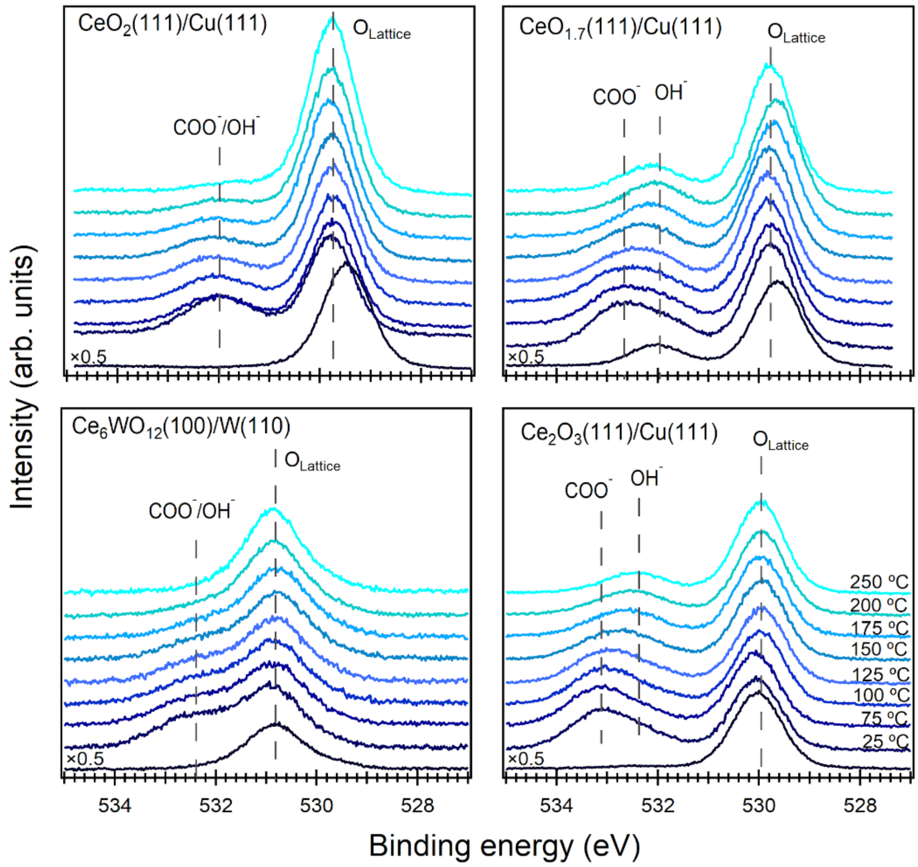

Fig. 3.1.3. *O 1s core level spectra of cerium oxide surfaces before (bottom line) and after glycine deposition plotted as a function of annealing temperature. Photon energy 630 eV.*

this value was found to be different for CeO_2 (2.4 eV) and Ce_2O_3 (2.6 eV) films (Table 3.1.1), which might be related to different bonding of the molecule to the surface or by different chemical impact of the Ce^{4+} and Ce^{3+} cations on glycine adlayers. Since position of the N 1s peak (400.1 eV) on the CeO_2 surface corresponds well to the neutral amino group[58,61,111,112] and is shifted toward high binding energies (400.4 – 400.9 eV) on the reduced surfaces due to the band bending effect, we concluded that the amino group of the molecule is not directly involved into reaction with the surface at 25 °C. Existence of the neutral carboxylic group COOH in the molecule is often confirmed in the literature by appearance of two features in the O 1s spectra separated by 1.8–1.9 eV.[107,110,111] In the case of glycine adlayer on Pt(111) substrate, they were found at binding energies 531.4 and 533.3 eV.[111] In the current work, only one O 1s component, besides the lattice oxygen, was observed at 532.0 and 532.4 eV on CeO_2 and Ce_6WO_{12} surfaces, respectively (Fig. 3.1.3 and Table 3.1.2). Thus, we suggest that glycine is bonded to these surfaces via deprotonated carboxylic group. The O 1s spectra of clean $CeO_{1.7}$ and Ce_2O_3 surfaces (Fig. 3.1.3) contain a minor peak component at about 532.0 and 532.5 eV, respectively, which is assigned to the adsorbed OH groups on Ce^{3+} centers.[67] After deposition of glycine, the OH peak slightly grows, and a new component at 532.9 eV ($CeO_{1.7}$) and 533.3 eV (Ce_2O_3) appears. Since the energy difference between the OH and carboxylic carbon group components (0.8-0.9 eV) is smaller than the value reported for the molecule in a neutral state (1.8 eV), we suggest that also for the reduced cerium oxide films glycine is bound via carboxylate group.

Annealing at 75 °C caused a slight intensity decrease of the N 1s and C 1s core levels (Fig. 3.1.6) without significant change of the shape (Figs. 3.1.4 and 3.1.5) for all substrates. Moreover, the intensity reduction is more pronounced for the C 1s signal. Thermal treatment at higher temperatures resulted in two distinct behavior of spectral features for glycine on CeO_2 and Ce_6WO_{12} at one side and molecular adlayers on $CeO_{1.7}$ and Ce_2O_3 at the other. The shape of the C 1s spectra reveals only minor changes for the CeO_2 and Ce_6WO_{12} films accompanied by an intensity decrease (see Fig. 3.1.5), which is even more pronounced after annealing at 150 °C (Fig. 3.1.6). Apparently, the amount of chemisorbed molecules on the surface is decreasing due to glycine desorption with possible decomposition. Interestingly, the C 1s signal decreases almost twice faster than N 1s one, especially after 150 °C, which supports the idea of molecular desorption. For glycine on Ce_6WO_{12}, the complete desorption of the adlayer is observed after 250 °C (Fig. 3.1.6).

Table 3.1.2. *The binding energy of the O 1s core level components.*

Surface	Components of the O 1s core level		
	$O_{Lattice}$	OH^-/COO^-	COO^-
CeO_2	529.5	–	–
Gly/CeO_2, 25 °C	529.8	532.0	–
Gly/CeO_2, 250 °C	529.8	531.7	–
$CeO_{1.7}$	529.6	532.0	–
Gly/$CeO_{1.7}$, 25 °C	529.8	532.0	532.9
Gly/$CeO_{1.7}$, 250 °C	529.8	532.1	532.8
Ce_2O_3	530.0	532.5	–
Gly/ Ce_2O_3, 25 °C	530.1	532.5	533.3
Gly/ Ce_2O_3, 250 °C	530.0	532.5	–
Ce_6WO_{12}	530.8	–	–
Gly/Ce_6WO_{12}, 25 °C	530.8	532.4	–
Gly/Ce_6WO_{12}, 250 °C	530.9	532.0 – 532.4	–

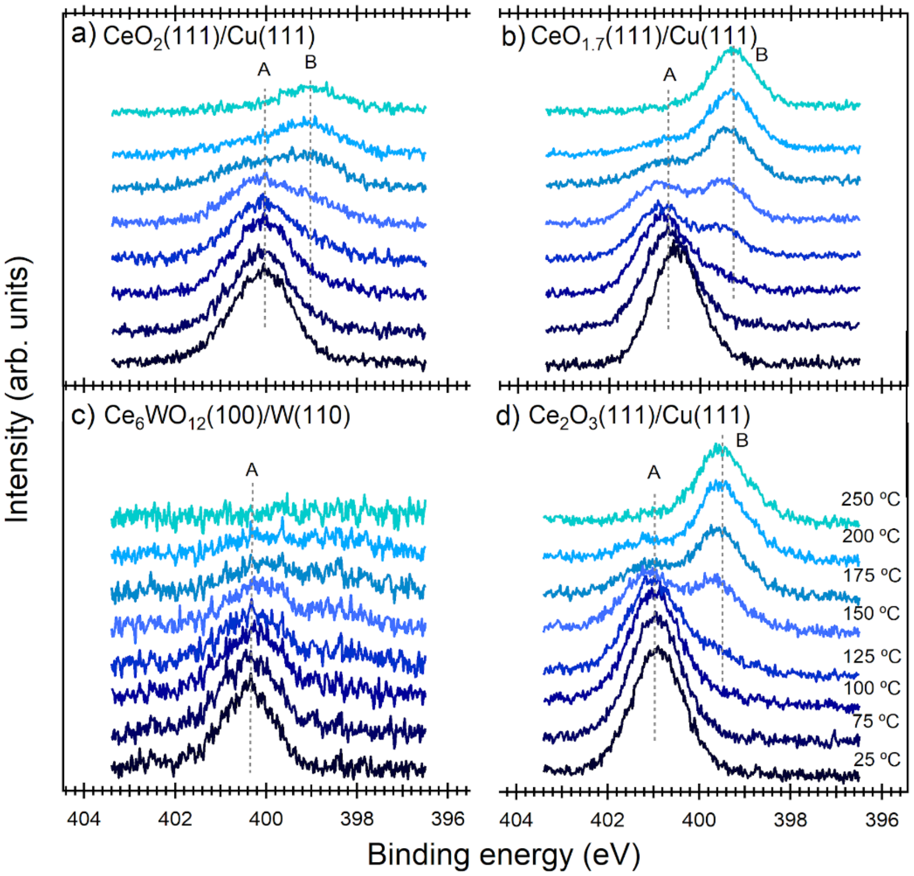

Fig. 3.1.4. *N 1s spectra of glycine adsorbed on cerium oxide surfaces: a) CeO_2, b) $CeO_{1.7}$, c) Ce_6WO_{12} and d) Ce_2O_3. The dark blue color corresponds to the glycine adlayers at 25 °C. With the annealing at the 75, 100, 125, 150, 175, 200 and 250 °C color of the lines gets to the light blue. The photon energy 475 eV.*

Similarly, the N 1s and C 1s intensities for the glycine/$CeO_{1.7}$ system have decreasing character first up to 125 °C, then remain stable and continue to slightly decrease again after 250 °C (Fig. 3.1.6). It worth noticing that the behavior of the N 1s and C 1s curves is almost parallel during thermal treatment, differently from the ones for CeO_2 and Ce_6WO_{12}, confirming the surface chemical reaction and desorption of the decomposed species. Starting from 75 °C, a new component E (binding energy 288.3 – 288.8 eV) appears (Fig. 3.1.5), which clearly grows at the expense of the component C (Fig. 3.1.7). Intensity of the peak D (287.0 eV) does not change substantially from 125 to 200 °C, then decreases again. The N 1s spectra from glycine/$CeO_{1.7}$ start to change shape also after annealing at 75 °C (see Fig. 3.1.4). A new component B appeared at low binding energy (~399.7 eV), which growth is accompanied by the intensity decrease of the component A (400.7 eV). Evidently, the electronic environment of the amino group changed considerably in course of the surface chemical reaction between

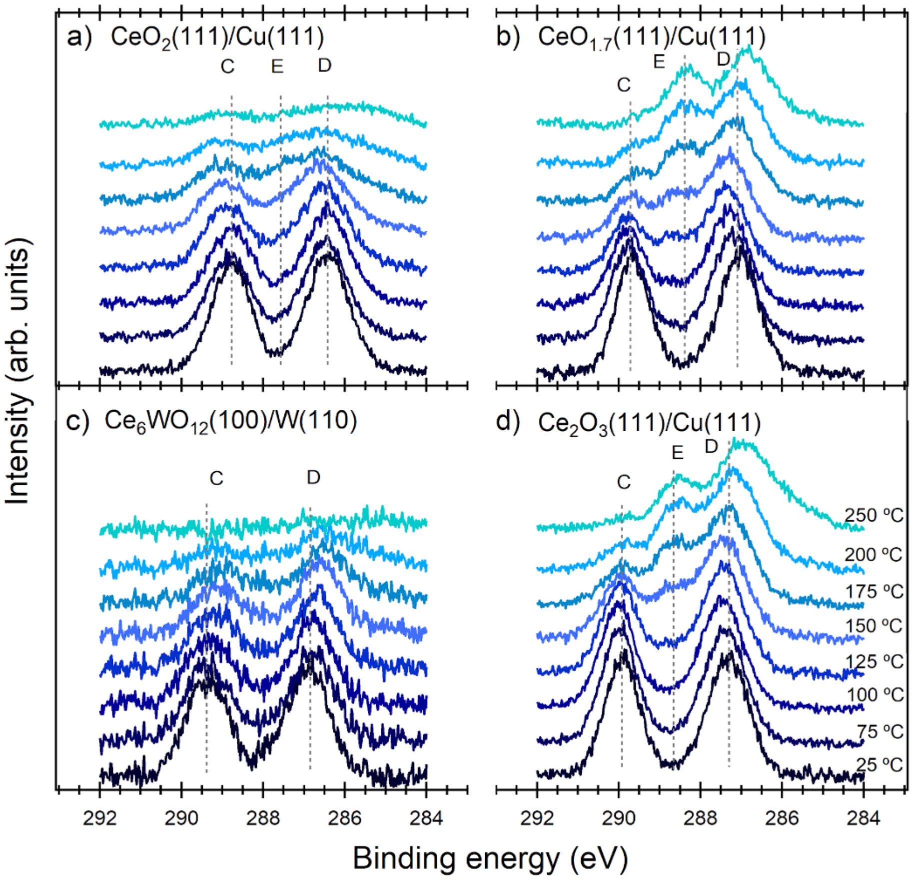

Fig. 3.1.5. *C 1s spectra of glycine adsorbed on cerium oxide surfaces: a)* CeO_2*, b)* $CeO_{1.7}$*, c)* Ce_6WO_{12} *and d)* Ce_2O_3*. The dark blue color corresponds to the as deposited glycine adlayers at 25 °C. With the annealing at the 75, 100, 125, 150, 175, 200 and 250 °C color of the lines gets to the light blue. The photon energy 410 eV.*

glycine and cerium oxide after thermal treatment. The possible explanations are the deprotonation of the amino nitrogen atom or its bonding to the oxide surface via hydrogen atoms.[67,108] The behavior of the C 1s and N 1s peaks from glycine adlayer on the Ce_2O_3 film is similar, but the decrease of the integrated intensities is smaller (Fig. 3.1.6), confirming the higher surface coverage by adsorbed species during the thermal treatment formed by integral molecules and/or decomposition products. The component D of C 1s is the most stable (Fig. 3.1.7). Its intensity decreases by about 20 % throughout all annealing steps, while in the case of glycine/$CeO_{1.7}$, it drops by more than 40 %. Another difference is that the intensity of the peak A in N 1s spectra after glycine deposition is higher than intensities of the single components C and D in C 1s spectra. It reaches values of the C peak intensity at 125-150 °C.

It could be explained as a result of diffraction effect or by attenuation of the C 1s signal. Annealing at 175 °C gives rise to intensity increase at low binding energy side of C 1s core

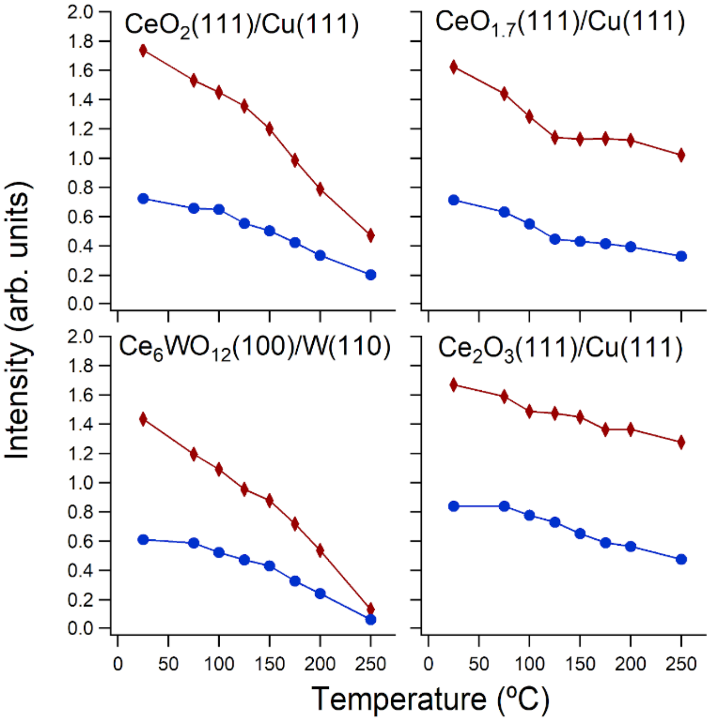

Fig. 3.1.6. *The intensity of the C 1s (brown) and N 1s (blue) core levels from glycine adlayers on cerium oxide films plotted as a function of annealing temperature.*

level, which can be represented by components F (286 eV) and G (285 eV) assigned to glycine decomposition products of CO_{ads} and CH_x character, respectively.

The intensity of carbon and nitrogen peaks for adlayers at 25 °C reveals that the C : N ratio is equal to about 2.4 for CeO_2 and Ce_6WO_{12} surfaces, fairly corresponding to the intact glycine structure. We presume that the cause of the deviation from the theoretical value 2 is a specific adsorption geometry. In particular, for the glycine molecules bound via carboxylate group and the amino group attracted by the oxide with C-C bond parallel to the surface, the partial attenuation of the nitrogen signal is expected and reflected as higher stoichiometry ratio. For $CeO_{1.7}$ the ratio is slightly lower, about 2.3, but close to the CeO_2 case. For the Ce_2O_3 surface, it is 2.0 and might be explained by different arrangement of the glycine molecule on the reduced oxide surface. The C : N ratio increased to 3.1 and 2.7 for glycine on $CeO_{1.7}$ and Ce_2O_3 films after 250 °C treatment, respectively, confirming molecular decomposition and desorption of products. Instead, it remains stable for adlayer on CeO_2, and dropped to about 2.0 on Ce_6WO_{12} (Fig. 3.1.8), supporting the idea of intact glycine desorption.

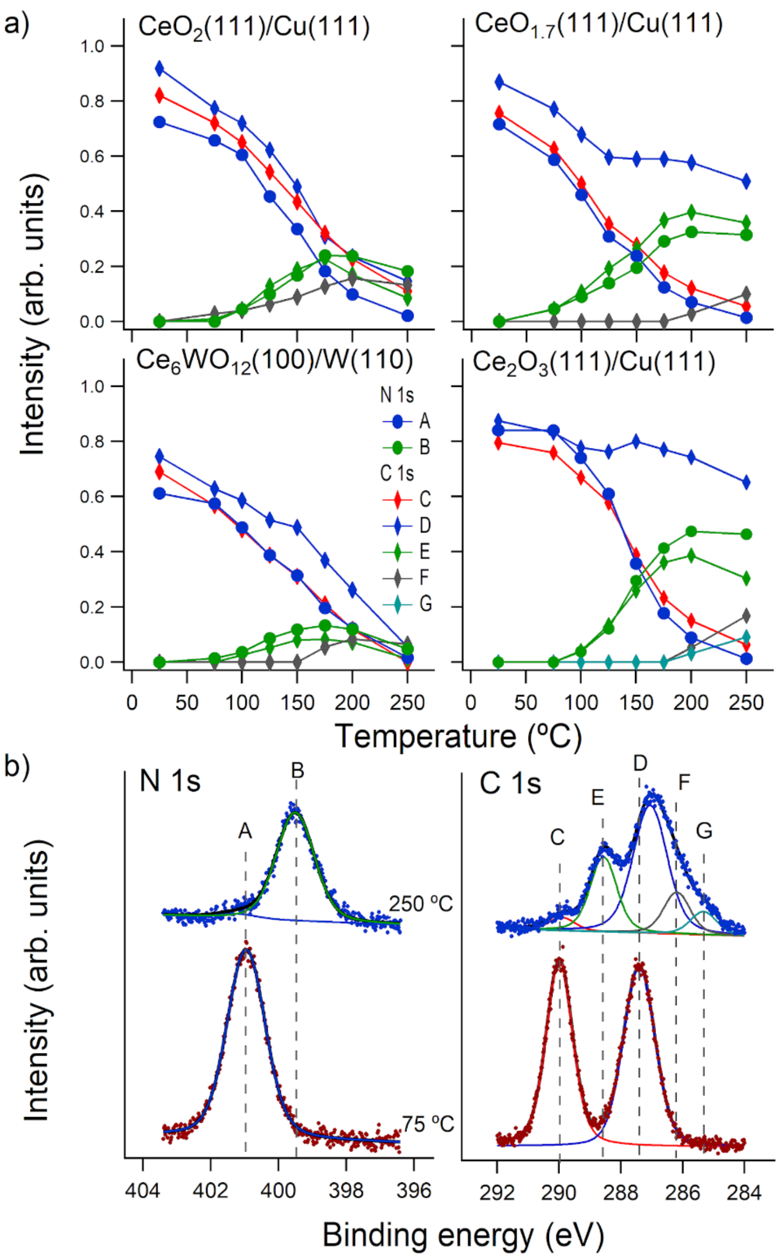

Fig. 3.1.7. *a) Intensity of C 1s and N 1s components plotted versus annealing temperature and b) example of N 1s and C 1s peak decomposition for glycine/Ce_2O_3 acquired after 75 and 250 °C. Photon energy 475 eV for N 1s and 410 eV for C 1s.*

Results – NEXAFS

The NEXAFS spectra of glycine on cerium oxide-based surfaces recorded after annealing at 75 and 200 °C are presented in the Figure 3.1.9. Positions of the peaks are collected in the Table 3.1.3. No clear angular dependence of the resonances was observed in the spectra measured at GI and NI geometries, confirming absence of the long-range molecular ordering

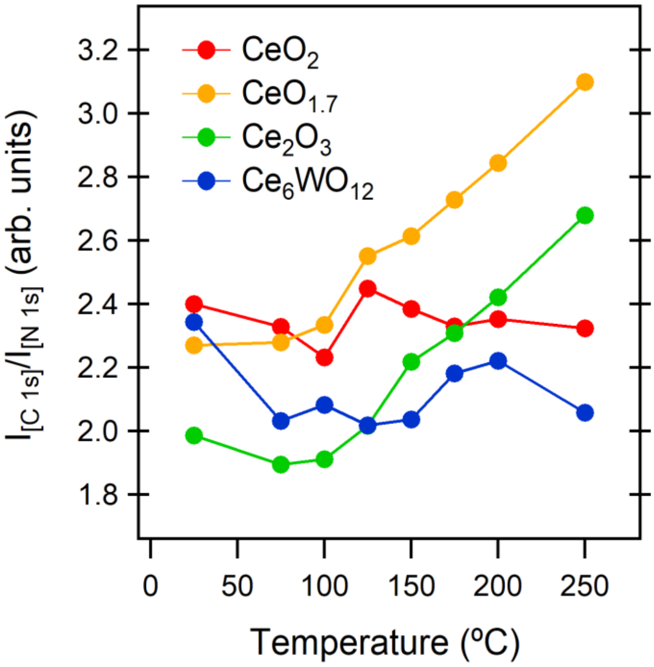

Fig. 3.1.8. *Ratio of total intensities of C 1s (photon energy 410 eV) and N 1s (photon energy 475 eV) peaks of glycine on the* CeO_2*,* $CeO_{1.7}$*,* Ce_2O_3 *and* Ce_6WO_{12} *surfaces as a function of annealing temperature.*

in the adlayer. The sharp C_1 in C K-edge spectrum corresponds to excitation of the C 1s electrons of carboxylic carbons to empty molecular orbitals of π^* symmetry.[112–114] After 200 °C treatment, the C_1' peak (288.0 eV) appears as a low energy shoulder next to C_1 peak for the CeO_2 and becomes dominant for $CeO_{1.7}$ and Ce_2O_3 surfaces. The energy shift of 0.8 eV between C_1 and C_1' is supposed to be related to the change in the electronic configuration of the carboxylic carbon atom. According to the published data, we assign the peak C_1 and C_1' to COO^- group of glycinate[113,115,116] and formate,[117] respectively. Broad features C_2 and C_3 were assigned to electron transitions to unoccupied states of σ^* symmetry and referred to C–C, C–N and C–O species, respectively.[112–114]

In N K-edge NEXAFS spectra after 75 °C annealing, only one dominant broad component (N_2) is present. According to the literature, it corresponds to the electron transition from N 1s core level to molecular orbitals with C–N σ^* character.[113,118] Less pronounced peaks between 400-404 eV were assigned to N–H anti-bonding molecular orbitals mixed with Rydberg states.[112,113] Thermal treatment at 200 °C leads to appearance of a new sharp peak N_1 at 400 eV and a broad feature N_3 at 413 eV. The N_2 peak intensity decreases and becomes comparable with N_3. Such behavior is more prominent for $CeO_{1.7}$ and Ce_2O_3 surfaces. The distinct shape of the N K-edge spectra after 200 °C suggests the change in the chemical

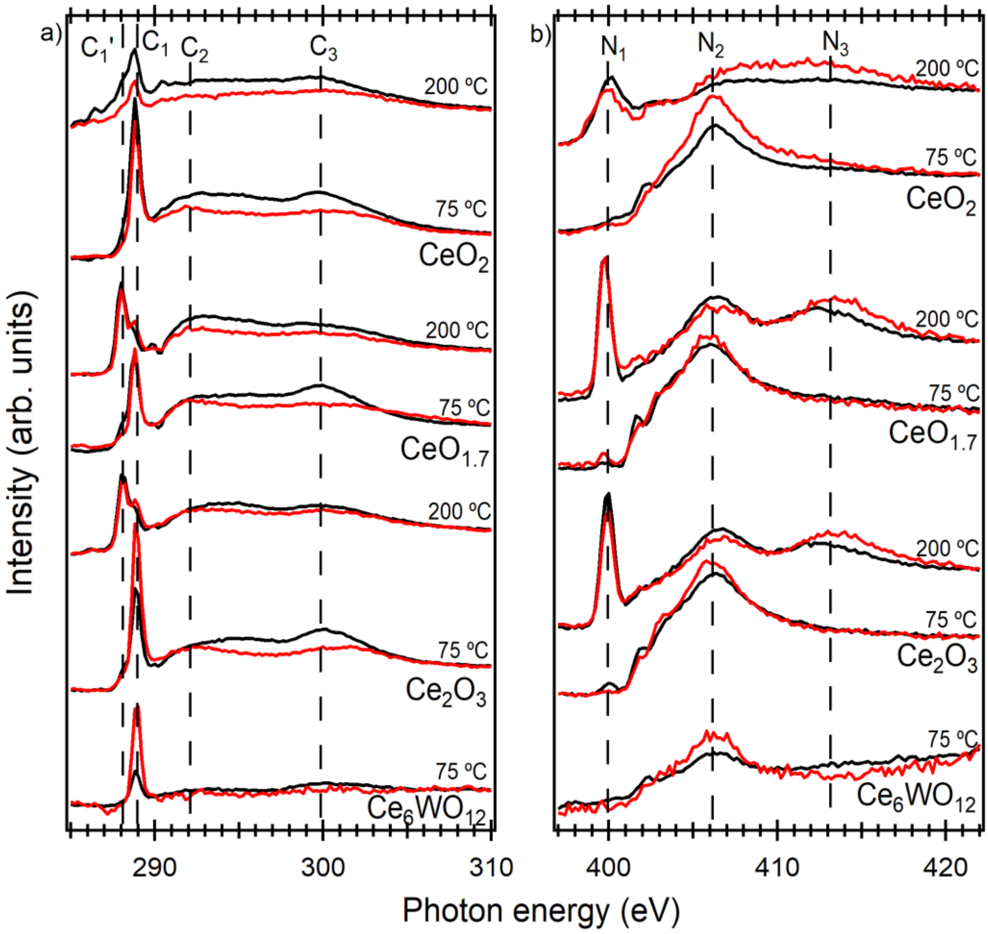

Fig. 3.1.9. *a) C K-edge and b) N K-edge NEXAFS spectra of glycine adlayers on cerium oxide films acquired after annealing at 75 and 200 °C. The spectra were recorded at GI (black) and NI (red) geometries. The oxide films* CeO_2, $CeO_{1.7}$, Ce_2O_3, *and* Ce_6WO_{12} *are listed from the top to the bottom.*

arrangement of nitrogen atoms in glycine adlayers. Nature of N_3 peak might be explained as EXAFS-like oscillations due to multiple scattering along C–N–H bond.[113]

<u>*Discussion*</u>

Four types of cerium oxide-based thin films were used in this work. Each of them has a varying ratio of Ce^{3+} to Ce^{4+} cations and different concentrations of oxygen vacancies. CeO_2 is a stoichiometric cerium oxide film with mainly Ce^{4+} cations and a negligible number of Ce^{3+} centers and oxygen vacancies at the edges of the CeO_2 terraces.[119] On the other side of the stoichiometry, there is the Ce_2O_3 film, where Ce ions are present only in 3+ state and the surface has the greatest number of oxygen vacancies.[105,106] The $CeO_{1.7}$ is an intermediate case, i.e., an oxide with a mixture of Ce^{3+} and Ce^{4+} cations and oxygen vacancies, concentration of which

Table 3.1.3. *Energy of the NEXAFS spectral components in eV and their assignment.*

substrate temperature	C K-edge C 1s → π^* (COO^-_{formate}) (C_1’), C 1s → π^* (COO^-_{glycine}) (C_1), C 1s → σ^* (C-C, C-N) (C_2) C 1s → σ^* (C-O) (C_3) C_1’, C_1, C_2, C_3	N K-edge N 1s → π^* (C-H) (N_1), N 1s → σ^* (C-N) (N_2,) N 1s → σ^* (C-N, C-H) (N_3) N_1, N_2, N_3
CeO_2(111)/Cu(111)		
75 °C	——, 288.8, 292.0, 300.0	——, 406.4, ——
200 °C	288.0, 288.8, 292.0, 300.0	400.0, 406.8, 413.0
$CeO_{1.7}$(111)/Cu(111)		
75 °C	——, 288.8, 292.0, 300.0	——, 406.0, ——
200 °C	288.0, 288.8, 292.0, 300.0	399.8, 406.4, 413.0
Ce_2O_3(111)/Cu(111)		
75 °C	——, 288.8, 292.0, 300.0	——, 406.0, ——
200 °C	288.0, 288.8, 292.0, 300.0	399.9, 406.6, 413.0
Ce_6WO_{12}(100)/W(110)		
75 °C	——, 288.8, 292.0, 300.0	——, 406.4, ——

is decreasing towards bulk.[105] The last oxide Ce_6WO_{12} contains Ce ions in solely Ce^{3+} state without oxygen vacancies.[120] Thus, we were able to investigate separately the effect of Ce^{3+}, Ce^{4+}, and oxygen vacancies on the interaction of glycine with the cerium oxide surface. The presented experimental data point out to two different scenarios of glycine adlayer formation related to the presence or absence of the oxygen vacancies in the studied films.

We suggest that the glycine molecules adsorb on CeO_2 through the formation of carboxylate in bidentate on-top configuration and the amino group attracted by oxygen anions. An adsorption geometry with the horizontal C-C bond which partially attenuates the nitrogen signal presumably accounts for the higher stoichiometry ratio C : N of 2.3 after 75 °C. The carboxylic group first deprotonates, binds by both oxygen atoms to two Ce^{4+} ions in on-top geometry (single component C in the C 1s core level at 288.8 eV binding energy), and then shares the remaining charge with the surface Ce^{4+} cations. It explains the slight surface reduction observed as the RER change of 0.6.

Previously, Lykhach et al.[121] reported that the RER value is related to the ratio of cations' (Ce^{3+} and Ce^{4+}) concentration on the oxide surface with a coefficient of 5.5:

$$RER = 5.5 \times n(Ce^{3+})/n(Ce^{4+}) \qquad \textbf{Eq. 8}$$

Since the RER value of CeO_2 was changed from 0.03 (initial RER value) to 0.61 and 0.53 (after glycine adsorption at 25 °C and after annealing at 75 °C, respectively), we can calculate for the substrate after 75 °C:

$$(0.56 - 0.03)/5.5 = n(Ce^{3+})/n(Ce^{4+})$$
$$0.10 = n(Ce^{3+})/n(Ce^{4+})$$
$$10/100 = n(Ce^{3+})/n(Ce^{4+}),$$

meaning that for every 100 Ce^{4+} there are 10 Ce^{3+} appeared.

Glycine coverage on CeO_2 was estimated to be 0.21 ML and 0.23 ML at 25 °C and 75 °C, respectively. It means that 21-23 glycine molecules can be adsorbed on 100 cerium cations leading to creation of about 10-11 Ce^{3+} centers. Thus, 1 glycine molecule should transfer about 0.5 electrons to the oxide surface, i.e., we observed a charge exchange with partial charge transfer from the molecule to the cerium cations.

It is in line with the information reported for histidine adlayers on $CeO_2(111)$,[67] where a similar electronic reduction of cerium oxide films was observed. The water desorption is excluded at this step because we neither observe the molecule decomposition nor the extraction of the lattice oxygen anions is likely at this condition. Interestingly, that Neitzel et al.[70] reported modest water desorption at 25 °C in the case of acetic acid adsorbed on CeO_2, but no ceria reduction was detected. In course of the thermal treatment, the majority of molecules desorbs and minor part (26 % as estimated from the area of the remaining N 1s signal after 250 °C) decomposes, similarly as on Ce_2O_3 (will be discussed later in detail). It worth to underline that the oxidation state of the surface Ce cations was not restored after desorption at 250 °C mainly due to the residual molecular decomposition at the Ce^{3+}, vacancies, or defect sites. Summarizing the findings, the 0.2 ML of glycine on CeO_2 at 25 °C is arranged in adlayer without long-range order and characterized by N 1s core level at 400.1 eV, two components of

C 1s (286.4 and 288.8 eV) separated by 2.4 eV, a sharp π^* resonance at the photon energy 288.8 eV in C K-edge and σ^* resonance at 406.4 eV in the N K-edge spectrum. The main spectral characteristic does not change considerably in course of thermal treatment. The stoichiometry of the molecule about 2.3 also remains unchanged; thus, we suppose that the molecules desorb from the surface in a neutral form. After desorption of the weakly bound species, the molecular adlayer diminishes fast starting from 125 °C (Fig. 3.1.6). The desorption of the intact molecules is also confirmed by the slope of the C 1s and N 1s intensity curves in the temperature range of 125 – 250 °C, where the carbon signal decreases about twice faster.

On the mixed ceria tungsten oxide, glycine adsorbs very similarly as on CeO_2. The thermal treatment causes complete desorption of the adlayer on Ce_6WO_{12}, and the intensity of the D(Ce^{3+}) reaches almost the clean surface value after 250 °C. The main spectral characteristics are very similar to the values for the glycine/CeO_2 system (see Table 3.1.1 and 3.1.3). The assumed bidentate on-top adsorption geometry with the amino group facing the surface seems to be unaffected by the fact that the carboxylate group is bound to the Ce^{3+} cations instead of Ce^{4+} as in the case of CeO_2. Any additional features related to molecular decomposition were detected in the spectra during thermal treatment. The σ^* resonance in N K-edge without pronounced π^* resonances evidences a very weak interaction of the amino group with the oxide surface.

The different scenario of glycine adsorption on the $CeO_{1.7}$ film was observed. The big advantage of this system, unlike Ce_2O_3, is the presence of both Ce^{3+} and Ce^{4+} cations on the surface. Thus the RER values can be used for the data analysis. Significant surface oxidation for this system was observed (see Fig. 3.1.1 b). The elaboration of the RER change after glycine adlayer deposition and annealing at 75 °C suggests the strong oxidation of the surface. The initial RER value of $CeO_{1.7}$ was about 8.34. After glycine adsorption it drops to 5.37, and after annealing at 75 °C it almost did not change (5.35). Using equation **(Eq. 8),** we obtain the following:

$$(5.37 - 8.34)/5.5 = n(Ce^{3+})/n(Ce^{4+})$$
$$-0.54 = n(Ce^{3+})/n(Ce^{4+})$$
$$-54/100 = n(Ce^{3+})/n(Ce^{4+})$$

It means that 54 Ce^{3+} ions were reoxidized for every 100 Ce^{4+}.

Since glycine coverage on $CeO_{1.7}$ was estimated to be about 0.23 ML and 0.20 ML (Table 3.1.1) at 25 °C and 75 °C, it means that adsorption of 20-23 glycine molecules per 100 Ce ions results in reoxidation of 54 Ce^{3+} cations. We can speculate, thus, that 1 glycine molecule should take about 3 electrons from the surface, most likely by incorporation of the carboxylate oxygens in the lattice with preservation of the molecular structure of glycinate. The glycinate with C 1s component C at 289.8 eV is bound to the surface cerium cations similarly as for CeO_2 and Ce_6WO_{12} oxides, but in this case, the oxygen atoms fill the vacancies sites on the surface. Thus, the bidentate incorporated adsorption geometry is expected for the glycine molecules adsorbed at 25 °C and stabilized in the adlayer after first annealing at 75 °C. We assume the upright position of molecules on the surface with the amino group directed outward.

Starting from 100 °C, the spectral characteristics of this system changes significantly: the new components E and B become evident in the C 1s and N 1s core levels accompanied by the appearance of π^* resonances C1' and N1 in the C and N K-edge spectra, respectively. Combining all these findings, we expect glycinate decomposition starting from 100 °C via C-C bond scission with formation of formate and methylamine species. Especially for the oxide film with both Ce^{4+} and Ce^{3+} cations, $CeO_{1.7}$, this process is likely to be accompanied by the desorption of the neutral glycine molecules as in the case of CeO_2, contributing to the intensity decrease of both N 1s and C 1s signals. Regarding the adsorbed methylamine species, an attraction of the amino group to the surface cerium cations is expected to develop in the strong bonding via partial deprotonation or dehydrogenation (component B in N 1s, Fig. 3.1.4) with possible formation of cyanide derived complexes[122,123] in the course of the thermal treatment. These species remain on the surface even after final annealing at 250 °C. Instead, the adsorbed formate species undergo a partial decomposition and possible desorption of the products. Starting from 100 °C formate appeared in the C 1s as the component E at 288.4 eV, which is expected to arrange in the similar bidentate incorporated geometry as glycinate species. During further annealing, about half of the molecules remain in this state (component E in C 1s, Fig. 3.1.5), and another part decomposes further to CO_{ads} (component F in C 1s, Fig. 3.1.5) and CH_x (component G in C 1s, Fig. 3.1.5) adsorbed species accompanied by desorption of volatile products (see Fig. 3.1.6). J. Hasselstrom et al.[112] compared acetate and glycine adsorbed on Cu(110). They showed that energy separation between carboxylic and α-carbon is 2.9 eV for acetate and 2.0 eV for glycine adsorbed on the surface. It indicates that appearance of amino group in glycine influences methyl carbon peak by 0.9 eV, shifting toward higher binding energies compared with methyl carbon in acetate.[112] The same shifting (0.9 eV) was found between methyl carbon in methane and methylamine by estimation of carbon ionization potentials.[124] Thus, we exclude breaking of C–N bond because it would result in creation of acetate CH_3COO^- and weakly bound ammonia with the shift of peak D toward low binding energy.

The NEXAFS for glycine/$CeO_{1.7}$ system taken after 75 °C annealing reminds the spectra of glycine on CeO_2 and Ce_6WO_{12}. The strong π^* resonance at 288.8 eV in C K-edge confirms the bidentate bonding via carboxylate group of glycinate to Ce cations. Moreover, the photon energy of this resonance is independent of surface adsorption sites (on-top or incorporated) and type of cerium cations on the surface (Ce^{4+} and Ce^{3+}). However, after annealing at 200 °C the spectra change remarkably (Fig. 3.1.9 a). A new π^* resonance peak appears at energy 288.0 eV in the C K-edge spectrum, which becomes more intense than the original $\pi^*_{COO^-}$ transition. We have already suggested analyzing the C 1s data the thermally induced decomposition of glycinate species, which is confirmed now by NEXAFS. The main difference between adsorbed glycinate and formate species is in specific electronic configuration of carboxylic oxygen atoms. Moreover, both contribute to surface oxidation. Analysis of the relative intensities C1' to C1 evidences that more than 60 % of glycinate decomposes to formate after 200 °C, which is in line with the relative intensity of the E to C components of the C 1s core level. Our conclusions on the assignment of the new resonance feature C1' are in good accordance with the literature data reported for adsorbed formate species. Previous works have shown that formate adsorbed on Ag(110) results in an absorption peak of π^* character at 288.3 eV.[117] Another possible product of glycine decomposition is methoxy group. It doesn't give any π^* resonance peak due to exceptionally single bond nature, but it provides a similar feature from C–H bond. Outka et al. reported that methoxy group adsorbed on Si(111)(7×7) results in sharp peaks at 288.1 and 289.4 eV from σ^*(C–H) resonances with broad σ^* (C–O) resonance at 293.0 eV.[125] Considering the fact that there is no peak around 289.4 eV in our data and that this peak is dominant in Ref.[125], we conclude that methoxy moiety was not produced on the Ce_2O_3 surface after 200 °C. A new peak N_1 that appears after 200 °C annealing was assigned to methylamine adsorbed species. Moreover, the formation of cyanide-derived complexes cannot be excluded.[122,123]

For Ce_2O_3, we suggest the adsorption of bidentate incorporated glycinate species with the upright molecules and the amino group far from the surface. The upright adsorption through the carboxylate oxygens only allows for the formation of a denser molecular adlayer of effective thickness 4.4 Å (molecular coverage of 0.36 ML, see Table 3.1.1) after 75 °C compared to glycinate on CeO_2 (effective thickness 2.3 Å and molecular coverage of 0.23 ML,

Table 3.1.1). We suppose that the upright geometry with unbound amino group, which may partially attenuate the signal from carbon atoms, is responsible for the lowest C to N ratio of 1.95 after 75 °C treatment. Moreover, the difference between C 1s components D and C is 0.2 eV higher for the glycine on Ce_2O_3 than on CeO_2, which we linked with the more crowded surface. The binding energy values of components D and C are not compared because of possible shift due to the band alignment for semiconducting surfaces. Starting from 100 °C, the glycinate on Ce_2O_3 is decomposed into formate and methylamine adsorbed species. The oxygen atoms of formate remain in the same adsorption sites filling the surface vacancies, with a carbon atom in different electronic configuration (due to C-C bond scission) evidenced by component E at 288.5 eV of the C 1s core level. Overall, the characteristic spectra are very similar to ones from the glycine/$CeO_{1.7}$ system. Moreover, the stability of the methylamine adsorbed species during thermal treatment is much more pronounced, with the formate species decomposition as in the case of $CeO_{1.7}$. The NEXAFS spectra further confirm a high activity of the reduced cerium oxide surfaces toward glycine molecule decomposition. The decomposition of glycine to formate and methylamine on reduced cerium oxide is in line with published results on thermally activated C-C bond scission for adsorbed glycine on Pt(111),[126] where N containing adsorbed species were found to be more stable than O-containing fragments.

Conclusions

The glycine adlayers on cerium oxide-based films were studied by synchrotron radiation photoelectron spectroscopy, resonance photoelectron spectroscopy, and near edge X-ray absorption fine structure spectroscopy. The thermal stability of the adsorbed molecules was investigated up to the temperature 250 °C. The main findings can be summarized as follow:

1. The glycine molecule adsorbs on CeO_2 and Ce_6WO_{12} as glycinate species via carboxylate group, the amino group attracted by oxygen anions with C-C bond parallel to the surface. The thermal annealing provokes strong molecular desorption from both surfaces above 125 °C. After final annealing at 250 °C, the ceria tungstate film was almost in the original state. Instead, the CeO_2 surface was covered by the residual adsorbed species formed in course of molecular decomposition on the defect sites.
2. The glycine adsorbs on the reduced cerium oxide films ($CeO_{1.7}$ and Ce_2O_3) in bidentate incorporated geometry with carboxylate oxygens in the vacancies sites and amino group directed outward. The bonding only through the carboxylate group allows for the formation of the dense molecular adlayer. The decomposition of glycinate on $CeO_{1.7}$

and Ce_2O_3 was observed starting from 100 °C. The formation of adsorbed formate and methylamine species is accompanied by strong surface oxidation. Annealing at temperature 100 °C and higher triggers the partial formate decomposition to CO_{ads} and CH_x species adsorbed on the surface. The nitrogen atom of methylamine is attracted by cerium cations after thermal treatment at 100 °C, which causes the chemisorption of the amino group to the oxide surface, most likely via partial deprotonation.

3.1.2. Glycine and sarcosine on polycrystalline cerium oxide

In the previous chapter, we presented the study of glycine adsorption on single-crystalline cerium oxide films prepared in well-defined UHV conditions. To make the system a step closer toward real-world conditions, further, we investigated adsorption of glycine (Fig. 1.3.1 a) and sarcosine (Fig. 1.3.1 b) on compact nanostructured cerium oxide films prepared by non-reactive magnetron sputtering *ex situ* (polyCeO_2). Deposition of the molecules was done in two ways: the first one, deposition by evaporation in vacuum, is an intermediate step between the model *in situ* sample preparation and technologically more accessible *ex situ* routines providing knowledge closely related to the research presented in the previous chapter; the second one, deposition from aqueous solution, is more applicable to the realistic conditions of the cerium oxide use in sensing systems. This chapter reveals the obtained results.

The surface morphology of the oxide films prepared by magnetron sputtering was examined by AFM and SEM microscopies (see Chapters 2.5.2 and 2.5.3 for details). After insertion in UHV system, the oxide films were cleaned by combination of ion sputtering and annealing in oxygen atmosphere. Thus, the compact polycrystalline cerium oxide films with thickness of 15-20 nm and average roughness of 1.3 nm were used as substrates for the molecular deposition of glycine and sarcosine. The effective thickness of glycine and sarcosine adlayers on polyCeO_2 films estimated from the attenuation of the O 1s core level (see Chapter 2.1.3) are presented in the Table 3.1.4. The molecular adlayers, as well as the change of the oxidation state of substrates, after deposition and then in course of the thermal treatment up to 250 °C were studied by SRPES, XPS, RPES, and NEXAFS spectroscopies.

Results - RPES, SRPES, XPS

For the glycine and sarcosine adlayers on polyCeO_2, dependence of RER ratio $D(Ce^{3+})/D(Ce^{4+})$ and the corresponding intensities $D(Ce^{3+})$ and $D(Ce^{4+})$ versus annealing temperature are shown in the Figures 3.1.10 and 3.1.11, respectively. Analysis of the RPES spectra (for instance, see Fig. 2.1.4 in Chapter 2.1.2) showed that the surface of polyCeO_2 films was almost fully oxidized with RER equal to 0-0.1 before molecular adsorption (Fig. 3.1.10). After glycine deposition by both methods, reduction of the cerium cations was observed, with RER rising to about 0.7. These results are comparable to the value of 0.6 obtained on the single-crystalline CeO_2 film covered by glycine adlayer deposited in UHV (see Fig. 3.1.1 a). However, in course of thermal treatment different behavior of RER for the two deposition techniques was observed. In the case of glycine deposition in vacuum, RER increases to about 1 at 100 °C and then reaches saturation. On the other hand, when glycine was deposited from the solution, the RER value was continuously rising to 1.65 after the final annealing at 250 °C. The same behavior was also observed for sarcosine adlayer deposited from solution on the polyCeO_2 film with slightly lower final RER of 1.5. Interestingly, for the sarcosine/polyCeO_2 system prepared in UHV the distinct character of the RER change on stepwise annealing was observed.

In particular, the RER values rise from 0.7 to 1.1 after 100-125 °C treatment and then start to decrease, reaching almost the initial value of 0.65 after 200-250 °C. To evaluate the impact of water on the surface chemistry in the case of the molecular deposition from solution, the same experiment was repeated with the H_2O covered and then dried polyCeO_2 film. The corresponding RPES VB spectra were analyzed in the same way as for the molecular adlayers.

Table 3.1.4. *Effective thickness of glycine adlayers [d_{mol}, Å], binding energy [E_b, eV] of the components of the N 1s and C 1s core levels, and the energy difference [Δ, eV] between components D and C of C 1s.*

oxide film/temperature	d_{mol}, Å	E_b(N 1s), eV components A, Z	E_b(C 1s), eV components D, C	Δ(C 1s), eV
Gly, UHV				
25 °C	2.8	399.6 (A)	286.0 (D), 288.4 (C)	2.4
75 °C	2.7	400.1 (A)	286.5 (D), 288.9 (C)	2.4
Gly, 5 mM sol				
25 °C	3.9	399.6 (A), 401.5 (Z)	286.7 (D), 289.1 (C)	2.4
75 °C	3.9	399.7 (A)	286.5 (D), 289.0 (C)	2.5
Gly, 3.33 M sol				
25 °C	38.4	400.0 (A), 402.3 (Z)	287.0 (D), 289.1 (C)	2.1
Sarc, UHV				
25 °C	5.1	399.7 (A)	286.0 (D), 288.6 (C)	2.6
75 °C	5.4	400.0 (A)	286.4 (D), 289.0 (C)	2.6
Sarc, 5 mM sol				
25 °C	3.8	400.1 (A), 402.2 (Z)	286.4 (D), 289.0 (C)	2.6
75 °C	4.8	400.1(A)	286.4 (D), 289.1 (C)	2.7

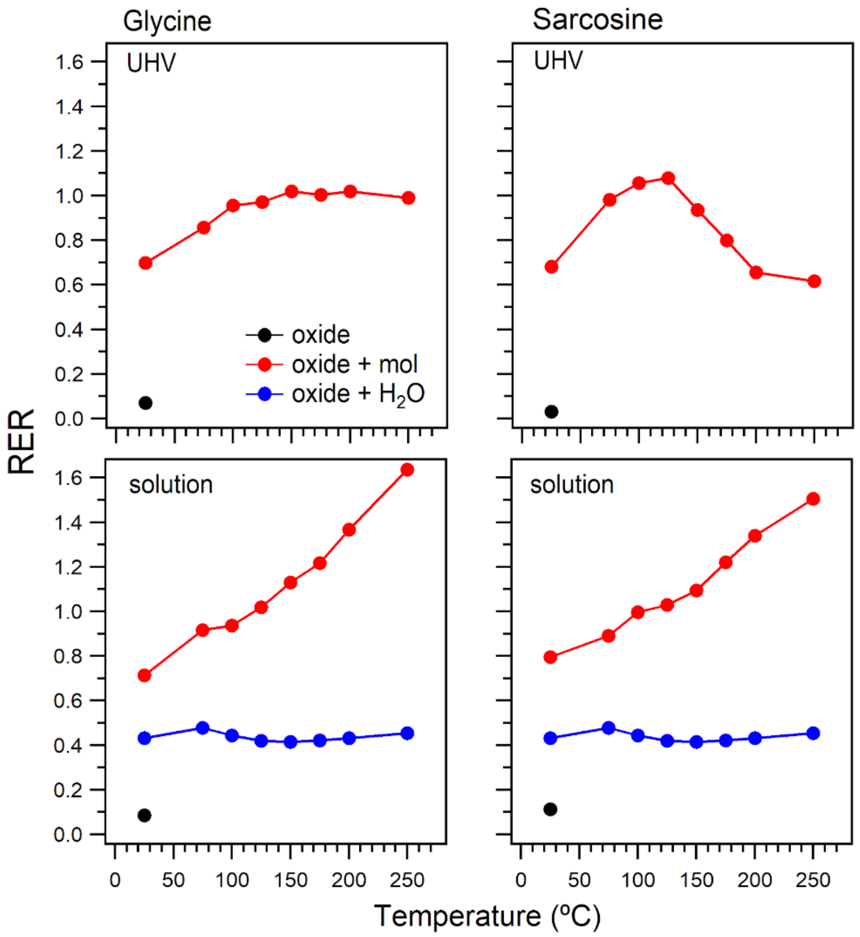

Fig. 3.1.10. *The resonance enhancement ratio D(Ce^{3+})/D(Ce^{4+}) of the glycine (left column) and sarcosine (right column) adlayers on polyCeO_2 versus annealing temperature. The top row presents RER results after molecule deposition in vacuum and the bottom row shows RER values after molecular deposition from solution. The black and blue circles represent the corresponding values for the clean oxide surfaces before deposition of the molecules and for H_2O/polyCeO_2 system, respectively.*

The RER behavior versus annealing temperature presented in the Figure 3.1.10 (blue dots) reveals the initial surface reduction after H_2O deposition with the RER value increase to 0.4, which remains almost unchanged during the thermal treatment.

The Ce 3d spectra for all systems, a typical example of the O 1s core levels for glycine/polyCeO_2, and the O 1s components intensity change with temperature are shown in the Figures 3.1.12, 3.1.13, and 3.1.14, respectively. The Ce 3d core levels (Fig. 3.1.12), providing information on the oxidation state of cerium cations within 5-7 nm of the surface, indicate slight oxide reduction after molecular deposition in UHV, which is observed as filling of the Ce 3d valley at 885 eV binding energy. Moreover, the effect is more pronounced for the sarcosine/polyCeO_2 system. In this case, the oxide reduction reached a maximum after 125 °C

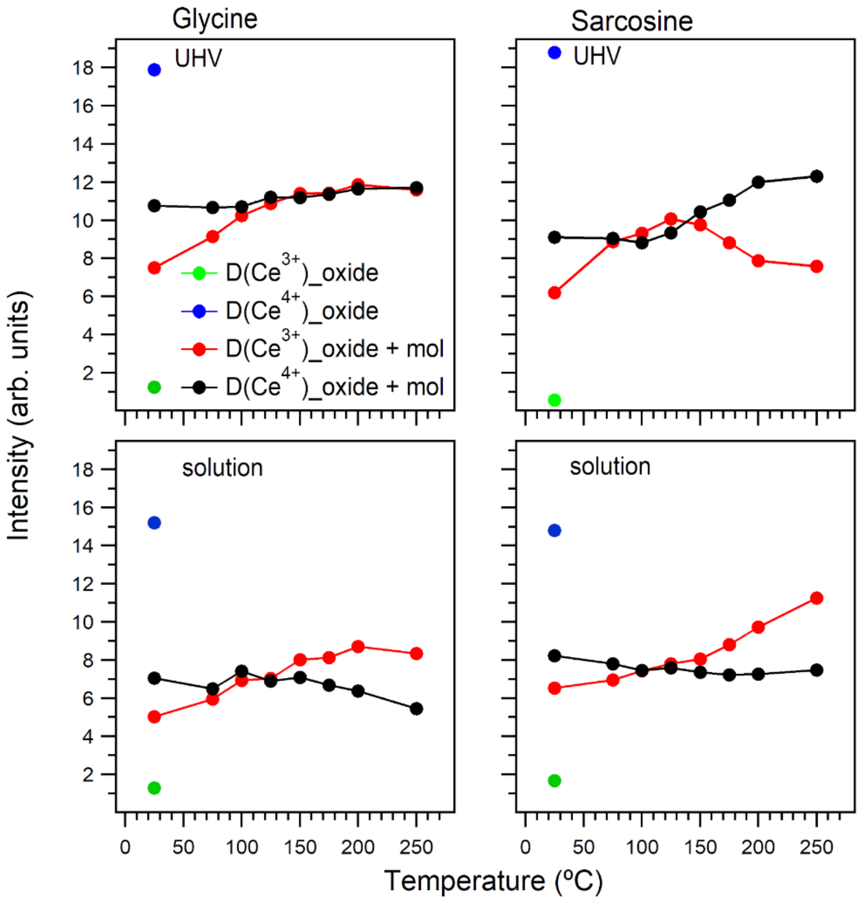

Fig. 3.1.11. *The resonance enhancements D(Ce^{3+}) and D(Ce^{4+}) of the glycine (left column) and sarcosine (right column) adlayers on polyCeO$_2$ versus annealing temperature. The top row presents values after molecule deposition in vacuum and the bottom row shows values after molecular deposition from solution. The blue and green circles represent the corresponding values for the clean oxide surfaces before deposition of the molecules.*

(the spectrum is not shown), and is restored again after final treatment, reminding the Ce 3d spectrum of the sarcosine/polyCeO$_2$ system at 25 °C, which is in line with the behavior of the RER (Fig. 3.1.10). At the same time, reduction of the oxide films for the other three systems becomes continuously stronger with annealing at higher temperatures with the maximum extent after 250 °C for glycine and sarcosine adlayers deposited from solution, again in accordance with the RER results. Thus, the glycine and sarcosine bonding to the polycrystalline cerium oxide have a strong effect both on the surface and subsurface region of the oxide film. The O 1s core level (Fig. 3.1.13) consists of two components: first, at about 529.5 eV binding energy, is assigned to oxygen atoms within the oxide lattice O$_{Lattice}$, and second, a small unresolved peak at 531-532 eV, accounts for the adsorbed species -COO$^-$ and OH$^-$. Changes in the intensity of the O 1s components, acquired with surface sensitive photon energy of 630 eV during the

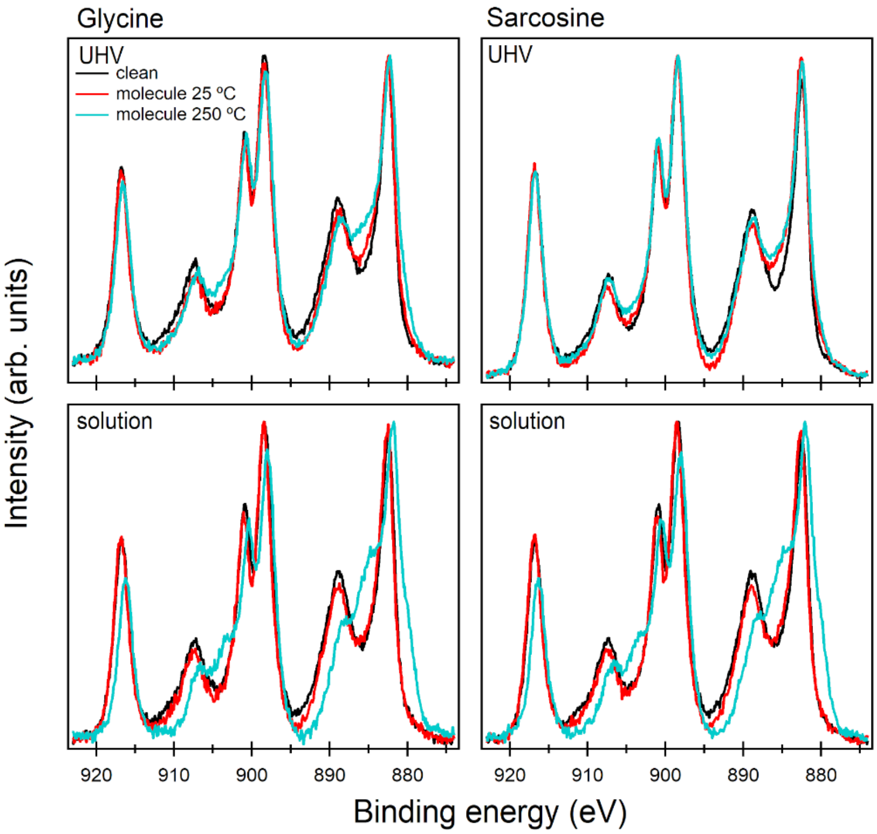

Fig. 3.1.12. Ce 3d core levels of the polycrystalline CeO_2 films before and after glycine adsorption at 25 °C and after substrate annealing at 250 °C. The top row presents Ce 3d spectra after molecule deposition in vacuum and the bottom row shows spectra after molecular deposition from solution. The spectra are normalized to the maximum intensity. Photon energy 1486.6 eV.

thermal treatment, show the same behavior for all systems apart from sarcosine/polyCeO_2. Most importantly, an increase of the lattice oxygen peak intensity at the expense of adsorbed species was observed only for sarcosine adlayer starting after 150 °C, which is in accordance with the D(Ce^{3+}) and D(Ce^{4+}) resonance enhancements change for this system (Fig. 3.1.11).

Bonding of glycine and sarcosine to the surface of the polycrystalline cerium oxide films and thermal stability of the adsorbed adlayers were studied by analysis of N 1s and C 1s spectra (Figs. 3.1.15 and 3.1.16). Two different behaviors were observed for molecules evaporated in UHV and deposited from solution. After deposition of the molecules in vacuum, only one peak is visible in the N 1s spectra (Fig. 3.1.15 a, b). Its position at about 400 eV after annealing at 75 °C is comparable with the peak A observed for the glycine/CeO_2(111) system. We assigned this peak to the nitrogen atoms from the amino group in a neutral state –NH_2. In the C 1s spectra, two components C at about 289.0 eV and D at about 286.5 eV are observed for UHV

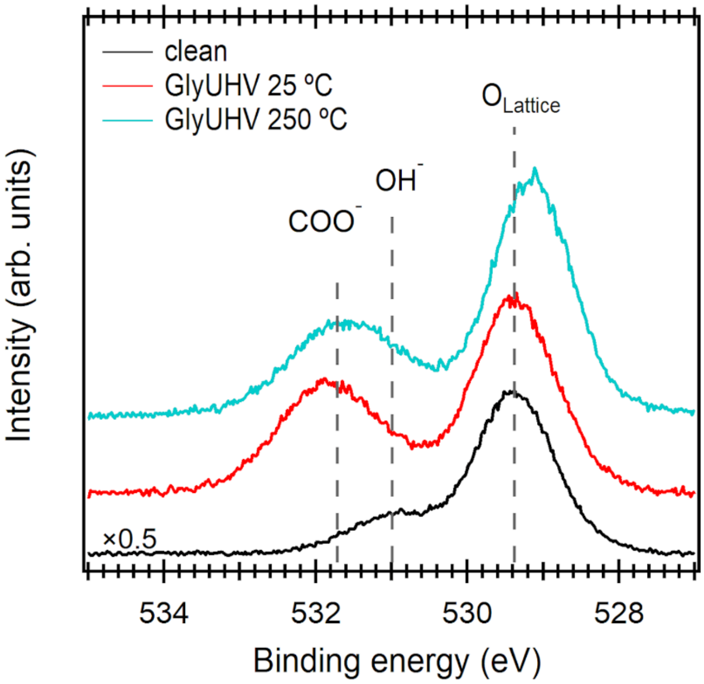

Fig. 3.1.13. *O 1s core level spectra of the polycrystalline CeO_2 film before and after glycine UHV deposition at 25 °C and after substrate annealing at 250 °C. Photon energy 630 eV.*

prepared adlayers (Fig. 3.1.16. a, b). In accordance with the published information[58,61,64] and the data presented in the Chapter 3.1.1, the component C is formed by photoelectrons from the adsorbed carboxylate groups and peak D is assigned to the rest of the carbon atoms of the molecules, which are α-carbon in glycine and α-carbon together with methyl carbon connected to the amino group in sarcosine (see Fig. 1.3.1 in Chapter 1.3). The intensity ratio D to C for glycine on polyCeO_2 was about 1 after deposition, and for sarcosine/polyCeO_2, it was estimated to be 2.4. This number for glycine/polyCeO_2 agrees well with the theoretical value for a molecule with two carbon atoms in a different chemical environment and also with the experimental data obtained for the glycine/CeO_2(111) system (see Chapter 3.1.1). The D : C ratio of 2.4 for sarcosine/polyCeO_2 differs from the expected value of 2, which can be explained by a specific adsorption geometry of the molecule bound via the carboxylic groups to the cerium oxide. The signal from the carboxylic carbon, thus, is attenuated by the rest of the molecule. The integral intensity of the N 1s and C 1s peaks as a function of the annealing temperature is shown in the Figure 3.1.17. The C 1s to N 1s intensity ratio for glycine and sarcosine adsorbed on polyCeO_2 surface at 25 °C is 2.6 and 3.8, respectively. The deviation from the theoretical values of 2 and 3 for glycine and sarcosine (see Fig. 1.3.1 in Chapter 1.3), respectively, most likely is related to the local atomic arrangement of the adsorbed molecule

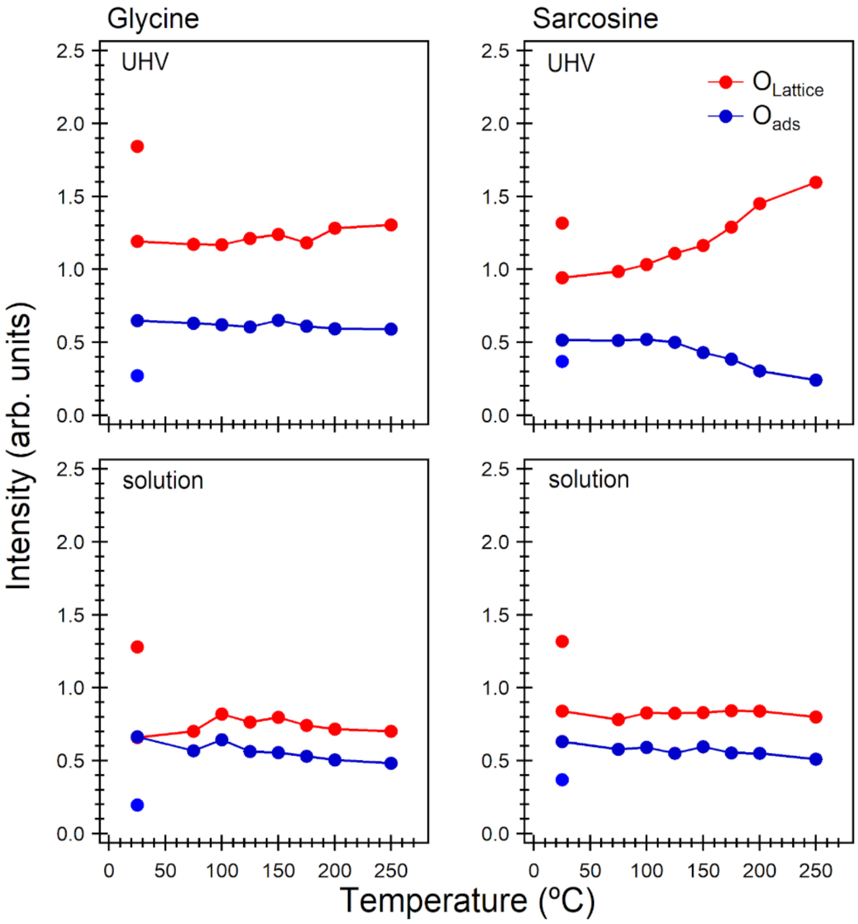

Fig. 3.1.14. *The intensity of the O 1s components versus annealing temperature: red and blue circles are lattice oxygen (*$O_{Lattice}$*) of the polyCeO*$_2$ *films and adsorbed OH*$^-$ *and -COO*$^-$ *groups (*O_{ads}*) on the surface, respectively. The top row presents values after molecule deposition in vacuum and the bottom row shows values after molecular deposition from solution. Photon energy 630 eV.*

on the polycrystalline cerium oxide, in which the signal of the atoms employed in the interface formation is attenuated by the rest of the molecule.

For the molecules deposited from the aqueous solution, two peaks are observed in the N 1s spectra after deposition of both glycine and sarcosine. The low binding energy (about 400 eV) component A was linked with the nitrogen atom of the neutral amino group, as in the case of UHV deposition.[58,61,64,112] The smaller feature at higher binding energy (401.5 and 402.3 eV for glycine and sarcosine, respectively) accounts for the protonated amino group NH_3^+, since glycine and sarcosine in aqueous solution are present in zwitterionic form.[127,128] Position of the zwitterionic nitrogen N 1s component Z for glycine is in good agreement with the previously reported results[58,61,64,111] and the reference data obtained in this work (see Figure 3.1.18) from a glycine multilayer on polyCeO$_2$ deposited from saturated solution. It is worth to underline

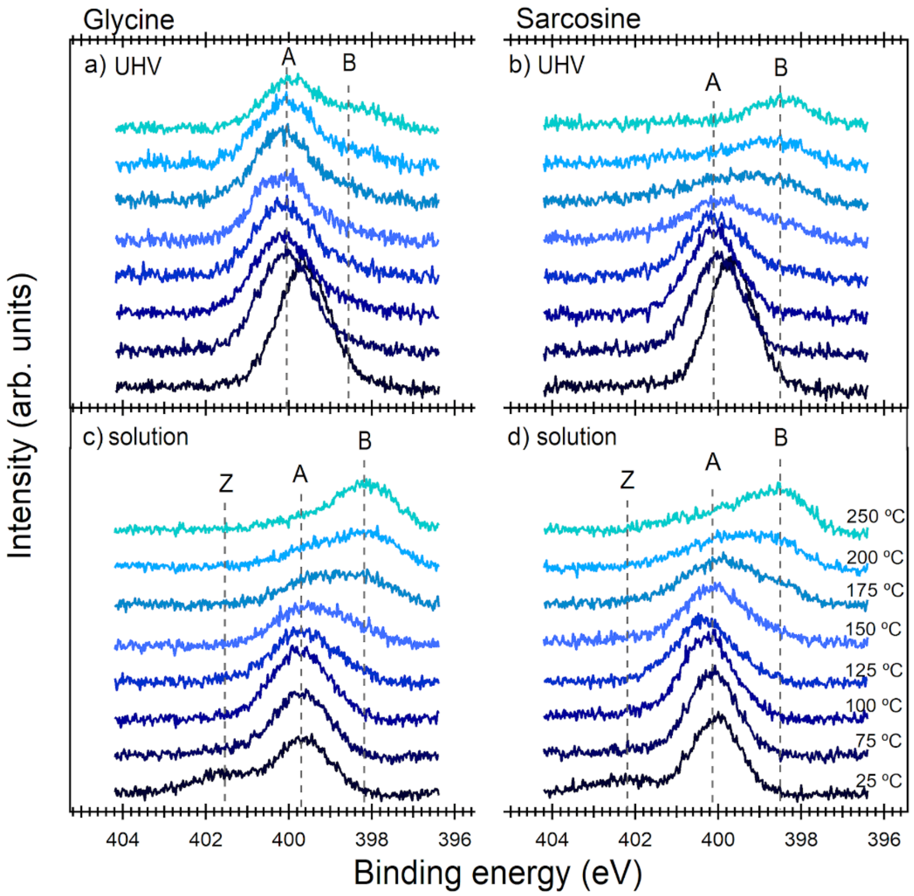

Fig. 3.1.15. *N 1s spectra of glycine adsorbed on polyCeO*$_2$ *a) in vacuum and c) from solution, and sarcosine deposited d) in vacuum and c) from solution. The dark blue color corresponds to the glycine adlayers at 25 °C. With the annealing at the 75, 100, 125, 150, 175, 200 and 250 °C color of the lines gets to the light blue. The photon energy 475 eV.*

that the small shift of the photoemission peak positions is related to the change of surface conductivity of the studied systems at different experimental steps; the effect which has already been reported in other works[70,108,109] and also observed for molecular adlayers on ordered UHV prepared cerium oxide-based films (Chapter 3.1.1). The C 1s peak consists of the two characteristic features (C and D) for glycine and sarcosine on polyCeO$_2$ films and includes one additional feature at low binding energy that was attributed to the carbonaceous species adsorbed from the solution. This component has higher intensity for the glycine/polyCeO$_2$ system. Considering the same experimental conditions, we suggest that the polycrystalline cerium oxide film is more reactive in reaction with sarcosine solution, where the preferential adsorption of the molecules dominates over the surface contamination by residual impurities. This conclusion is supported by the effective thickness of the molecular adlayers (see Table 3.1.4), which is considerably higher for the sarcosine/polyCeO$_2$ system (4.8 Å) compared to

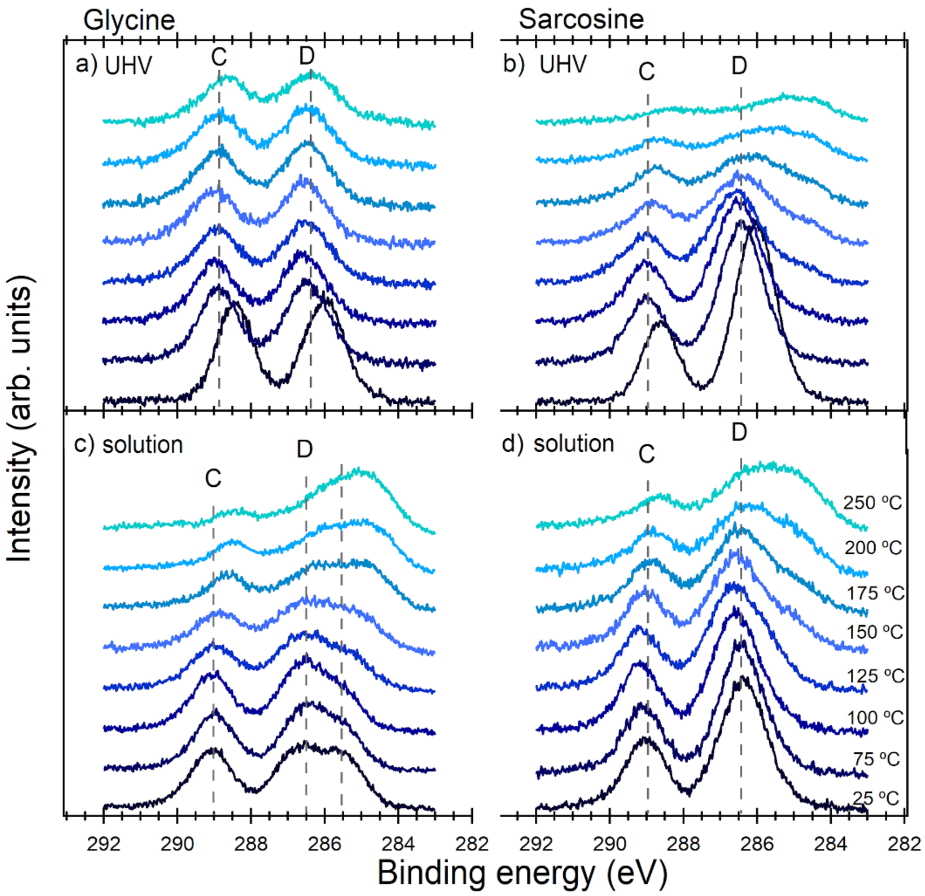

Fig. 3.1.16. *C 1s spectra of glycine adsorbed on polyCeO$_2$ a) in vacuum and c) from solution, and sarcosine deposited d) in vacuum and c) from solution. The dark blue color corresponds to the as deposited glycine adlayers at room temperature. With the annealing at the 75, 100, 125, 150, 175, 200 and 250 °C color of the lines gets to the light blue. The photon energy 410 eV.*

the value for the glycine adlayer on polyCeO$_2$ (3.9 Å) after annealing at 75 °C, which ensures desorption of weakly bound or physisorbed species.

Energy separation between the C 1s components is 2.4 and 2.6 eV (Table 3.1.4) for as deposited glycine and sarcosine on polyCeO$_2$, respectively, independently of the deposition methods. Apparently, the small fraction of the protonated molecules for adlayers deposited from solution does not affect considerably the binding energy of the C 1s components, as for purely zwitterionic multilayer this value is 2.1 eV (see Table 3.1.4 and Fig. 3.1.18). The same as in the previous Chapter 3.1.1, we conclude that glycine is chemisorbed in anionic state on the polycrystalline cerium oxide surface, since the C 1s components separation is smaller than the value observed for molecules in a neutral state (2.9 eV).[107,110,111] We are not aware of the published photoelectron spectra for the sarcosine molecules either in the gas phase or thin films.

Similarly, as for glycine adlayers on ordered cerium oxide-based films (Chapter 3.1.1), this conclusion can be further supported by the analysis of the O 1s components, i.e., by the binding energy difference between OH^- and COO^- oxygen states. In the case of glycine and sarcosine deposited on polyCeO_2, the O 1s components separation is between 0.8–1.0 eV for all studied systems (for instance, see Figure 3.1.13), which is about 1 eV smaller than the expected value 1.8-1.9 eV for a neutral carboxylic group.[107,110,111]

The thermal treatment of the molecular adlayers on polyCeO_2 leads to overall signals decrease of different extent shown as integral intensity change for C 1s and N 1s in the Figure 3.1.17, and C 1s and N 1s components behavior in the Figure 3.1.19. After treatment at 75 °C, during which the weakly bound species desorb from the surface, causing the major intensity decrease, the shape of the peaks for the UHV deposited molecular adlayers remains unchanged. A different scenario was observed for glycine and sarcosine adlayers deposited from solution

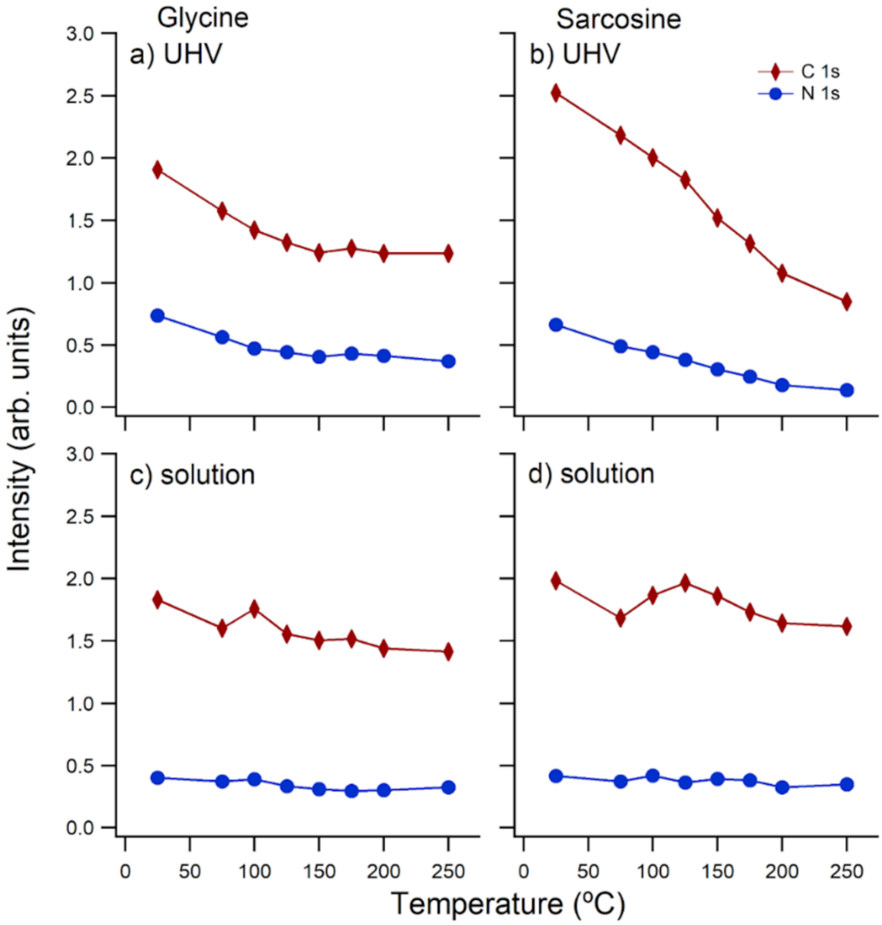

Fig. 3.1.17. *The intensity of the C 1s (brown) and N 1s (blue) core levels from glycine and sarcosine adlayers on polycrystalline cerium oxide films plotted as a function of annealing temperature. Photon energy 630 eV.*

after the first annealing step: the N 1s shoulder assigned to NH_3^+ disappears, contributing to the component A (Fig. 3.1.15 c, d). Moreover, for the glycine/polyCeO_2 system the C 1s component from carbonaceous species decreases after 75 °C (Figs. 3.1.16 c, 3.1.19 c, gray dashed line, component F).

The annealing in the range of 100 – 250 °C leads to further desorption of the molecules or species after their partial decomposition (Figs 3.1.17, 3.1.19). In N 1s spectra, a new component B appears between 398 - 399 eV binding energy, which is accompanied by a decrease of the component A, and accounts for the change of the electronic environment of the nitrogen atoms. The component B is minimal for glycine evaporated in vacuum on polyCeO_2 film and has about the same intensity for all other systems (Fig. 3.1.15). Moreover, the shape of C 1s spectra is preserved in course of the thermal treatment of UHV glycine/polyCeO_2, demonstrating the highest stability of the molecular adlayer among all samples. On other systems, a bunch of new C 1s components (E, F, and G) appears after annealing at 100 °C (Figure 3.1.19), which are directly related to adsorbed decomposition species. The following components assignment is suggested: E is formate, F is CH_x, and G is carbonates species. It has to be underlined that the suggested fitting procedure applied to the C 1s core levels represents only one of the possible scenarios of molecular decomposition and an exact component assignment is rather ambiguous. For glycine and sarcosine deposited from the solution, in particular, the total intensity of the N 1s and C 1s signals is rather stable (Fig. 3.1.17 c, d), but the shape of the spectra differs substantially after final annealing (Figs. 3.1.15, 3.1.16). These observations bring to the conclusion that molecules deposited from solution are decomposing on the polycrystalline cerium oxide, forming strongly bound residual species, which are likely accompanied by minor

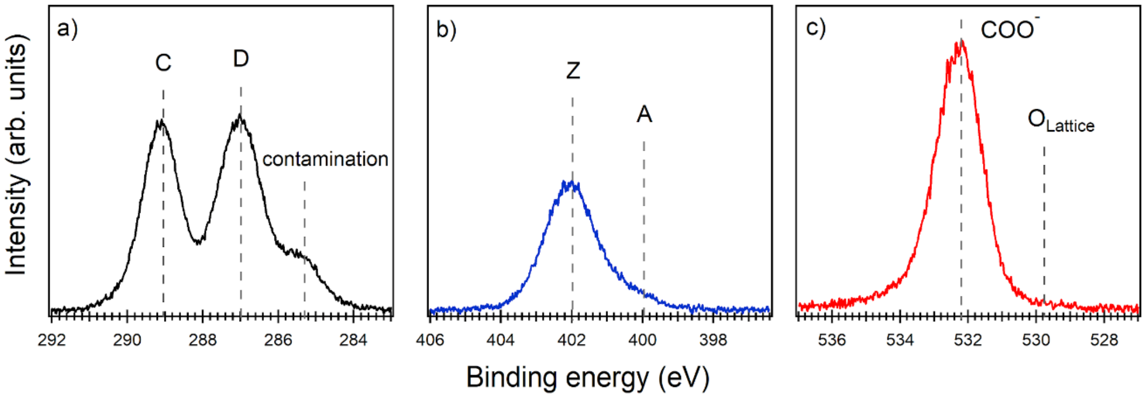

Fig. 3.1.18. *a) C 1s, b) N 1s, and c) O 1s core level spectra of glycine multilayer on polycrystalline cerium oxide film.*

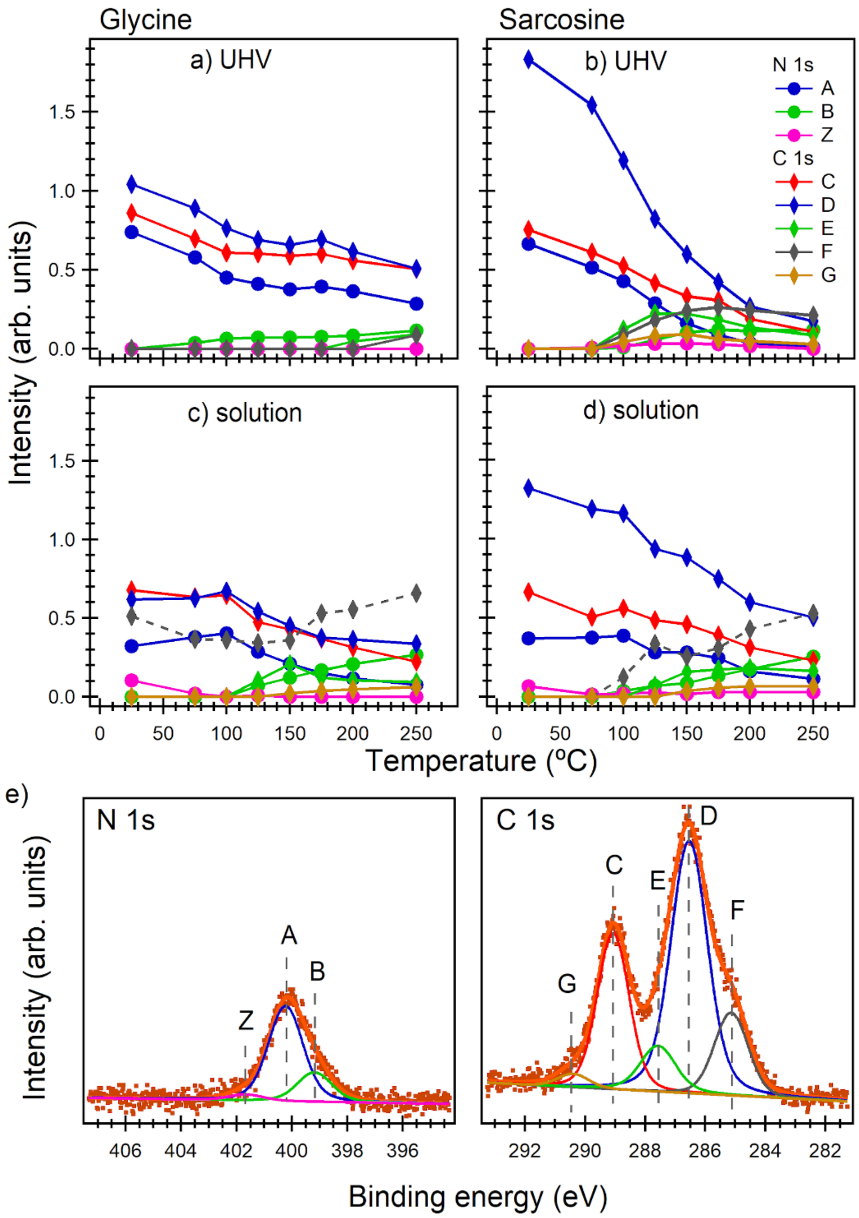

Fig. 3.1.19. *a) Intensity of C 1s and N 1s components plotted versus annealing temperature and e) example of N 1s and C 1s peak decomposition for sarcosine/polyCeO$_2$ acquired after annealing at 150 °C. Photon energy 475 eV for N 1s and 410 eV for C 1s.*

desorption of the decomposition products. Another peculiar feature to mention is a fast decrease of the C 1s signal for UHV sarcosine/polyCeO$_2$ system (Fig. 3.1.17 b), which is mainly connected with the diminishing of the component D (Fig. 3.1.19 b). Moreover, the intensity of the C 1s components C and D is not changing simultaneously with the N 1s component A as expected for integral molecule desorption. Thus, we suggest the C-N bond scission with subsequent desorption of the CH$_x$ species.

Results - NEXAFS

The NEXAFS results for glycine and sarcosine adsorbed on polycrystalline cerium oxide are presented in the Figure 3.1.20. Positions and assignments of the main peaks are shown in the Table 3.1.5. The spectra were recorded only in GI geometry since the ordered molecular adlayer formation is not expected on the polycrystalline oxide due to the grain structure of the film. The absorption spectra from UHV deposited glycine adlayer were taken after 75 and 250 °C annealing. The sarcosine adlayer deposited in vacuum was measured after 75, 175, and 250 °C. For the systems with the molecules deposited from solution the data were acquired after annealing at 75 and 200 °C. The spectra from glycine multilayer deposited from the saturated solution were measured after deposition at 25 °C. The shape of the glycine multilayer spectra and position of the main features agree well with the previously published data of solid glycine.[116] Moreover, the spectral shape and assignment of the main spectral features are very similar to the NEXAFS data for glycine and sarcosine adlayers on polyCeO_2 (will be presented later). For the multilayer glycine film, the intense π^* resonance at 288.7 eV in the C K-edge with weak σ^* features at 294.0 and 302.0 eV photon energy are very similar to UHV prepared system characterized in the Chapter 3.1.1. The N K-edge is dominating by the strong σ^* resonance at 406.5 eV, which is a characteristic feature of glycine adlayer with the weakly bound amino group (minor peak of the π^* character at 399.0 eV in N K-edge). Position of the peaks is shifted toward lower binding energy compared to the single-crystalline cerium oxide surfaces and then differs slightly throughout the thermal treatment due to the semiconducting nature of the substrate.

The sharp peak C_1 in the C K-edge spectrum was assigned to electron transition from the deprotonated carboxylic group to unoccupied π^* molecular orbitals,[112–114] similarly as for the glycine/$CeO_2(111)$ system. The broad peaks C_2 and C_3 correspond to electron excitation to unoccupied states of σ^* symmetry from C–C, C–N, and C–O species, respectively. The clear feature C_4 at 290.0-290.4 eV is tentatively assigned to the C–O electron transition to the orbitals of π^* character.[108] This peak is well visible for the UHV deposited glycine on polyCeO_2, which was the most stable adlayer according to the photoemission results. The additional bond between α-carbon atom and surface oxygen anions with or without deprotonation is suggested to be responsible for C_4 feature in the C K-edge, which substantially contributes to the stabilization of the molecular adlayer in course of the thermal treatment. The bond scission is not expected as SPRES data evidence against this hypothesis. A similar less prominent C_4 traces can also be found in the spectra from glycine on the single-crystalline cerium oxide

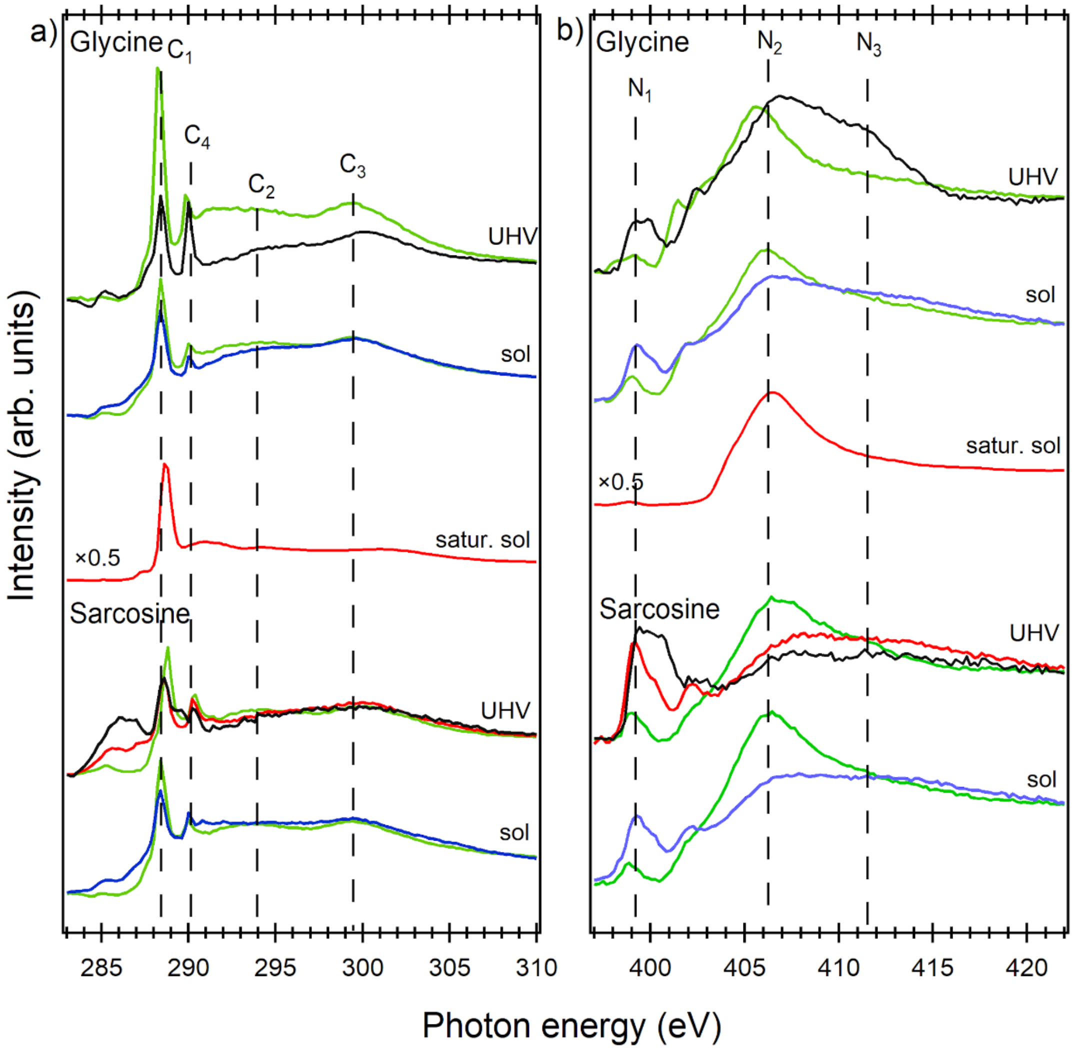

Fig. 3.1.20. *a) C K-edge and b) N K-edge NEXAFS spectra of glycine and sarcosine adlayers on cerium oxide films acquired after annealing at 75 (green), 175 (red), 200 (blue), and 250 (black) °C. Spectra of glycine multilayer are shown after deposition at 25 °C (pink). The spectra were recorded at GI geometry.*

surfaces (Fig. 3.1.9 a in Chapter 3.1.1). Thermal treatment does not lead to changes in the peak positions. However, the ratio between C_1 and C_4 features became smaller, particularly for the molecular adlayers deposited in vacuum. The minor component observed at about 286.0 eV photon energy for all systems most probably comes from the surface impurities and decomposition products.[112] Moreover, the low-energy shoulder in C K-edge for UHV deposited sarcosine accounts for the decomposition products adsorbed on the surface. The formate species, which are characterized by the π^* resonance at the lower photon energy than peak C_1 (Chapter 3.1.1), are also expected among the decomposition products.

Table 3.1.5. *Energy of the NEXAFS spectral components in eV and their assignment.*

substrate temperature	C K-edge C 1s → π^* ($COO^-_{molecule}$) (C_1), C 1s → π^* ($C\text{-}O_{surf}$) (C_4), C 1s → σ^* (C-C/C-N, C-O) (C_2, C_3) C_1, C_4, C_2, C_3,	N K-edge N 1s → π^* (C-H) (N_1), N 1s → σ^* (C-N) (N_2,) N 1s → σ^* (C-N, C-H) (N_3) N_1, N_2, N_3
Gly, UHV		
75 °C	288.4, 290.0, 295.0, 300.0	399.0, 405.8, ——
250 °C	288.4, 290.0, 295.0, 300.0	399.0, 407.0, 410.0
Gly, 5 mM sol.		
75 °C	288.4, 290.0, 294.0, 299.6	398.8, 406.2, ——
200 °C	288.4, 290.0, 294.0, 299.6	399.0, 406.2, 413.0
Gly, 3.3 M sol.		
25 °C	288.7, 291.0, 294.0, 302.0	399.0, 406.5, ——
Sarc., UHV		
75 °C	288.8, 290.4, 294.5, 300.0	399.0, 406.8, ——
175 C		
250 °C	288.6, 290.2, 294.5, 300.0	399.6, 408.0 , 415.0
Sarc., 5 mM sol.		
75 °C	288.4, 290.0, 293.6, 299.4	398.4, 406.0, ——
200 °C	288.4, 290.0, 293.6, 299.4	398.6, 406.0, 413.0

In the N K-edge spectra, after annealing at 75 °C one intense broad component N_2 at about 406 eV is present for all systems. The component was assigned to the electron transition from the N 1s level to the unoccupied molecular orbital of σ^* symmetry and referred to C-N/C-H bonds.[112,116] After annealing at higher temperatures, another peak N_1 assigned to C-H π^* resonances appears at 399–400 eV. Similarly to the glycine adlayers on ordered cerium oxide-based films (Chapter 3.1.1), it can be assigned to the decomposition products containing nitrogen atoms[112] among which the methylamine species are expected too.

Discussion

The molecular film thickness of 2.8 Å for glycine deposited in UHV (Table 3.1.4) evidences formation of the saturation monolayer on the polycrystalline surface, which is in good agreement with the value for the glycine/CeO_2(111) system (Chapter 3.1.1). The coverage θ under assumption of the molecular agglomerate growth (Chapter 2.1.3 and Fig. 2.1.6) was not estimated due to polycrystalline nature of the film. For the sarcosine molecules deposited in vacuum the effective thickness is 5.1 Å, the highest value among all samples. We suggest that the molecular structure of sarcosine, together with the specific adsorption geometry, account for this finding. The adlayers prepared from solution are characterized by effective thickness values of 3.9 and 3.8 Å for glycine and sarcosine, respectively. For the glycine/polyCeO_2 system, this value is higher than that found for the saturation glycine coverage prepared in UHV, but we suggest it accounts for both the adsorbed molecules and impurities from solution. For sarcosine/polyCeO_2, it even increased after first annealing at 75 °C to 4.8 Å, which was linked to the desorption of the impurities and molecular rearrangement on the polycrystalline oxide surface.

The same RER value of 0.7 was obtained for all systems after molecular deposition on polyCeO_2 films by both techniques, which reflects a similar chemical reaction as a result of molecular bonding to the surface. Similarly as for the CeO_2(111)/Cu(111) film, we suggest that glycine/sarcosine is bound to the polyCeO_2 surface via the carboxylate group with C-C bond parallel to the oxide lattice. Moreover, the same initial RER value of 0.7 after glycine deposition on polyCeO_2 films in UHV and from solution evidences preferential molecular adsorption independent of deposition technique and presence of impurities.

As was pointed above, the analysis of the N 1s and C 1s core levels allows to conclude that the molecules are adsorbed on the surface in the anionic state for all systems. Analysis of the NEXAFS data of molecular adlayers on polycrystalline cerium oxide films was used to support and finalize the SRPES data interpretation. In other words, the electronic structure of the molecular adlayers within the NEXAFS study was supplying information on the unoccupied electronic orbitals, allowing for the comprehensive characterization of the systems. The appearance of the peak C_4, defined as C-O bond formation between α-carbon atom of glycine and oxygen anions in the oxide, was shown to stabilize the molecular adlayer on the polyCeO_2 surface, likely due to the grain structure of the film. Among all considered systems, UHV deposited glycine adlayer on the polyCeO_2 film after initial desorption of weakly bound species remains stable in the whole range of applied temperature (see Fig. 3.1.17 a). Only residual feature of molecular decomposition (minor component B in N 1s after 250 °C in Fig. 3.1.15 a, see also Fig. 3.1.19 a) was observed in the spectra, but it can be considered as negligible in comparison to the other systems.

For all other cases (sarcosine in UHV, glycine from solution, sarcosine from solution deposition on polyCeO_2), behavior of the molecular adlayer in course of thermal treatment is rather similar with minor differences (see Figs. 3.1.15, 3.1.16, 3.1.19). It was shown that the presence of water for the adlayers deposited from solution defines the main reaction path between glycine or sarcosine and polycrystalline cerium oxide surface. First, the molecule binds to the Ce cations via a deprotonated carboxylate group (single component C in C 1s, C1 component of the C K-edge). We do not expect a strong bonding of the amino group to the surface at this stage (strong N_2 component in N K-edge). The molecular geometry is suggested to vary between all possible variations with C-C bond locally parallel to the oxide lattice. The thermally induced molecular scission is observed with partial desorption of the decomposition products. This surface chemical reaction is accompanied by the intense oxide reduction in both surface and subsurface regions (Figs. 3.1.10, 3.1.12, 3.1.14). Moreover, as was mentioned above, the oxide reduction is not an intrinsic property of the water/polyCeO_2 system, where the annealing does not cause the RER change (Fig. 3.1.10 c, d). Thus, presence of the adsorbed glycine or sarcosine on the surface can be considered as a trigger for the oxide film reduction. This process is more pronounced for the adlayers deposited from solution, for which the reduction is continuous and most likely due to the film saturation by the adsorbed OH^- groups on the surface and in the subsurface region (see Fig. 3.1.12). For the UHV glycine/polyCeO_2 system, the oxide reduction reached saturation after 150 °C, confirming the limited source of the adsorbed OH^- groups on the grain boundaries. We suggest that the main reason for the oxide reduction for adlayers on polyCeO_2 is water desorption triggered by the adsorbed molecules.

The only system for which the RER behavior differs substantially after 150 °C is UHV sarcosine/polyCeO_2, where the surface oxidation was observed, unlike all other cases (see Fig. 3.1.10 b), with simultaneous reduction of the subsurface region (Fig. 3.1.12). Again, we expect the sarcosine molecule to bind via carboxylate group at 25 °C, forming dense adlayer (effective thickness 5.1 Å) with the molecules most likely directed upward. In course of the thermal treatment, first of all, the rapid decrease of the component D of C 1s and further molecular decomposition similar to adlayers deposited from solution were observed. Thus, we suggest C-N bond scission with desorption of the CH_x group accounting for the detachment of the methyl carbon atom of sarcosine. Then the decomposition proceeds with simultaneous conversion of oxygenated carbonaceous to purely carbonaceous species filling the oxygen vacancies on the

CeO_2 grains, which is well illustrated by the intensity exchange between O 1s components in the Figure 3.1.14 b and also by D(Ce^{3+}) and D(Ce^{4+}) behavior on the annealing temperature in the Figure 3.1.11 b. In other words, the surface restores the oxidation state decomposing the adsorbed species in course of the thermal treatment. Similar behavior was observed for the glycine/$CeO_{1.7}$ system presented in the previous Chapter 3.1.1. Evidently, presence of methyl carbon in sarcosine and different adsorption geometry do not allow for the molecule stabilization via additional C-O bond formation as for UHV glycine/polyCeO_2, which is in line with the less pronounced C_4 feature in the C K-edge.

Conclusions

The adsorption of glycine and sarcosine on polycrystalline cerium oxide films was studied by synchrotron radiation photoelectron spectroscopy, resonance photoelectron spectroscopy, and near edge X-ray absorption fine structure spectroscopy. The thermal stability of the molecular adlayers was examined in the temperature range of 25 – 250 °C. The main findings can be summarized as follow:

1. The adlayer formed by UHV deposited glycine on polyCeO_2 represents the most stable molecular phase on the polycrystalline cerium oxide. The glycine molecules bound strongly to the oxide surface via the carboxylate group with minor involvement of the amino group. The grain structure of the film was suggested to be responsible for the additional C-O bond formation with C-C molecular skeleton locally parallel to the oxide lattice.
2. For UHV sarcosine/polyCeO_2 system, the dense overlayer is formed at 25 °C with sarcosine adsorbed via carboxylate group and the rest of the molecular skeleton directed outward. The water desorption was responsible for the reduction of the oxide in the subsurface region up to 150 °C. The filling of the surface vacancies throughout the decomposition of adsorbed formate or other oxygenated species is expected to account for the oxidation of the film on the surface in the temperature range 150 - 250 °C.
3. The stabilized or continuous reduction of the oxide surface in course of the thermal treatment of glycine adlayers on polyCeO_2 films deposited in UHV or from solution, respectively, was explained by the water desorption from the oxide. Apparently, the quantity of the OH groups adsorbed on the boundaries of CeO_2 grains defines the extent of the surface reduction after annealing. Most interestingly, we can conclude that the presence of the adsorbed molecules is an essential condition to observed extensive water desorption, especially for the molecular adlayers deposited from solution.

3.2. Polycrystalline cerium oxide thin film as a sensing material

3.2.1. Polycrystalline cerium oxide based electrochemical sensor for hydrogen peroxide

This chapter is devoted to the study of magnetron sputtered polycrystalline cerium oxide thin film prepared on the glassy carbon substrate as an electrode (CeO_2/GC) for electrochemical detection of hydrogen peroxide. Structure and morphology of the electrode were characterized by SEM and AFM microscopies (see Chapters 2.5.2 and 2.5.3). The 15 nm thick oxide film was examined by SRPES and XPS techniques before and after CA measurements in low (0.05 mM) and high (8 mM) concentrations of hydrogen peroxide to estimate changes in the oxidation state of ceria cations after interaction with the analyte. Reference measurements after immersion in the blank working solutions (PBS with pH 7 and concentration of 10 mM) were performed as well. More details on the CeO_2/GC electrode preparation and electrochemical measurements could be found in Chapters 2.6.1 and 2.6.3, respectively. The electrochemical detection of hydrogen peroxide was tested with and without the use of a mediator potassium ferricyanide.

Results – CeO_2/GC cathode characterization by AFM, SEM, XPS, and RPES

The morphology and structure of the CeO_2 film were analyzed by AFM and SEM (Fig. 2.5.2) and combined with the photoemission analysis of the electronic structure of the oxide surface. The polycrystalline film had a grain size between 10 and 30 nm, measured by both AFM and SEM. The surface roughness was about 1.20 nm. The oxide stoichiometry and oxidation state of surface and subsurface Ce cations were examined by measuring the Ce 3d core level and VB spectra. Ce 3d photoelectrons excited by 1486.6 eV photons with kinetic energy about 550 eV provide information about the oxidation state of Ce cations within 5-7 nm of the surface. The shape of the Ce 3d core level (Fig. 3.2.1) corresponds well to a fully oxidized ceria film with a minor contribution of Ce^{3+} centers. The average oxide stoichiometry of $CeO_{1.96}$ was determined by fitting of the Ce 3d spectrum[108] (for details, refer to Chapter 2.1.3). The analysis of resonant processes in the VB spectra excited by photon energies 121.4 and 124.5 eV (for instance, see Fig. 2.1.4) provides complementary information about the oxidation state of cerium cations in the topmost surface layer. The RER value, $D(Ce^{3+})/D(Ce^{4+})$,

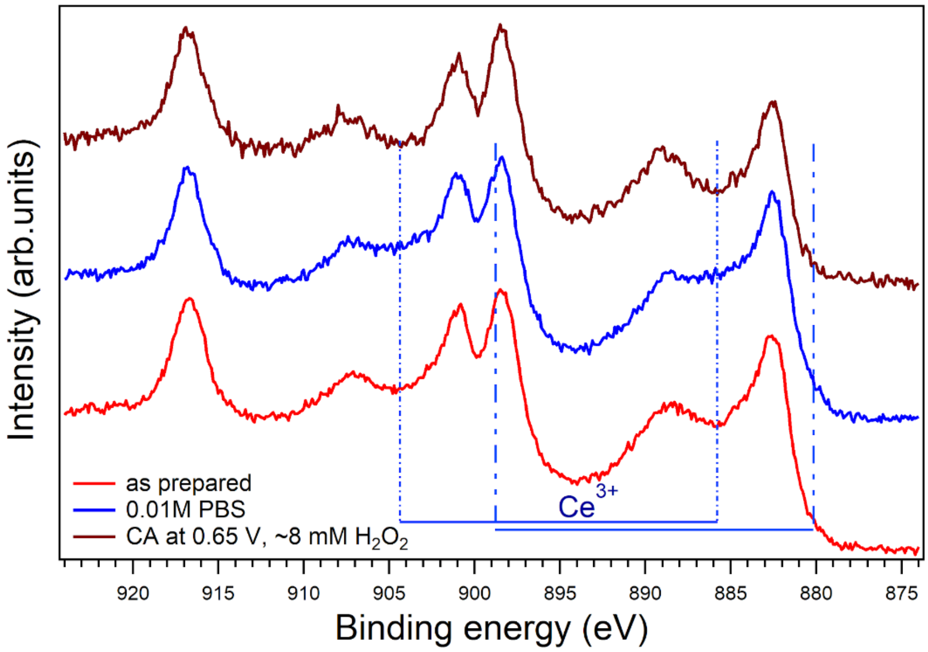

Fig. 3.2.1. *Ce 3d spectra normalized to the maxima for differently treated CeO2/GC electrodes.*

estimated from RPES was equal to 1.0, confirming the presence of Ce^{3+} cations on the electrode surface. According to Ref.[129], the RER value is 5.5 times the ratio of cerium 3+ to 4+ cations on the surface. Thus, the RER 1.0 can be expressed as 18 Ce^{3+} per 100 Ce^{4+} surface cations (Table 3.2.1). The partial reduction of the CeO_2/GC electrode was associated with the polycrystalline structure of the oxide and with the presence of a small amount of fluorine on the surface of the film (the usual contamination element for commercially available cerium or cerium oxide). As the ceria film was stored in air and analyzed in UHV without cleaning, the adventitious carbon and fluorine were detected on the surface roughly in the ratio 1.7 to 1 (Table 3.2.1). The C 1s core level is characterized by a major peak at 285.0 eV due to atomic carbon and a small component at 289.0 eV assigned to oxygenated hydrocarbons overlapping the Ce 4s signal. We do not expect a significant carbon signal from the underlying GC substrate as the oxide film is 15 nm thick. We believe that the F 1s signal at 684.5 eV originates rather from the surface than from the bulk of the CeO_2 film because it vanished almost completely in the course of the electrochemical experiment and the shape of the Ce 3d core level (Fig. 3.2.1) does not show traces of the formation of CeO_xF_y mixed oxide.[130] The O 1s core level (not shown here) is dominated by one peak at 529.6 eV assigned to the lattice oxygen from cerium oxide with a small shoulder at 531.5 eV due to adsorbed oxygenated hydrocarbons and hydroxyl groups. The immersion in PBS further reduces the surface, accompanied by adsorption of phosphorus, sodium, potassium, and chlorine. The attenuation of the Ce 3d core level expressed as a Ce 3d area relative to the signal of the clean oxide (see Table 3.2.1) is a

Table 3.2.1. *The RER values, the ratio of Ce^{3+} and Ce^{4+} cations on the surface, average cerium oxide film stoichiometry together with the relative Ce 3d area and the ratio of normalized (C 1s+Ce 4s) to F 1s XPS signals for the different experimental steps.*

CeO_2/GC	VB (RPES) RER	$n(Ce^{3+})/n(Ce^{4+})$	Ce 3d (XPS), Relative area	I(C1s+Ce4s)/I(F1s)
as prepared	1.0	18 / 100	$CeO_{1.96}$, 1.0	1.7 / 1.0
10 mM PBS	1.7	31 / 100	$CeO_{1.94}$, 0.86	4.2 / 1.0
CA at 0.65 V in 10 mM PBS + 0.05 mM H_2O_2	0.4	7 / 100	$CeO_{1.97}$, 0.68	6.0 / 1.0
CA at 0.65 V in 10 mM PBS + 8 mM H_2O_2	0.2	3.5 / 100	$CeO_{1.97}$, 0.24	20.0 / 1.0

measure of thickness of the P, Na, K, and Cl adlayer formed as a result of the working electrode interaction with PBS in the course of the electrochemical experiments.

H_2O_2 sensing by CeO_2/GC nanostructured cathode - cyclic voltammetry

The cyclic voltammetry curves of the CeO_2/GC working electrode in 200 mM PBS with and without mediator are shown in the Figure 3.2.2 in comparison with data obtained for bare GC. We observe that the CeO_2/GC electrode has a good conductibility and a larger electro active area compared to bare GC. The total surface area of the electrode has an important effect on the reaction rate for heterogeneous catalysts and is bigger in the case of polycrystalline ceria film compared to a GC electrode giving a higher CV current. Thus, the presence of the cerium oxide promotes electron transfer without the use of a mediator. The CV curve of the CeO_2/GC electrode in the presence of the mediator indicates the further enhancement of the electron transfer between working and counter electrodes. A difference of 270 mV between the oxidation and reduction peaks characteristic for the mediator on CeO_2/GC, close to the value of 320 mV on GC (Fig. 3.2.2), confirms good transducer properties of the ceria electrode. The kinetics of the electrochemical reactions on the CeO_2/GC electrode was shown to be surface-controlled and stable in the pH range from 6 to 8 (Fig. 3.2.3). With an increasing scan rate, the CV curves, maintaining the shape, gradually increase in intensity, indicating surface-controlled electrochemical behavior.[131] The oxidation current values observed in the CV curves do not

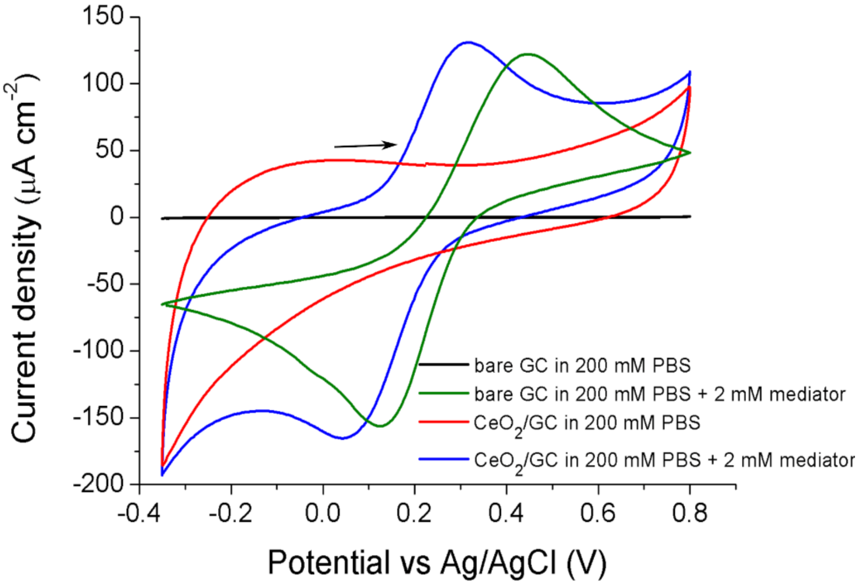

Fig. 3.2.2. *The CV curves of CeO2/GC and GC electrodes in 200 mM PBS with and without 2 mM* $K_3Fe(CN)_6$.

change considerably at pH values between 6 and 8 at 25 °C; thus, the CeO_2/GC electrode is stable under these conditions.

To explore the response of the CeO_2/GC electrode to an increasing concentration of hydrogen peroxide, the CV measurements were performed in 200 mM PBS at pH 7 with and without a mediator (Fig. 3.2.4). The 2 mM $K_3Fe(CN)_6$ redox mediator was used with the aim to facilitate the electron transfer processes in the working solution. The H_2O_2 was introduced stepwise from a minimum concentration of 5 μM to a maximum total concentration of 8388 μM. A gradual increase in the anodic current upon the addition of H_2O_2 was observed without clear peaks in the case of the working solution without the mediator. For the oxidation region, the calibration curves were plotted at potential 0.65 and 0.80 V and are shown in the inset of the Figure 3.2.4 a. Both curves increase with H_2O_2 concentration. Notice that CeO_2/GC shows a remarkable onset potential of about 0.55-0.60 V for the H_2O_2 oxidation, which is comparable with the most active systems for H_2O_2 oxidation reported to date.[132] In order to study the catalytic mechanism of hydrogen peroxide oxidation on the surface of cerium oxide, we repeated the experiment with different H_2O_2 concentrations in the presence of a redox mediator (Fig. 3.2.4 b). In line with previous results, the anodic currents, measured at 0.65 and 0.8 V, rises systematically with an increase of H_2O_2 concentration, and the maximum current values reached at 0.65 and 0.8 V are similar to the case of working solution without the mediator. Furthermore, the current increase was only negligible in the case of pristine GC, and, thus, it

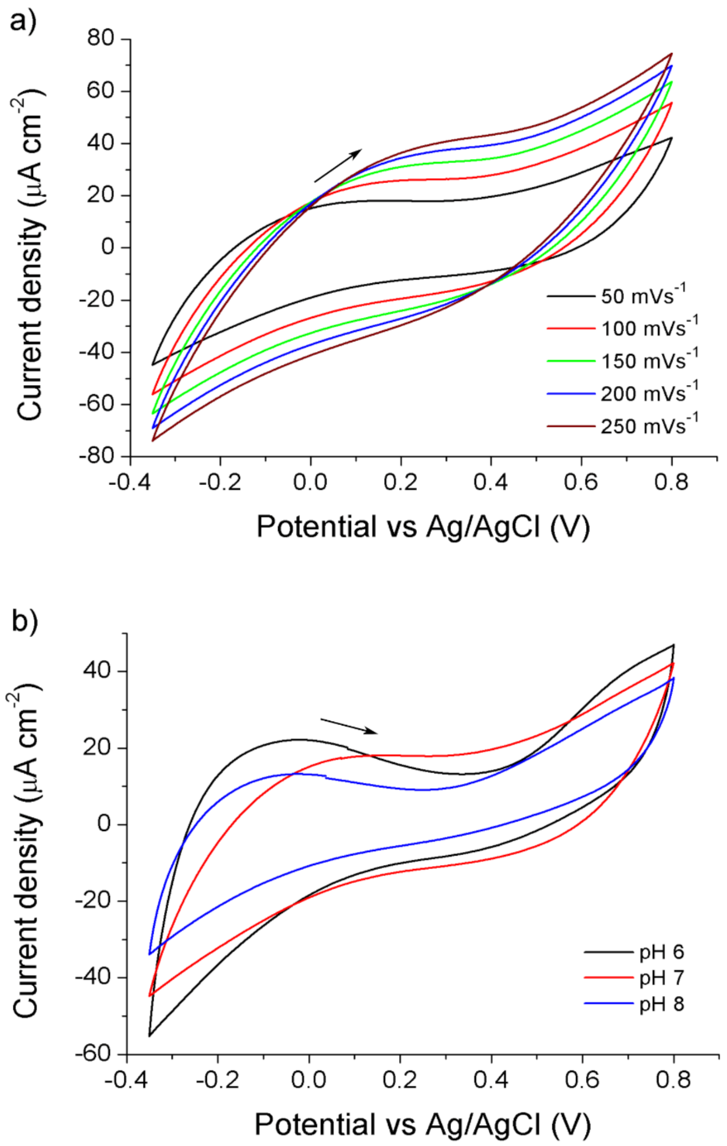

Fig. 3.2.3. *The CV curves for the CeO_2/GC electrode in 10 mM PBS with 81.2 μM of H_2O_2 measured a) at different scan rates and pH 7 and b) at different pH and scan rate 50 mVs^{-1}.*

was linked to the activity of the ceria cations on the electrode surface. Additionally, the reversible oxidation at $E_{1/2}$ of 0.2 V corresponds to H_2O_2 reaction at the mediator centers.

The magnitude of the anodic peak at 0.33 V decreases with an increase of H_2O_2 concentration (see the calibration curve at 0.33 V in the inset of Fig. 3.2.4 b). This is likely due to the competition between H_2O_2 and the redox mediator molecules in the interaction with the active sites on the electrode surface, which is not in favor of the latter. The CV performance of the CeO_2/GC electrode in the presence of the mediator confirms the important role of oxygen vacancies on the CeO_2/GC electrode surface in the reaction with H_2O_2. This statement is also supported by the chronoamperometry results presented below.

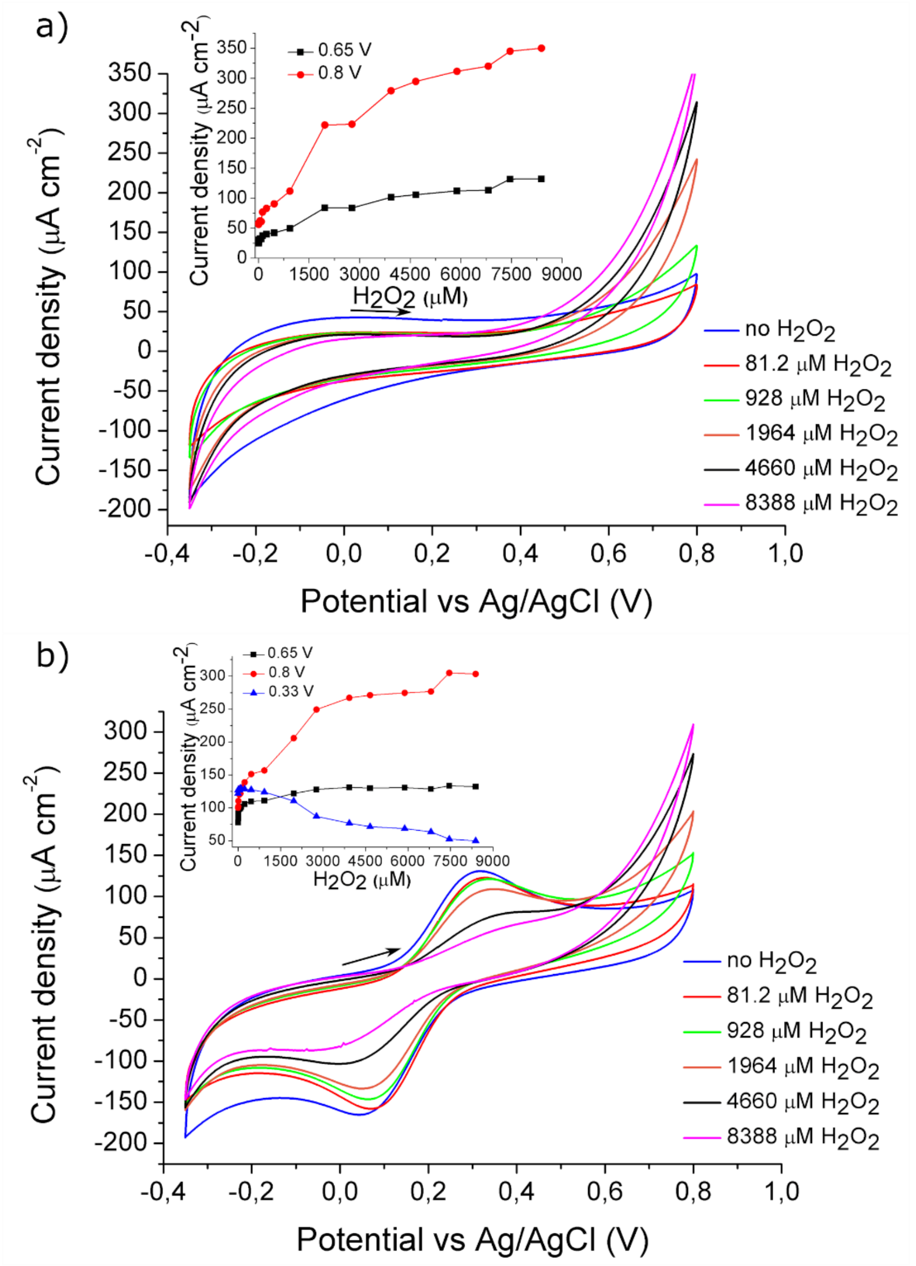

Fig. 3.2.4. *Cyclic voltammogram of a CeO_2/GC electrode as a function of H_2O_2 concentration without (a) and with 2 mM $K_3Fe(CN)_6$ (b). Insets: calibration curves plotted at potentials 0.65 V and 0.8 V (a), and at 0.33 V, 0.65 V and 0.8 V (b). The CV was measured in 200 mM PBS at pH 7 at a scan rate 50 mVs^{-1}.*

H_2O_2 sensing by CeO_2/GC nanostructured cathode - chronoamperometry and RPES

The CeO_2/GC electrode activity was characterized by chronoamperometry performed applying a constant potential of 0.65 V versus Ag/AgCl with increasing concentration of hydrogen peroxide (Fig. 3.2.5 a). In this case, 10 mM PBS working solution at pH 7 was used in order to reduce the formation of cerium phosphate, which might passivate the electrode surface and hinder the H_2O_2 oxidation on the ceria active centers.[133] The dependence of the

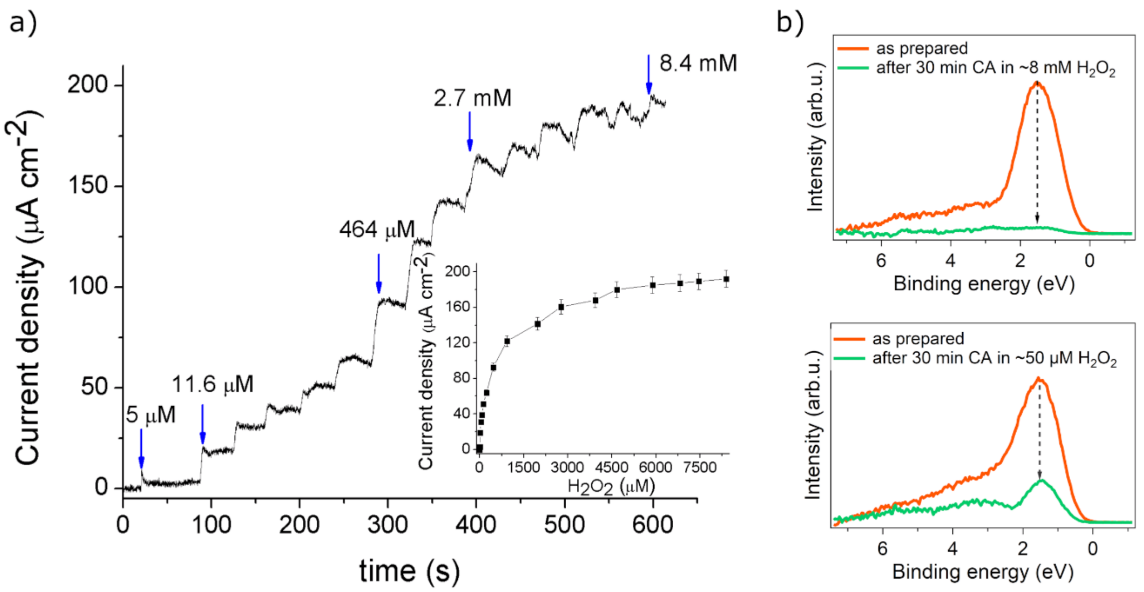

Fig. 3.2.5. *a) Amperometric response of the* CeO_2*/GC electrode at 0.65 V vs Ag/AgCl with stepwise* H_2O_2 *concentration increasing from 0 to 8 mM, in 10 mM PBS. The inset shows the dependence of the current density versus* H_2O_2 *concentration; b) Change of the D(*Ce^{3+}*) resonance VB peak measured by RPES of the as-prepared (red) films and after chronoamperometry (green) at high (~8 mM) and low (~50 μM)* H_2O_2 *concentrations.*

stabilized current value at each step on the H_2O_2 concentration, i.e., the calibration curve (see the inset in Fig. 3.2.5 a), shows the high sensitivity of the CeO_2/GC electrode to the low concentration of hydrogen peroxide. The shape of the calibration curve is typical for the enzymatic reactions, showing a Michaelis–Menten mechanism, which confirms the enzymatic-like activity of the working electrode.[134] The region where the current density increases linearly with H_2O_2 (0.005 – 0.460 mM) defines the first-order reaction of hydrogen peroxide on the CeO_2/GC electrode with a sensitivity factor of ~ 0.7 $\mu A\ \mu M^{-1}\ cm^{-2}$. Then, the current gradually reaches a plateau (starting from 4.5 mM), indicating completion of the reaction between the active sites of the electrode and H_2O_2, i.e., a further increase in the H_2O_2 concentration does not change the reaction speed anymore, and, therefore, constitutes a zero-order reaction mechanism. The Michaelis-Menten constant (*K*m) was estimated from the Lineweaver–Burk plot. It represents the catalytic efficiency of an enzyme or enzyme-mimetic material in conversion of H_2O_2 into products. Thus, for hydrogen peroxide, molecules or biomaterials with lower *K*m are more efficient, i.e., a lower concentration of H_2O_2 is needed to obtain a maximum activity of an electrode. The measured values are presented in the Table 3.2.2 and compared with recently published results of other nanozymes and HRP.

The top of the VB spectra of the CeO_2/GC electrode after chronoamperometry at low (~50 μM) and high (~8 mM) H_2O_2 concentrations are shown in the Figure 3.2.5 b, corresponding to the linear 0.05 – 0.46 mM and saturation 4.5 – 8.4 mM region of the calibration curve, respectively. The corresponding RER values and the estimated ratio of surface Ce^{3+} to Ce^{4+} cations are shown in the Table 3.2.1. The change of the D(Ce^{3+}) peak intensity after CA experiments evidences involvement of the Ce^{3+} cations in the H_2O_2 oxidation on the electrode surface. Specifically, low H_2O_2 concentration caused a strong decrease of the Ce^{3+} intensity, while this peak vanished completely when saturation is reached. Thus, the plateau in amperometric response was attributed to electrode reoxidation, i.e., the substantial decrease in concentration of the Ce^{3+} cations and oxygen vacancies on the surface of the working electrode. The average cerium oxide film stoichiometry remains unchanged after CA, while the intensity of the Ce 3d core level is strongly reduced for the H_2O_2 saturated region where the Ce^{3+} concentration is minimal (see Table 3.2.1). We can conclude that the less reactive the surface becomes, the more adsorbed species are formed on the surface in a given time. The Ce 3d core level behavior (Fig. 3.2.1) confirms the reduction of the electrode within a depth of 7 nm after PBS treatment and then partial reoxidation after reaction with H_2O_2.

Table 3.2.2. *Comparison of the Michaelis-Menten constant (Km) for hydrogen peroxide between CeO_2/GC, other nanozymes and HRP.*

Catalyst	*K*m, mM	Reference
RF CeO_2/GC	1.02	This work
CeO_2 NPs	64.60	[135]
CeO_2/NT-TiO_2	0.04	[136]
H_2TCPP-CeO_2 NPs	0.254	[137]
CeO_2 NPs	0.278	[137]
$LaNiO_3$	90.05	[138]
Au/CeO_2-chitosan film	1.93	[139]
Fe_3O_4	154	[140]
HRP	3.70	[140,141]

Discussion

The CeO_2/GC electrode acts as a catalyst in the oxidation of H_2O_2 under applied voltage. To understand the enzymatic-like activity of ceria, it is important to characterize the active centers on the electrode surface and the reaction mechanism of the H_2O_2 oxidation. According to the published data on CeO_2 NPs, the active centers responsible for the anti-oxidation behavior are proposed to be mainly determined by surface Ce sites that can coordinate the oxygen species.[17,142] Apparently, for the CeO_2/GC electrode, the possible active centers, i.e., the sites where the reaction occurs, are Ce^{4+} and Ce^{3+} cations and oxygen vacancies. In our experiments, the as-prepared CeO_2 electrode surface is partially reduced, i.e., we have a polycrystalline ceria film with a mixture of Ce^{4+} and Ce^{3+} cations on the surface. The RPES analysis shows that immersion in PBS and CV cycling further reduces the electrode surface. Once the hydrogen peroxide is introduced into the working solution under applied voltage, ceria acts as a nanozyme - adsorbing H_2O_2 promotes the electrochemical reaction by sharing its electrons. We assume that the oxidation mechanism of H_2O_2 on the CeO_2/GC electrode can be expressed by the reaction[143]:

$$H_2O_2 = O_2 + 2H^+ + 2e^-, \qquad \textbf{Eq. 9}$$

Here, apart from the electrochemical current increase connected with the formation of electrons ($2e^-$), a pH change to lower values is expected. As the detected pH change was minor and in the opposite direction, we conclude that we observed more complex behavior, such as a catalase-like activity of cerium oxide.[9,133,144–146] The mechanism of the reaction might be expressed by the equations (10) and (11), summarized by the net reaction (12):

$$2Ce^{3+} + H_2O_2 => Ce^{4+} + Ce^{4+}\text{-}O_{ads} + H_2O + 2e^- \qquad \textbf{Eq. 10}$$

$$Ce^{4+} + Ce^{4+}\text{-}O_{ads} + H_2O_2 => 2Ce^{3+} + H_2O + O_2 + 2e^- \qquad \textbf{Eq. 11}$$

$$2H_2O_2 => O_2 + 2H_2O \qquad \textbf{Eq. 12}$$

where $Ce^{4+}\text{-}O_{ads}$ denotes adsorbed oxygen species, which transforms the Ce^{3+} cations with nearby vacancy into Ce^{4+} sites. The produced electrons form the current increase in the electrochemical data, and they are accommodated by cerium cations. As a result, we obtained a solution enriched by O_2 (note that experiments were carried out in an oxygen-free solution). This oxygen may react with vacancies and be a primary reason for the ceria surface deactivation in its reaction with H_2O_2. The formation of free radicals is unlikely, but we do not have a direct

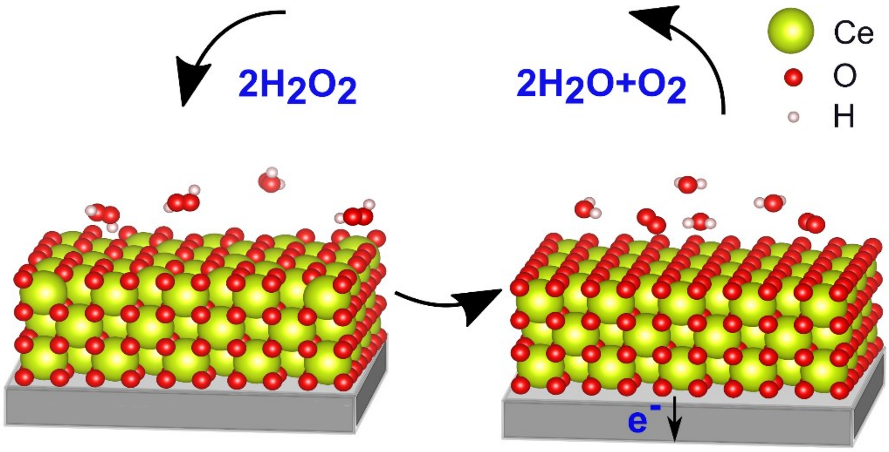

Fig. 3.2.6. *Schematic illustration of the electrochemical reaction of* H_2O_2 *on the* CeO_2*/GC electrode surface.*

proof, as in the published data.[146] Thus, the electrode surface is oxidizing during the electrochemical reaction of H_2O_2 on the surface of cerium oxide. The reaction stops when no Ce^{3+} centers are available for the reaction. Moreover, immersion in the working solution and CV cycling reduces the electrode surface and offers a way to regenerate the Ce^{3+} active centers. The schematic illustration of the electrochemical reaction of H_2O_2 on the CeO_2/GC electrode surface is shown in the Figure 3.2.6. The suggested reaction mechanism agrees well with the phase diagram of hydrogen peroxide decomposition in water,[143] where the region of pH 7 and voltage 0.65 V corresponds to a double instability of H_2O_2: reduction to H_2O and oxidation to O_2.

The typical Michaelis-Menten curve and *K*m parameter of 1.02 mM for the oxidation of H_2O_2 on CeO_2/GC indicates increased affinity of H_2O_2 for the surface of cerium oxide as compared (see Table 3.2.2) to CeO_2 NPs (64.60 mM)[135], Au/CeO_2-chitosan composite films (1.93 mM)[139] and HRP enzyme (3.70 mM)[140,141], underlining the advantage of polycrystalline surface morphology of the working electrode. The absence of a H_2O_2 oxidation peak suggests that the CeO_2 matrix acts as a good electron acceptor and confirms the direct electron exchange via the ceria surface. As suggested in previously published works,[136,138] we link it to the presence of the Ce^{3+} cations on the electrode surface. We conclude that the hydrogen peroxide reaction on the ceria electrode is managed via efficient adsorption of oxygenated species on the Ce^{3+} cations or oxygen defects and direct electron transfer through Ce^{3+} and Ce^{4+} redox centers. The observed linear response as a function of H_2O_2 concentration indicates that the CeO_2/GC electrode can be efficiently used for H_2O_2 detection over the concentration range 0.005 – 0.460 mM.

Nanostructured cerium oxide is widely used as an electrode material in electrochemistry, which is usually prepared by chemical methods, for instance, by deposition from solution.[17,18,20,24,28–31,135,136] The ceria electrode was shown to provide an enhanced electron communication between the working solution and the cathode during electrochemical deactivation of H_2O_2, independently of the absence or presence of enzymes/mediators. In agreement with our work, the published data report the oxidation of the CeO_2 particles on the electrode surface in the course of the H_2O_2 electrochemical reaction, often confirmed by red shift of UV-vis features. Our findings are in line with the work of Pirmohamed et al.[142] They confirmed the catalase mimetic properties of nanoceria and affirmed that this catalytic reaction is not equivalent for all nanoceria preparations correlating with the presence of cerium cations in the 3+ state. The authors closely linked the change in Ce^{3+} cation concentration at the NPs surface with their improved catalytic activity versus H_2O_2. It was even shown that immersion in PBS led to an improved catalase mimetic activity of cerium oxide NPs.[142] The only significant difference with respect to our results is the conclusion regarding oxidation of NPs after immersion in PBS, deduced from the red shift of UV-vis features, while we demonstrated the surface reduction of ceria films. Whether this discrepancy relates to the cerium oxide morphology (NPs versus thin films) or to different techniques of analysis (UV-vis versus RPES) it is not clear. Another closely related work is Ref.,[17] where the working electrode with CeO_2 NPs was tested as an enzyme-free H_2O_2 sensor in the 0.5 pM – 5.0 mM range. The higher EC signals were generated on the electrode with the lowest Ce^{3+}/Ce^{4+} ratio, in agreement with our results. The absolute Ce^{3+}/Ce^{4+} values cannot be directly compared because of difference in the applied surface characterization techniques. The linearity range 5 – 460 μM for our CeO_2/GC electrode is higher compared with 0.1 pM – 0.1 μM for the CeO_2 NPs based electrode from Ref.,[17] most likely due to insufficient experimental cleanliness in the latter case. The recent work of Li et al.[147] is an example of the application of ceria NPs deposited by magnetron sputtering on TiO_2 used for tissue engineering and regenerative medicine. In general, introduction of an implant into the body initiates an inflammatory cascade due to cell and tissue damage, which is closely related to a local increase of reactive oxygen species formation, such as superoxide and hydrogen peroxide. This work confirmed the importance of the Ce^{3+}/Ce^{4+} ratio for the new bone formation adjacent to the inorganic implant on the base of cerium oxide. Specifically, the manipulation of valence states of ceria NPs appeared to provide an effective modulation of the balance of anti-inflammatory and pro-inflammatory processes and create an anti-inflammatory microenvironment.[147] Summarizing, the morphologically different ceria electrode, i.e., the compact polycrystalline CeO_2 film in the present work is suitable as an electrode for the electrochemical detection of hydrogen peroxide. The CeO_2/GC electrode showed catalytic activity versus H_2O_2, due to available oxygen vacancies and high specific area. Thus, cerium oxide in the form of thin films provides the outstanding properties of ceria NPs, offering a compact polycrystalline electrode material for sensing devices.

Conclusions

Polycrystalline cerium oxide films are proposed for electrochemical detection of hydrogen peroxide. The electrode was characterized by photoelectron spectroscopy and microscopy. The CeO_2/GC electrode surface was formed by compact polycrystalline cerium oxide with the cerium cations in both 4+ and 3+ states. The sensor was tested in PBS solution at 25 °C in the H_2O_2 concentration range from 5 μM to 8 mM. The CeO_2/GC exhibited high sensitivity and linear response in the low H_2O_2 concentration range. The sensor sensitivity was estimated to be 0.7 $\mu A\ \mu M^{-1}\ cm^{-2}$. The detection limit is below 5 μM of H_2O_2. We conclude that H_2O_2 molecules are bound to the oxygen vacancies in the vicinity of Ce^{3+} cations on the surface of the electrode. Thus, ceria absorbs H_2O_2 and coordinates the electrochemical reaction by sharing its electrons. The enzymatic properties of the polycrystalline CeO_2/GC electrode were confirmed. The results bring important knowledge and direct proof of the Ce^{3+} cations role in H_2O_2 sensing by cerium oxide electrodes.

3.2.2. Nanostructured cerium oxide electrode applied for electrochemiluminescent detection of sarcosine

This chapter reveals preliminary results on the polycrystalline cerium oxide thin films (15 nm thick, deposited on the glassy carbon substrate) use as an electrode for electrochemiluminescent (ECL) detection of sarcosine. Preparation and characterization of morphology and structure of the cerium oxide electrode (CeO_2/GC) were done in the same way as in the previous Chapter (for details, see Chapter 2.6.1). Details on the electrochemical measurements are disclosed in the Chapter 2.6.3.

Recently, Valenti et al. has proposed a synergetic ECL supramolecular sensor of sarcosine in urine by using sarcosine as a co-reactant.[48] As it was mentioned in the Chapter 2.4, the luminophore activity of polypyridine ruthenium complexes (in particular $Ru(bpy)_3^{2+}$) in ECL measurements is substantially enhanced in combination with amine molecules (in particular TPrA).[148,149] It was shown that the tertiary amines are the most effective, e.g., they provide the highest ECL intensity and have the lowest limit of detection (LOD).[150,151] Since sarcosine is a secondary amine, it can also be potentially used in the ECL systems interacting with $Ru(bpy)_3^{2+}$ and assisting in light emission. Mechanism of the co-reactant oxidation-reduction reaction for generation of the excited $(Ru(bpy)_3)^{2+*}$ species using amines is briefly described in the Chapter 2.4. Valenti et al. have shown that sarcosine can be used as a co-reactant, but it is 30% less efficient than TPrA.[48] In this chapter of the thesis, we compare CeO_2/GC and bare GC substrates employed as a working electrode for ECL detection of sarcosine in aqueous solution (PBS, pH 7) and show the advantage of the polycrystalline cerium oxide nanostructured film in comparison to the flat glassy carbon substrate.

Results

The structure and morphology of the cerium oxide film were characterized using SEM and AFM microscopies. The surface roughness was estimated to be 1.20-1.30 nm and the grain size between 10-30 nm. The oxidation state and stoichiometry of the cerium oxide on the surface and in the subsurface layers were examined by RPES and XPS techniques by measuring the Ce^{3+} and Ce^{4+} resonances in the VB region and Ce 3d core level spectra. The obtained results showed a minor contribution of the Ce^{3+} cations within the measured thickness range.

In order to estimate the electrocatalytic behavior of the CeO_2/GC electrode, the CV experiments with CeO_2/GC and bare GC working electrodes were conducted in pure 200 mM

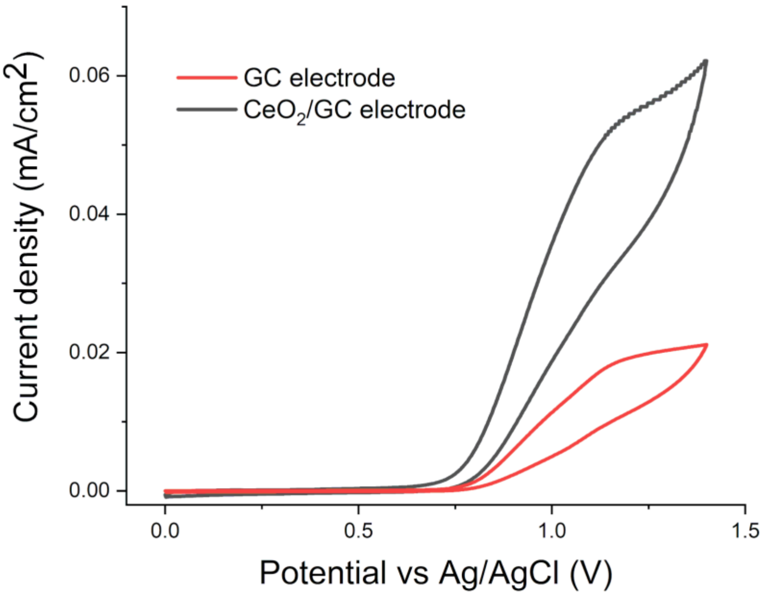

Fig. 3.2.7. *Cyclic voltammogram recorded in TPrA 30 mM and Ru(bpy)*$_3^{2+}$ *10 µM solution on GC (red) and GC/CeO*$_2$ *(blue) electrode, in PH 7 phosphate buffer and scan rate of 100 mV/s, potential range: 0 to 1.4 V.*

PBS and in the presence of mediator - 2 mM potassium ferricyanide (see Chapter 3.2.1). Obtained voltammograms repeated the results shown in the Figure 3.2.2, revealing that CeO$_2$/GC electrode has a higher electroactive surface area compared to bare GC. It is caused by the polycrystalline morphology of the cerium oxide thin film. The results confirm that high catalytic activity of cerium oxide leads to faster electron transfer kinetics. The peak-shape profile of the voltammogram measured in the solution with the mediator is typical for a planar diffusion condition.

In order to estimate efficiency of the CeO$_2$/GC electrode for ECL measurements, it was first tested using Ru(bpy)$_3^{2+}$ as luminophore and TPrA as co-reactant. Since the oxidation of both luminophore and co-reactant happens before 1.4 V,[152] potential range from 0 to 1.4 V was chosen for the measurements. Obtained results of the CV experiment for CeO$_2$/GC are shown in the Figure 3.2.7 and compared with the results obtained for bare GC. We observed that the CeO$_2$/GC electrode produces a higher current density of the Ru(bpy)$_3^{2+}$ oxidation peak compared to the bare GC electrode. Good conductivity of CeO$_2$ gives it the ability to act as a conducting agent between the Ru(bpy)$_3^{2+}$ and the GC electrode surface facilitating the electron-transfer in the ECL reaction. These results confirm compatibility of the CeO$_2$/GC electrode with the Ru(bpy)$_3^{2+}$/TPrA co-reactant ECL system.

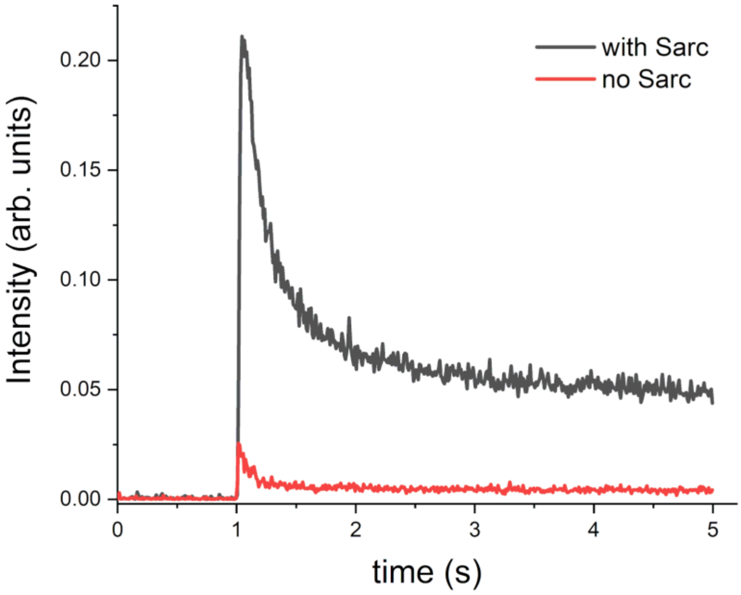

Fig. 3.2.8. *ECL signal obtained in chronoamperometry mode for 10 µM Ru(bpy)*$_3^{2+}$ *complex in 200 mM PBS on the CeO*$_2$*/GC electrode with (gray) and without (red) 5 mM sarcosine as amine co-reactant measured at 1.4 V.*

Sarcosine is a secondary amine (the amino group is directly bonded to two carbon atoms of any hybridization) and can be potentially used as a co-reactant in the ECL experiments, providing sufficient effectivity in the light generation. Sarcosine shows an irreversible oxidation peak at 1 V,[48] and, thus, satisfies the energy requirements for generating the excited state of the chromophore. Its ability to act as a co-reactant for ECL generation has been tested according to the "oxidative-reduction" mechanism in 200 mM PBS using 10µM Ru(bpy)$_3^{2+}$ on CeO$_2$/GC electrode. The preparation step was done at 0 V since no electrochemical processes occur at this potential. The Figure 3.2.8 shows the ECL intensities obtained on CeO$_2$/GC electrode before and after the addition of 5mM sarcosine as co-reactant. Evidently, the addition of sarcosine causes a significant improvement in signal intensity, confirming that sarcosine acts as a good co-reactant for the generation of the ECL.

In order to evaluate the sensing ability of the CeO$_2$/GC electrode to different concentrations of sarcosine using ECL, the experiment was conducted in 10 µM Ru(bpy)$_3^{2+}$ PBS solution with stepwise addition of sarcosine, starting from 50 µM and increasing molecular concentration up to 5 mM. The measurements were performed in the CA mode. The concentration range of sarcosine in the study was chosen in accordance with values of sarcosine that appears in urine medical tests used for early diagnosis of PCa, i.e., 270 µM in healthy people and from 1.34 to

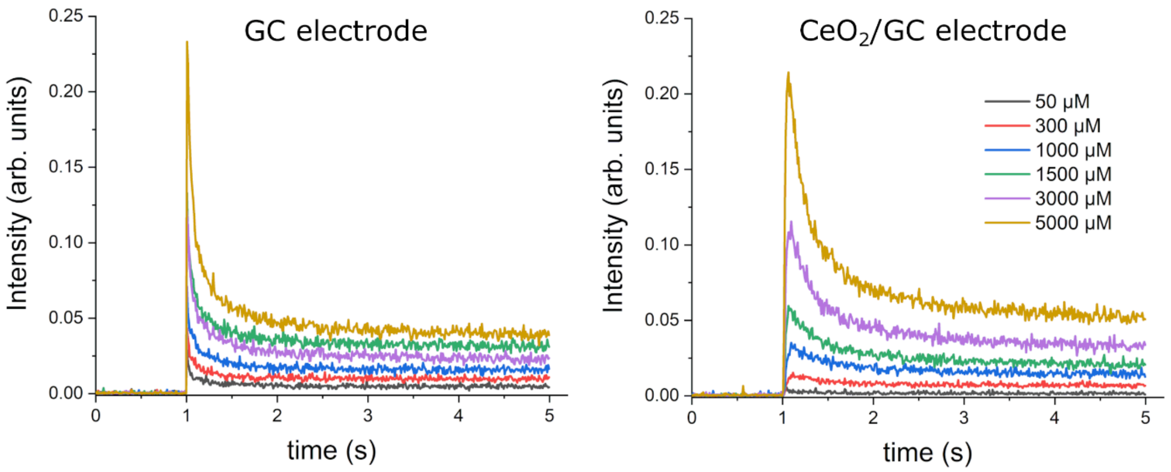

Fig. 3.2.9. *The ECL signal intensity as a function of time recorded on bare GC and CeO2/GC electrodes after addition of different concentrations of sarcosine (from 50 to 5000 µM).*

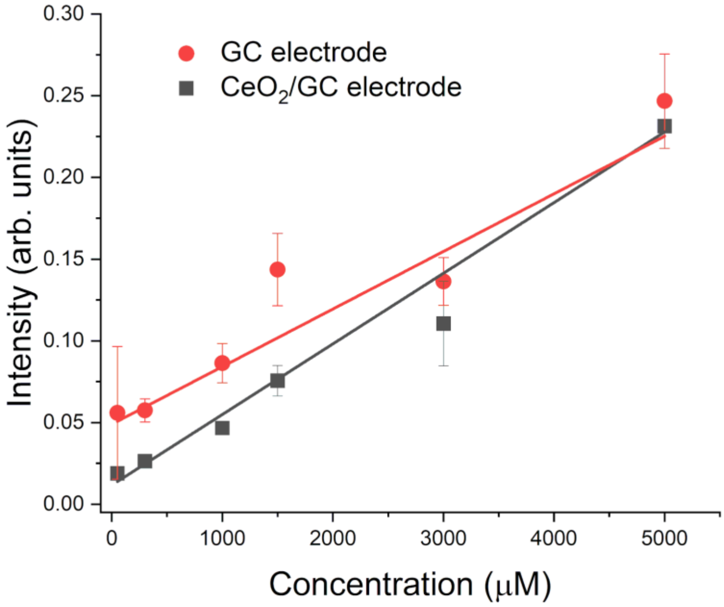

Fig. 3.2.10. *The ECL signal intensity as a function of sarcosine concentration measured in 10 µM Ru(bpy)*$_3^{2+}$ *PBS solution on bare GC and CeO2/GC electrodes.*

1.91 mM in patients with PCa.[153] The same measurements were repeated with the bare GC electrode for comparison and estimation of the CeO_2/GC electrode efficiency. The Figure 3.2.9 shows the ECL intensity profile of different concentrations of sarcosine in the working solution taken on bare GC (left) and CeO_2/GC (right) electrodes. The results reveal a direct dose-response correlation between sarcosine concentration and ECL signal intensity. It is worth to note that on the CeO_2/GC electrode the intensity decay is slower than on the bare GC, pointing to the higher sensitivity of the polycrystalline cerium oxide film in reaction with sarcosine. The ECL peak intensity as a function of sarcosine concentration on CeO_2/GC and bare GC electrodes is shown in the Figure 3.2.10. The error bare is a standard deviation (n=3) and is equal to 0.00065 and 0.0012 for CeO_2/GC and bare GC electrodes, respectively. The LOD parameter was calculated from the obtained calibration lines using the following formula:

$$LOD = {(K \times S_b)}/{m}, \qquad \textbf{Eq. 13}$$

where K equals 2 (confidence level of 92.1%) or 3 (confidence level 98.3%), S_b is the standard deviation of the blank solution, and m is the calibration sensitivity (slope of the calibration curve). Under the optimized experimental conditions, the LOD was found to be 45.9 and 578.7 μM for CeO_2/GC and bare GC electrodes, respectively, lying in the range of detection used in clinical assays. It confirms that GC electrode modified with polycrystalline cerium oxide thin film is more suitable for detection of small concentrations of sarcosine.

Conclusions

Polycrystalline cerium oxide thin films prepared by magnetron sputtering on the glassy carbon substrate (CeO_2/GC) were studied as an electrode for ECL detection of sarcosine, while the sarcosine molecule was used as a co-reactant in oxidative-reduction mechanism with the $Ru(bpy)_3^{2+}$ luminophore. Obtained results revealed that modification of the bare glassy carbon electrode by polycrystalline cerium oxide film increases the electrode's electroactive area and enhances its catalytic properties. The CeO_2/GC electrode was successfully applied for rapid and sensitive detection of different concentrations (50 – 5000 μM) of sarcosine in PBS (PH=7). CeO_2/GC was shown to be a more efficient electrode material for ECL applications compared to the commercial GC electrode. LOD of CeO_2/GC electrode was estimated to be 45.9 μM that makes it suitable for sarcosine detection in the concentration range used in clinical assays for PCs diagnostics.

4. Summary and conclusions

The presented work covers two approaches in research related to the cerium oxide thin films applications in biosensing systems: a fundamental study of molecular adsorption on various cerium oxide surfaces by means of UHV surface science techniques, and more applied study of polycrystalline cerium oxide thin films as a working electrode material in electrochemical sensing of hydrogen peroxide and sarcosine.

The objective of the first part was to increase the knowledge on cerium oxide interaction with biological environment, starting with the simplest case – amino acid molecules. The smallest proteinogenic amino acid glycine and its derivative sarcosine, also known as N-methylglycine, were chosen as model molecules. The information on bonding of glycine or sarcosine to cerium oxide, in general, was not available in the scientific literature up to date. The most important findings are:

1) Glycine was deposited in vacuum on four cerium oxide-based oriented surfaces of different stoichiometry and oxidation states prepared on Cu(111) and W(110) single-crystals. The results revealed that the appearance of the Ce^{3+} cations on the surface does not influence the adsorption chemistry of the molecule compared to the fully oxidized cerium oxide, but the oxygen vacancies play an important role in the glycine bonding to the oxide surface and stability of the molecular adlayer in course of thermal treatment. For all oxides, the glycine molecules adsorb via deprotonated carboxylic group. However, while on CeO_2 and Ce_6WO_{12} glycine lies almost parallel to the surface due to attraction of the amino group by the oxygen anions of the oxide, on the reduced cerium oxides, $CeO_{1.7}$ and Ce_2O_3, the situation is different. In this case, glycine binds to the surface with the carboxylate oxygens incorporated into the vacancies sites and the amino group is directed out of the surface. Interaction between glycine and the cerium tungstate surface is the weakest compared to other systems, with complete desorption of the molecule after 250 °C annealing. The molecular bonding to other oxide films becomes stronger with increasing concentration of the oxygen vacancies on the surface. Decomposition of glycine was observed on the reduced surfaces with formation of adsorbed formate, which further decomposes at higher temperatures, and stable methylamine-like species inducing partial reoxidation of the oxide films.
2) On the polycrystalline cerium oxide thin films, glycine and sarcosine molecules were deposited by evaporation in vacuum and from aqueous solution. Molecules deposited in vacuum adsorb via carboxylate oxygens with neutral amino group. The molecular

adlayer deposited from solution contains the minor contribution of glycine in the zwitterionic form with carboxylate group bound to the oxide surface. The most stable molecular adlayer was obtained for glycine deposited in vacuum. It was explained by formation of additional C-O bond between α-carbon of the molecule and oxygen cations on the surface, caused by flat adsorption geometry of glycine and grain structure of the oxide film. Sarcosine deposited in vacuum on the polycrystalline cerium oxide surface adsorbs in a tilted geometry with amino group directed outward, creating a dense adlayer. Annealing of the system induces decomposition of the molecule with following reduction of the oxide up to 150 °C (caused by water desorption), and reoxidation after treatment in the temperature range 150 - 250 °C (due to refilling of the vacancies by oxygen after decomposition of oxygenated products). It is worth to note that deposition of the molecules from solution causes continuous reduction of the oxide, likely accompanied by water desorption. Such behavior was not observed either for the molecules deposited in vacuum or for the pure water adlayer.

The goal of the second part of the thesis was to investigate if the polycrystalline cerium oxide thin film on glassy carbon substrate could be used as an electrode for electrochemical detection of hydrogen peroxide and electrochemiluminescent detection of sarcosine. Summary of the obtained results is the following:

3) The polycrystalline cerium oxide electrode was proposed and tested for hydrogen peroxide detection in a range from 5 μM to 8 mM in PBS at pH 7 at room temperature. The linear response was observed in a low H_2O_2 concentration diapason. The limit of detection was estimated to be below 5 μM of H_2O_2 with the sensitivity of 0.7 $\mu A\ \mu M^{-1}\ cm^{-2}$. For the first time, the electrochemical study was combined with the RPES and XPS characterization of the CeO_2 electrode. The surface analysis of the working electrode before and after chronoamperometry at low and high concentrations of H_2O_2 demonstrated that under applied potential the hydrogen peroxide molecules adsorb on the oxide surface interacting with the oxygen vacancies on the grain edges near the Ce^{3+} cations. This reaction is followed by O_2 enrichment of the working solution and reoxidation of the cerium oxide. Thus, the catalase enzymatic properties of cerium oxide in the form of polycrystalline film for H_2O_2 oxidation were confirmed. Activity of the electrode terminates when the surface is completely oxidized. However, it was shown that immersion of the electrode into working solution and CV cycling is a potential route to the electrode reactivation. This part of the results was published in

the Journal of Applied Surface Science in 2019. Since then, *the paper has been cited 12 times,* revealing the increasing importance of the topic nowadays.

4) For sarcosine detection using the ECL technique, the sarcosine molecule was used as a co-reactant couple for Ru(bpy)$_3^{2+}$ luminophore with compact polycrystalline cerium oxide film as a working electrode. The electrode was tested in PBS at pH 7 at room temperature in a range of sarcosine concentrations from 50 μM to 5 mM. The electrode showed a linear response in this concentration range. The limit of detection of the electrode was estimated to be 45.9 μM. Thus the CeO$_2$/GC electrode was shown to be suitable for sarcosine detection in the concentration range used in clinical assays for PCs diagnostics.

Bibliography

1 V. Matolín, M. Cabala, I. Matolínová, M. Škoda, M. Václavů, K. C. Prince, T. Skála, T. Mori, H. Yoshikawa, Y. Yamashita, S. Ueda and K. Kobayashi, Pt and Sn Doped Sputtered CeO_2 Electrodes for Fuel Cell Applications, *Fuel Cells*, 2010, **10**, 139–144.

2 V. Esposito and E. Traversa, Design of Electroceramics for Solid Oxides Fuel Cell Applications: Playing with Ceria, *J. Am. Ceram. Soc.*, 2008, **91**, 1037–1051.

3 N. Izu, W. Shin, I. Matsubara and N. Murayama, Development of Resistive Oxygen Sensors Based on Cerium Oxide Thick Film, *J. Electroceramics*, 2004, **13**, 703–706.

4 M. Aguirre, M. Paulis and J. R. Leiza, UV screening clear coats based on encapsulated CeO2 hybrid latexes, *J. Mater. Chem. A*, 2013, **1**, 3155.

5 A. Corma, P. Atienzar, H. García and J.-Y. Chane-Ching, Hierarchically mesostructured doped CeO_2 with potential for solar-cell use, *Nat. Mater.*, 2004, **3**, 394–397.

6 V. Matolín, I. Matolínová, F. Dvořák, V. Johánek, J. Mysliveček, K. C. Prince, T. Skála, O. Stetsovych, N. Tsud, M. Václavů and B. Šmíd, Water interaction with CeO_2(111)/Cu(111) model catalyst surface, *Catal. Today*, 2012, **181**, 124–132.

7 V. Matolín, J. Libra, M. Škoda, N. Tsud, K. C. Prince and T. Skála, Methanol adsorption on a CeO_2(111)/Cu(111) thin film model catalyst, *Surf. Sci.*, 2009, **603**, 1087–1092.

8 M. Wason and J. Zhao, Cerium oxide nanoparticles: potential applications for cancer and other diseases, *Am. J. Transl. Res.*, 2013, **5**, 126–131.

9 I. Celardo, J. Z. Pedersen, E. Traversa and L. Ghibelli, Pharmacological potential of cerium oxide nanoparticles, *Nanoscale*, 2011, **3**, 1411.

10 V. Kalyanaraman, S. V. Naveen, N. Mohana, R. M. Balaje, K. R. Navaneethakrishnan, B. Brabu, S. S. Murugan and T. S. Kumaravel, Biocompatibility studies on cerium oxide nanoparticles-combined study for local effects, systemic toxicity and genotoxicity: Via implantation route, *Toxicol. Res. (Camb).*, 2019, **8**, 25–37.

11 S. S. Lee, W. Song, M. Cho, H. L. Puppala, P. Nguyen, H. Zhu, L. Segatori and V. L. Colvin, Antioxidant properties of cerium oxide nanocrystals as a function of nanocrystal diameter and surface coating, *ACS Nano*, 2013, **7**, 9693–9703.

12 N. Ould-Moussa, M. Safi, M.-A. Guedeau-Boudeville, D. Montero, H. Conjeaud and J.-F. Berret, In vitro toxicity of nanoceria: effect of coating and stability in biofluids., *Nanotoxicology*, 2014, **8**, 799–811.

13 S. Saha, S. K. Arya, S. P. Singh, K. Sreenivas, B. D. Malhotra and V. Gupta, Nanoporous cerium oxide thin film for glucose biosensor, *Biosens. Bioelectron.*, 2009, **24**, 2040–

2045.

14 M. Moumene, A. Tabet-Aoul, M. Gougis, D. Rochefort and M. Mohamedi, Laser pulse deposited nanosized ceria for direct electron transfer of glucose oxidase, *Int. J. Electrochem. Sci.*, 2014, **9**, 176–184.

15 A. A. Ansari, P. R. Solanki and B. D. Malhotra, Sol-gel derived nanostructured cerium oxide film for glucose sensor, *Appl. Phys. Lett.*, 2008, **92**, 263901.

16 Y. Kosto, A. Zanut, S. Franchi, Y. Yakovlev, I. Khalakhan, V. Matolín, K. C. Prince, G. Valenti, F. Paolucci and N. Tsud, Electrochemical activity of the polycrystalline cerium oxide films for hydrogen peroxide detection, *Appl. Surf. Sci.*, 2019, **488**, 351–359.

17 C. J. Neal, A. Gupta, S. Barkam, S. Saraf, S. Das, H. J. Cho and S. Seal, Picomolar Detection of Hydrogen Peroxide using Enzyme-free Inorganic Nanoparticle-based Sensor, *Sci. Rep.*, 2017, **7**, 1324.

18 A. A. Ansari, P. R. Solanki and B. D. Malhotra, Hydrogen peroxide sensor based on horseradish peroxidase immobilized nanostructured cerium oxide film, *J. Biotechnol.*, 2009, **142**, 179–184.

19 A. A. Ansari, A. Kaushik, P. R. Solanki and B. D. Malhotra, Sol-gel derived nanoporous cerium oxide film for application to cholesterol biosensor, *Electrochem. commun.*, 2008, **10**, 1246–1249.

20 S. Panky, K. Thandavan, D. Sivalingam, S. Sethuraman, U. M. Krishnan, B. G. Jeyaprakash and J. B. B. Rayappan, Lipase immobilized on nanostructured cerium oxide thin film coated on transparent conducting oxide electrode for butyrin sensing, *Mater. Chem. Phys.*, 2013, **137**, 892–897.

21 K. Feng, Y. Yang, Z. Wang, J. Jiang, G. Shen and R. Yu, A nano-porous CeO_2/Chitosan composite film as the immobilization matrix for colorectal cancer DNA sequence-selective electrochemical biosensor, 2006, **70**, 561–565.

22 Y.-B. Hahn, R. Ahmad and N. Tripathy, Chemical and biological sensors based on metal oxide nanostructures, *Chem. Commun.*, 2012, **48**, 10369.

23 C. Xu and X. Qu, Cerium oxide nanoparticle: a remarkably versatile rare earth nanomaterial for biological applications, *NPG Asia Mater.*, 2014, **6**, e90.

24 D. Patil, N. Q. Dung, H. Jung, S. Y. Ahn, D. M. Jang and D. Kim, Enzymatic glucose biosensor based on CeO_2 nanorods synthesized by non-isothermal precipitation., *Biosens. Bioelectron.*, 2012, **31**, 176–81.

25 P. R. Solanki, A. Kaushik, V. V. Agrawal and B. D. Malhotra, Nanostructured metal oxide-based biosensors, *NPG Asia Mater.*, 2011, **3**, 17–24.

26 Y. Lin, J. Ren and X. Qu, Catalytically active nanomaterials: a promising candidate for artificial enzymes, *Acc Chem Res*, 2014, **47**, 1097–1105.

27 X. Wang, Y. Hu and H. Wei, Nanozymes in bionanotechnology: from sensing to therapeutics and beyond, *Inorg. Chem. Front.*, 2016, **3**, 41–60.

28 F. Qu, H. Sun, S. Zhang, J. You and M. Yang, Electrochemical sensing platform based on palladium modified ceria nanoparticles, *Electrochim. Acta*, 2012, **61**, 173–178.

29 M. Cai, L. Zhu, Y. Ding, J. Wang, J. Li and X. Du, Determination of sulfamethoxazole in foods based on CeO_2/chitosan nanocomposite-modified electrodes, *Mater. Sci. Eng. C*, 2012, **32**, 2623–2627.

30 P. R. Solanki, C. Dhand, A. Kaushik, A. A. Ansari, K. N. Sood and B. D. Malhotra, Nanostructured cerium oxide film for triglyceride sensor, *Sensors Actuators, B Chem.*, 2009, **141**, 551–556.

31 A. Kaushik, P. R. Solanki, A. A. Ansari, S. Ahmad and B. D. Malhotra, A nanostructured cerium oxide film-based immunosensor for mycotoxin detection, *Nanotechnology*, 2009, **20**, 055105.

32 Global Hydrogen Peroxide Industry, https://www.reportlinker.com/p090603/World-Hydrogen-Peroxide-Market.html?utm_source=GNW.

33 M. Valko, D. Leibfritz, J. Moncol, M. T. D. Cronin, M. Mazur and J. Telser, Free radicals and antioxidants in normal physiological functions and human disease, *Int. J. Biochem. Cell Biol.*, 2007, **39**, 44–84.

34 M. Malferrari, A. Ghelli, F. Roggiani, G. Valenti, F. Paolucci, M. Rugolo and S. Rapino, Reactive Oxygen Species Produced by Mutated Mitochondrial Respiratory Chains of Entire Cells Monitored Using Modified Microelectrodes, *ChemElectroChem*, 2019, **6**, 627–633.

35 P. Frontera, A. Malara, S. Stelitano, S. G. Leonardi, A. Bonavita, E. Fazio, P. Antonucci, G. Neri, F. Neri and S. Santangelo, Characterisation and H_2O_2 sensing properties of TiO_2-CNTs/Pt electro-catalysts, *Mater. Chem. Phys.*, 2016, **170**, 129–137.

36 A. Mehta, S. Patil, H. Bang, H. J. Cho and S. Seal, A novel multivalent nanomaterial based hydrogen peroxide sensor, *Sensors Actuators, A Phys.*, 2007, **134**, 146–151.

37 W. Zhang, G. Xie, S. Li, L. Lu and B. Liu, Au/CeO2-chitosan composite film for hydrogen peroxide sensing, *Appl. Surf. Sci.*, 2012, **258**, 8222–8227.

38 A. K. Yagati, T. Lee, J. Min and J. W. Choi, An enzymatic biosensor for hydrogen peroxide based on CeO_2 nanostructure electrodeposited on ITO surface, *Biosens. Bioelectron.*, 2013, **47**, 385–390.

39 M. V. Bracamonte, M. Melchionna, A. Giuliani, L. Nasi, C. Tavagnacco, M. Prato and P. Fornasiero, H_2O_2 sensing enhancement by mutual integration of single walled carbon nanohorns with metal oxide catalysts: The CeO2 case, *Sensors Actuators, B Chem.*, 2017, **239**, 923–932.

40 S. K. Ujjain, A. Das, G. Srivastava, P. Ahuja, M. Roy, A. Arya, K. Bhargava, N. Sethy, S. K. Singh, R. K. Sharma and M. Das, Nanoceria based electrochemical sensor for hydrogen peroxide detection, *Biointerphases*, 2014, **9**, 031011.

41 L. Klotz, Prostate cancer overdiagnosis and overtreatment, *Curr. Opin. Endocrinol. Diabetes Obes.*, 2013, **20**, 204–209.

42 A. Sreekumar, L. M. Poisson, T. M. Rajendiran, A. P. Khan, Q. Cao, J. Yu, B. Laxman, R. Mehra, R. J. Lonigro, Y. Li, M. K. Nyati, A. Ahsan, S. Kalyana-Sundaram, B. Han, X. Cao, J. Byun, G. S. Omenn, D. Ghosh, S. Pennathur, D. C. Alexander, A. Berger, J. R. Shuster, J. T. Wei, S. Varambally, C. Beecher and A. M. Chinnaiyan, Metabolomic profiles delineate potential role for sarcosine in prostate cancer progression, *Nature*, 2009, **457**, 910–914.

43 J. Couzin, BIOMARKERS: Metabolite in Urine May Point To High-Risk Prostate Cancer, *Science (80-.).*, 2009, **323**, 865a-865a.

44 Y. Jiang, X. Cheng, C. Wang and Y. Ma, Quantitative Determination of Sarcosine and Related Compounds in Urinary Samples by Liquid Chromatography with Tandem Mass Spectrometry, *Anal. Chem.*, 2010, **82**, 9022–9027.

45 T. S. C. R. Rebelo, C. M. Pereira, M. G. F. Sales, J. P. Noronha, J. Costa-Rodrigues, F. Silva and M. H. Fernandes, Sarcosine oxidase composite screen-printed electrode for sarcosine determination in biological samples, *Anal. Chim. Acta*, 2014, **850**, 26–32.

46 J. Lan, W. Xu, Q. Wan, X. Zhang, J. Lin, J. Chen and J. Chen, Colorimetric determination of sarcosine in urine samples of prostatic carcinoma by mimic enzyme palladium nanoparticles, *Anal. Chim. Acta*, 2014, **825**, 63–68.

47 E. Biavardi, C. Tudisco, F. Maffei, A. Motta, C. Massera, G. G. Condorelli and E. Dalcanale, Exclusive recognition of sarcosine in water and urine by a cavitand-functionalized silicon surface, *Proc. Natl. Acad. Sci.*, 2012, **109**, 2263–2268.

48 G. Valenti, E. Rampazzo, E. Biavardi, E. Villani, G. Fracasso, M. Marcaccio, F. Bertani, D. Ramarli, E. Dalcanale, F. Paolucci and L. Prodi, An electrochemiluminescence-supramolecular approach to sarcosine detection for early diagnosis of prostate cancer, *Faraday Discuss.*, 2015, **185**, 299–309.

49 F. Ersan, E. Aktürk and S. Ciraci, Glycine self-assembled on graphene enhances the

solar absorbance performance, *Carbon N. Y.*, 2019, **143**, 329–334.

50 F. Ersan, O. Üzengi Aktürk, E. Aktürk and S. Ciraci, Metal-Insulator Transition and Heterostructure Formation by Glycines Self-Assembled on Defect-Patterned Graphene, *J. Phys. Chem. C*, 2018, **122**, 14598–14605.

51 N. Ly, C. Seo and S.-W. Joo, Detection of Copper(II) Ions Using Glycine on Hydrazine-Adsorbed Gold Nanoparticles via Raman Spectroscopy, *Sensors*, 2016, **16**, 1785.

52 L. Chen, Y. He, Q. Yang, R. R. Yang, L. Zhang, Y. Fan and Z. He, A glycine derivative as corrosion inhibitor for carbon steel in 3.5 wt% NaCl solution: The combined experimental and theoretical calculation, *Int. J. Electrochem. Sci.*, 2018, **13**, 4640–4660.

53 A. Sreekumar, L. M. Poisson, T. M. Rajendiran, A. P. Khan, Q. Cao, J. Yu, B. Laxman, R. Mehra, R. J. Lonigro, Y. Li, M. K. Nyati, A. Ahsan, S. Kalyana-Sundaram, B. Han, X. Cao, J. Byun, G. S. Omenn, D. Ghosh, S. Pennathur, D. C. Alexander, A. Berger, J. R. Shuster, J. T. Wei, S. Varambally, C. Beecher and A. M. Chinnaiyan, Metabolomic profiles delineate potential role for sarcosine in prostate cancer progression, *Nature*, 2009, **457**, 910–914.

54 N. Jornet-Martínez, C. J. Henderson, P. Campíns-Falcó, R. Daly and E. A. H. Hall, Towards sarcosine determination in urine for prostatic carcinoma detection, *Sensors Actuators, B Chem.*, 2019, **287**, 380–389.

55 X. Zhao, H. Yan, R. G. Zhao and W. S. Yang, Self-Assembled Structures of Glycine on Cu(111), *Langmuir*, 2003, **19**, 809–813.

56 V. Efstathiou and D. P. Woodruff, Characterisation of the interaction of glycine with Cu(100) and Cu(111), *Surf. Sci.*, 2003, **531**, 304–318.

57 S. Barlow, K. Kitching, S. Haq and N. Richardson, A study of glycine adsorption on a Cu{110} surface using reflection absorption infrared spectroscopy, *Surf. Sci.*, 1998, **401**, 322–335.

58 P. Löfgren, a. Krozer, J. Lausmaa and B. Kasemo, Glycine on Pt(111): a TDS and XPS study, *Surf. Sci.*, 1997, **370**, 277–292.

59 G. Feng, L. Zhenjun, W. Yilin, L. Burkholder and W. T. Tysoe, Chemistry of glycine on Pd(111): Temperature-programmed desorption and X-ray photoelectron spectroscopic study, *J. Phys. Chem. C*, 2007, **111**, 9981–9991.

60 T. J. Lerotholi, E. A. Kröger, M. J. Knight, W. Unterberger, K. Hogan, D. C. Jackson, C. L. A. Lamont and D. P. Woodruff, Adsorption structure of glycine on TiO_2(110): A photoelectron diffraction determination, *Surf. Sci.*, 2009, **603**, 2305–2311.

61 J. N. Wilson, R. M. Dowler and H. Idriss, Adsorption and reaction of glycine on the

rutile TiO_2(011) single crystal surface, *Surf. Sci.*, 2011, **605**, 206–213.

62 R. Tonner, Adsorption of Proline and Glycine on the TiO2(110) Surface: A Density Functional Theory Study, *ChemPhysChem*, 2010, **11**, 1053–1061.

63 J. Lausmaa, P. Lofgren and B. Kasemo, Adsorption and coadsorption of water and glycine on TiO2, *J. Biomed. Mater. Res.*, 1999, **44**, 227–242.

64 G. Tzvetkov, G. Koller, Y. Zubavichus, O. Fuchs, M. B. Casu, C. Heske, E. Umbach, M. Grunze, M. G. Ramsey and F. P. Netzer, Bonding and structure of glycine on ordered Al_2O_3 film surfaces, *Langmuir*, 2004, **20**, 10551–10559.

65 P. A. Garrain, D. Costa and P. Marcus, Biomaterial-biomolecule interaction: DFT-D study of glycine adsorption on Cr_2O_3, *J. Phys. Chem. C*, 2011, **115**, 719–727.

66 D. Costa, P. A. Garrain, B. Diawara and P. Marcus, Biomolecule-biomaterial interaction: A DFT-D study of glycine adsorption and self-assembly on hydroxylated Cr_2O_3 surfaces, *Langmuir*, 2011, **27**, 2747–2760.

67 N. Tsud, R. G. Acres, M. Iakhnenko, D. Mazur, K. C. Prince and V. Matolín, Bonding of Histidine to Cerium Oxide, *J. Phys. Chem. B*, 2013, **117**, 9182–9193.

68 N. Tsud, S. Bercha, R. G. Acres, M. Vorokhta, I. Khalakhan, K. C. Prince and V. Matolín, Functionalization of nanostructured cerium oxide films with histidine, *Phys. Chem. Chem. Phys.*, 2015, **17**, 2770–2777.

69 S. Bercha, G. Mali, I. Khalakhan, T. Skála, K. C. Prince, V. Matolín and N. Tsud, Histidine adsorption on nanostructured cerium oxide, *J. Electron Spectros. Relat. Phenomena*, 2016, **212**, 28–33.

70 A. Neitzel, Y. Lykhach, V. Johánek, N. Tsud, T. Skála, K. C. Prince, V. Matolín and J. Libuda, Decomposition of Acetic Acid on Model Pt/CeO_2 Catalysts: The Effect of Surface Crowding, *J. Phys. Chem. C*, 2015, **119**, 13721–13734.

71 D. Briggs and M. P. Seah, *Practical surface analysis, Auger and X-ray photoelectron spectroscopy.* 657 pp., John Wiley & Sons, Ltd, New York, 1990, vol. I.

72 S. Hüfner, *Photoelectron Spectroscopy*, Springer Berlin Heidelberg, Berlin, Heidelberg, 2003.

73 G. A. Somorjai, *Chemistry in two dimensions: surfaces*, Cornell University Press, 1981.

74 R. Z. Bachrach, *Synchrotron Radiation Research*, Springer US, Boston, MA, 1992.

75 O. Tjernberg, S. Söderholm, U. Karlsson, G. Chiaia, M. Qvarford, H. Nylén and I. Lindau, Resonant photoelectron spectroscopy on NiO, *Phys. Rev. B - Condens. Matter Mater. Phys.*, 1996, **53**, 10372–10376.

76 H. Magnan, P. Le Fèvre, D. Chandesris, P. Krüger, S. Bourgeois, B. Domenichini, A.

Verdini, L. Floreano and A. Morgante, Resonant photoelectron and photoelectron diffraction across the FeL$_3$ edge of Fe$_3$O$_4$, *Phys. Rev. B - Condens. Matter Mater. Phys.*, 2010, **81**, 1–6.

77 Y. Lykhach, T. Staudt, M. Vorokhta, T. Skála, V. Johánek, K. C. Prince, V. Matolín and J. Libuda, Hydrogen spillover monitored by resonant photoemission spectroscopy, *J. Catal.*, 2012, **285**, 6–9.

78 D. R. Mullins, S. H. Overbury and D. R. Huntley, Electron spectroscopy of single crystal and polycrystalline cerium oxide surface, *Surf. Sci.*, 1998, **409**, 307–319.

79 A. Pfau and K. D. Schierbaum, The electronic structure of stoichiometric and reduced CeO$_2$ surfaces: an XPS, UPS and HREELS study, *Surf. Sci.*, 1994, **321**, 71–80.

80 E. Wuilloud, B. Delley, W. D. Schneider and Y. Baer, Spectroscopic evidence for localized and extended f-symmetry states in CeO$_2$, *Phys. Rev. Lett.*, 1984, **53**, 202–205.

81 P. S. Bagus, E. S. Ilton and C. J. Nelin, The interpretation of XPS spectra: Insights into materials properties, *Surf. Sci. Rep.*, 2013, **68**, 273–304.

82 S. Fabris, G. Vicario, G. Balducci, S. De Gironcoli and S. Baroni, Electronic and atomistic structures of clean and reduced ceria surfaces, *J. Phys. Chem. B*, 2005, **109**, 22860–22867.

83 Z. Yang, T. K. Woo, M. Baudin and K. Hermansson, Atomic and electronic structure of unreduced and reduced CeO$_2$ surfaces: A first-principles study, *J. Chem. Phys.*, 2004, **120**, 7741–7749.

84 T. Skála, F. Šutara, K. C. Prince and V. Matolín, Cerium oxide stoichiometry alteration via Sn deposition: Influence of temperature, *J. Electron Spectros. Relat. Phenomena*, 2009, **169**, 20–25.

85 H. Shinotsuka, S. Tanuma, C. J. Powell and D. R. Penn, Calculations of electron inelastic mean free paths. X. Data for 41 elemental solids over the 50 eV to 200 keV range with the relativistic full Penn algorithm, *Surf. Interface Anal.*, 2015, **47**, 871–888.

86 M. P. Seah and W. A. Dench, Quantitative electron spectroscopy of surfaces: A standard data base for electron inelastic mean free paths in solids, *Surf. Interface Anal.*, 1979, **1**, 2–11.

87 D. Briggs and M. P. Seah, *Practical Surface Analysis, Auger and X-ray Photoelectron Spectroscopy*, Wiley, 2nd edn., 1996.

88 Y. K. Gao, F. Traeger, C. Wöll and H. Idriss, Glycine adsorption and photo-reaction over ZnO(000$\bar{1}$) single crystal, *Surf. Sci.*, 2014, **624**, 112–117.

89 C. B. Ching, K. Hidajat and M. S. Uddin, Evaluation of Equilibrium and Kinetic

Parameters of Smaller Molecular Size Amino Acids on KX Zeolite Crystals via Liquid Chromatographic Techniques, *Sep. Sci. Technol.*, 1989, **24**, 581–597.

90 T. Staudt, Y. Lykhach, L. Hammer, M. A. Schneider, V. Matolín and J. Libuda, A route to continuous ultra-thin cerium oxide films on Cu(111), *Surf. Sci.*, 2009, **603**, 3382–3388.

91 H. Winick and S. Doniach, in *Synchrotron Radiation Research*, Springer US, Boston, MA, 1980, pp. 1–10.

92 J. Stöhr, *NEXAFS Spectroscopy*, Springer Berlin Heidelberg, Berlin, Heidelberg, 1992, vol. 25.

93 K. Weiss, P. S. Bagus and C. Wöll, Rydberg transitions in X-ray absorption spectroscopy of alkanes: The importance of matrix effects, *J. Chem. Phys.*, 1999, **111**, 6834–6845.

94 S. G. Urquhart and R. Gillies, Rydberg-valence mixing in the carbon Is near-edge X-ray absorption fine structure spectra of gaseous alkanes, *J. Phys. Chem. A*, 2005, **109**, 2151–2159.

95 J. Stöhr and D. A. Outka, Determination of molecular orientations on surfaces from the angular dependence of near-edge x-ray-absorption fine-structure spectra, *Phys. Rev. B*, 1987, **36**, 7891–7905.

96 J. Koryta, J. Dvorak and L. Kavan, *Principles of Electrochemistry*, Wiley, 1993.

97 Cynthia G. Zoski, *Handbook of Electrochemistry*, Elsevier, 2007.

98 R. Parsons, Electrical Double Layer: Recent Experimental and Theoretical Developments, *Chem. Rev.*, 1990, **90**, 813–826.

99 G. Inzelt, in *Encyclopedia of Applied Electrochemistry*, Springer New York, New York, NY, 2014, pp. 207–214.

100 M. M. Richter, Electrochemiluminescence (ECL), *Chem. Rev.*, 2004, **104**, 3003–3036.

101 M. A. VanHove, W. H. Weinberg and C.-M. Chan, *Low-energy electron diffraction: experiment, theory and surface structure determination.*, Springer s. New York: Springer-Verlag, 1986.

102 V. Mironov, *Fundamentals of scanning probe microscopy*, 2004.

103 S. Amelinckx, D. van Dyck, J. van Landuyt and G. van Tendeloo, in *Handbook of Microscopy*, Wiley-VCH Verlag GmbH, Weinheim, Germany, 2008, pp. 539–561.

104 F. Šutara, M. Cabala, L. Sedláček, T. Skála, M. Škoda, V. Matolín, K. C. Prince and V. Cháb, Epitaxial growth of continuous $CeO_2(111)$ ultra-thin films on Cu(111), *Thin Solid Films*, 2008, **516**, 6120–6124.

105 T. Duchoň, F. Dvořák, M. Aulická, V. Stetsovych, M. Vorokhta, D. Mazur, K. Veltruská, T. Skála, J. Mysliveček, I. Matolínová and V. Matolín, Ordered Phases of Reduced Ceria As Epitaxial Films on Cu(111), *J. Phys. Chem. C*, 2014, **118**, 357–365.

106 V. Stetsovych, F. Pagliuca, F. Dvořák, T. Duchoň, M. Vorokhta, M. Aulická, J. Lachnitt, S. Schernich, I. Matolínová, K. Veltruská, T. Skála, D. Mazur, J. Mysliveček, J. Libuda and V. Matolín, Epitaxial Cubic Ce_2O_3 Films via Ce–CeO_2 Interfacial Reaction, *J. Phys. Chem. Lett.*, 2013, **4**, 866–871.

107 O. Plekan, V. Feyer, R. Richter, M. Coreno, M. De Simone, K. C. Prince and V. Carravetta, Investigation of the amino acids glycine, proline, and methionine by photoemission spectroscopy, *J. Phys. Chem. A*, 2007, **111**, 10998–11005.

108 S. Bercha, K. Beranová, R. G. Acres, M. Vorokhta, M. Dubau, I. Matolínová, T. Skála, K. C. Prince, V. Matolín and N. Tsud, Thermally Controlled Bonding of Adenine to Cerium Oxide: Effect of Substrate Stoichiometry, Morphology, Composition, and Molecular Deposition Technique, *J. Phys. Chem. C*, 2017, **121**, 25118–25131.

109 Y. Lykhach, M. Happel, V. Johánek, T. Skála, F. Kollhoff, N. Tsud, F. Dvořák, K. C. Prince, V. Matolín and J. Libuda, Adsorption and decomposition of formic acid on model ceria and Pt/Ceria catalysts, *J. Phys. Chem. C*, 2013, **117**, 12483–12494.

110 A. R. Slaughter and M. S. Banna, Core-photoelectron binding energies of gaseous glycine: Correlation with its proton affinity and gas-phase acidity, *J. Phys. Chem.*, 1988, **92**, 2165–2167.

111 A. Shavorskiy, T. Eralp, K. Schulte, H. Bluhm and G. Held, Surface chemistry of glycine on Pt{111} in different aqueous environments, *Surf. Sci.*, 2013, **607**, 10–19.

112 J. Hasselström, O. Karis, M. Weinelt, N. Wassdahl, A. Nilsson, M. Nyberg, L. G. M. Pettersson, M. G. Samant and J. Stöhr, The adsorption structure of glycine adsorbed on Cu(110); comparison with formate and acetate, *Surf. Sci.*, 1998, **407**, 221–236.

113 Y. Zubavichus, M. Zharnikov, A. Schaporenko and M. Grunze, NEXAFS study of glycine and glycine-based oligopeptides, *J. Electron Spectros. Relat. Phenomena*, 2004, **134**, 25–33.

114 Y. Zubavichus, A. Shaporenko, M. Grunze and M. Zharnikov, Innershell absorption spectroscopy of amino acids at all relevant absorption edges, *J. Phys. Chem. A*, 2005, **109**, 6998–7000.

115 Y. Zubavichus, A. Shaporenko, M. Grunze and M. Zharnikov, Solid-State Near-Edge X-ray Absorption Fine Structure Spectra of Glycine in Various Charge States, *J. Phys. Chem. B*, 2006, **110**, 3420–3427.

116 M. L. Gordon, G. Cooper, C. Morin, T. Araki, C. C. Turci, K. Kaznatcheev and A. P. Hitchcock, Inner-shell excitation spectroscopy of the peptide bond: Comparison of the C 1s, N 1s, and O 1s spectra of glycine, glycyl-glycine, and glycyl-glycyl-glycine, *J. Phys. Chem. A*, 2003, **107**, 6144–6159.

117 P. A. Stevens, R. J. Madix and J. Stöhr, NEXAFS study of HCOO/Ag(110): Evidence for dynamic bending, *Surf. Sci.*, 1990, **230**, 1–12.

118 E. Otero and S. G. Urquhart, Nitrogen 1s near-edge X-ray absorption fine structure spectroscopy of amino acids: Resolving zwitterionic effects, *J. Phys. Chem. A*, 2006, **110**, 12121–12128.

119 F. Dvořák, O. Stetsovych, M. Steger, E. Cherradi, I. Matolínová, N. Tsud, M. Škoda, T. Skála, J. Mysliveček and V. Matolín, Adjusting Morphology and Surface Reduction of CeO_2(111) Thin Films on Cu(111), *J. Phys. Chem. C*, 2011, **115**, 7496–7503.

120 T. Skála, N. Tsud, M. Á. N. Orti, T. O. Menteş, A. Locatelli, K. C. Prince and V. Matolín, In situ growth of epitaxial cerium tungstate (100) thin films, *Phys. Chem. Chem. Phys.*, 2011, **13**, 7083.

121 Y. Lykhach, S. M. Kozlov, T. Skála, A. Tovt, V. Stetsovych, N. Tsud, F. Dvořák, V. Johánek, A. Neitzel, J. Mysliveček, S. Fabris, V. Matolín, K. M. Neyman and J. Libuda, Counting electrons on supported nanoparticles, *Nat. Mater.*, 2016, **15**, 284–288.

122 R. Cook, E. A. Crathorne, A. J. Monhemius and D. L. Perry, An XPS study of the adsorption of gold (I) cyanide by carbons, *Hydrometallurgy*, 1989, **22**, 171–182.

123 M. Ekimova, M. Kubin, M. Ochmann, J. Ludwig, N. Huse, P. Wernet, M. Odelius and E. T. J. Nibbering, Soft X-ray Spectroscopy of the Amine Group: Hydrogen Bond Motifs in Alkylamine/Alkylammonium Acid-Base Pairs, *J. Phys. Chem. B*, 2018, **122**, 7737–7746.

124 G. R. Wight and C. E. Brion, K-shell excitation of CH_4, NH_3, H_2O, CH_3OH, CH_3OCH_3 and CH_3NH_2 by 2.5 keV electron impact, *J. Electron Spectros. Relat. Phenomena*, 1974, **4**, 25–42.

125 D. A. Outka, J. Stöhr, R. J. Madix, H. H. Rotermund, B. Hermsmeier and J. Solomon, NEXAFS studies of complex alcohols and carboxylic acids on the Si(111)(7×7) surface, *Surf. Sci.*, 1987, **185**, 53–74.

126 K. H. Ernst and K. Christmann, The interaction of glycine with a platinum (111) surface, *Surf. Sci.*, 1989, **224**, 277–310.

127 F. R. Tortonda, J. L. Pascual-Ahuir, E. Silla and I. Tuñón, Why is glycine a zwitterion in aqueous solution? A theoretical study of solvent stabilising factors, *Chem. Phys. Lett.*,

1996, **260**, 21–26.

128 S. Xu, J. M. Nilles and K. H. Bowen, Zwitterion formation in hydrated amino acid, dipole bound anions: How many water molecules are required?, *J. Chem. Phys.*, 2003, **119**, 10696–10701.

129 Y. Lykhach, S. M. Kozlov, T. Skala, A. Tovt, V. Stetsovych, N. Tsud, F. Dvorak, V. Johanek, A. Neitzel, J. Myslivecek, S. Fabris, V. Matolin, K. M. Neyman and J. Libuda, Counting electrons on supported nanoparticles, *Nat Mater*, 2016, **15**, 284–288.

130 M. Kettner, K. Ševčíková, P. Homola, V. Matolín and V. Nehasil, Influence of the Ce–F interaction on cerium photoelectron spectra in CeOXFY layers, *Chem. Phys. Lett.*, 2015, **639**, 126–130.

131 Bagotsky V. S., *Fundamentals of Electrochemistry. 2nd Edn. Wiley,* 2006.

132 Y. Li, C. Sella, F. Lemaître, M. Guille Collignon, L. Thouin and C. Amatore, Highly Sensitive Platinum-Black Coated Platinum Electrodes for Electrochemical Detection of Hydrogen Peroxide and Nitrite in Microchannel, *Electroanalysis*, 2013, **25**, 895–902.

133 R. Singh and S. Singh, Role of phosphate on stability and catalase mimetic activity of cerium oxide nanoparticles., *Colloids Surf. B. Biointerfaces*, 2015, **132**, 78–84.

134 A. Juzgado, A. Soldà, A. Ostric, A. Criado, G. Valenti, S. Rapino, G. Conti, G. Fracasso, F. Paolucci and M. Prato, Highly sensitive electrochemiluminescence detection of a prostate cancer biomarker, *J. Mater. Chem. B*, 2017, **5**, 6681–6687.

135 X. Jiao, H. Song, H. Zhao, W. Bai, L. Zhang and Y. Lv, Well-redispersed ceria nanoparticles: Promising peroxidase mimetics for H_2O_2 and glucose detection, *Anal. Methods*, 2012, **4**, 3261.

136 H. Zhao, Y. Dong, P. Jiang, G. Wang and J. Zhang, Highly dispersed CeO_2 on TiO_2 nanotube: A synergistic nanocomposite with superior peroxidase-like activity, *ACS Appl. Mater. Interfaces*, 2015, **7**, 6451–6461.

137 Q. Liu, Y. Yang, X. Lv, Y. Ding, Y. Zhang, J. Jing and C. Xu, One-step synthesis of uniform nanoparticles of porphyrin functionalized ceria with promising peroxidase mimetics for H_2O_2 and glucose colorimetric detection, *Sensors Actuators B Chem.*, 2017, **240**, 726–734.

138 X. Wang, W. Cao, L. Qin, T. Lin, W. Chen, S. Lin, J. Yao, X. Zhao, M. Zhou, C. Hang and H. Wei, Boosting the peroxidase-like activity of nanostructured nickel by inducing its 3+ oxidation state in $LaNiO_3$ perovskite and its application for biomedical assays, *Theranostics*, 2017, **7**, 2277–2286.

139 W. Zhang, G. Xie, S. Li, L. Lu and B. Liu, Au/CeO_2–chitosan composite film for

hydrogen peroxide sensing, *Appl. Surf. Sci.*, 2012, **258**, 8222–8227.

140 L. Gao, J. Zhuang, L. Nie, J. Zhang, Y. Zhang, N. Gu, T. Wang, J. Feng, D. Yang, S. Perrett and X. Yan, Intrinsic peroxidase-like activity of ferromagnetic nanoparticles., *Nat. Nanotechnol.*, 2007, **2**, 577–583.

141 F. Qiao, J. Wang, S. Ai and L. Li, As a new peroxidase mimetics: The synthesis of selenium doped graphitic carbon nitride nanosheets and applications on colorimetric detection of H_2O_2 and xanthine, *Sensors Actuators B Chem.*, 2015, **216**, 418–427.

142 T. Pirmohamed, J. M. Dowding, S. Singh, B. Wasserman, E. Heckert, A. S. Karakoti, J. E. S. King, S. Seal and W. T. Self, Nanoceria exhibit redox state-dependent catalase mimetic activity, *Chem. Commun.*, 2010, **46**, 2736–2738.

143 Z. N. De Pourbaix M, *Atlas of Electrochemical Equilibria in Aqueous Solutions*, National Association of Corrosion Engineers, Houston, 1974.

144 K. Reed, A. Cormack, A. Kulkarni, M. Mayton, D. Sayle, F. Klaessig and B. Stadler, Exploring the properties and applications of nanoceria: is there still plenty of room at the bottom?, *Environ. Sci. Nano*, 2014, **1**, 390–405.

145 S. M. Hirst, A. Karakoti, S. Singh, W. Self, R. Tyler, S. Seal and C. M. Reilly, Bio-distribution and in vivo antioxidant effects of cerium oxide nanoparticles in mice., *Environ. Toxicol.*, 2013, **28**, 107–18.

146 A. B. Shcherbakov, N. M. Zholobak, A. E. Baranchikov, A. V Ryabova and V. K. Ivanov, Cerium fluoride nanoparticles protect cells against oxidative stress, *Mater. Sci. Eng. C*, 2015, **50**, 151–159.

147 J. Li, J. Wen, B. Li, W. Li, W. Qiao, J. Shen, W. Jin, X. Jiang, K. W. K. Yeung and P. K. Chu, Valence State Manipulation of Cerium Oxide Nanoparticles on a Titanium Surface for Modulating Cell Fate and Bone Formation, *Adv. Sci.*, 2018, **5**, 1700678.

148 R. J. Forster, P. Bertoncello and T. E. Keyes, Electrogenerated Chemiluminescence, *Annu. Rev. Anal. Chem.*, 2009, **2**, 359–385.

149 E. Kerr, E. H. Doeven, G. J. Barbante, C. F. Hogan, D. J. Bower, P. S. Donnelly, T. U. Connell and P. S. Francis, Annihilation electrogenerated chemiluminescence of mixed metal chelates in solution: modulating emission colour by manipulating the energetics, *Chem. Sci.*, 2015, **6**, 472–479.

150 X. Liu, L. Shi, W. Niu, H. Li and G. Xu, Environmentally Friendly and Highly Sensitive Ruthenium(II) Tris(2,2′-bipyridyl) Electrochemiluminescent System Using 2-(Dibutylamino)ethanol as Co-Reactant, *Angew. Chemie Int. Ed.*, 2007, **46**, 421–424.

151 Y. Yuan, S. Han, L. Hu, S. Parveen and G. Xu, Coreactants of tris(2,2′-

bipyridyl)ruthenium(II) Electrogenerated Chemiluminescence, *Electrochim. Acta*, 2012, **82**, 484–492.

152 W. Miao, J.-P. Choi and A. J. Bard, Electrogenerated Chemiluminescence 69: The Tris(2,2‘-bipyridine)ruthenium(II), (Ru(bpy)$_3^{2+}$)/Tri-n-propylamine (TPrA) System RevisitedA New Route Involving TPrA$^{\bullet+}$ Cation Radicals, *J. Am. Chem. Soc.*, 2002, **124**, 14478–14485.

153 H. Wei, Y. Du, J. Kang and E. Wang, Label free electrochemiluminescence protocol for sensitive DNA detection with a tris(2,2′-bipyridyl)ruthenium(II) modified electrode based on nucleic acid oxidation, *Electrochem. commun.*, 2007, **9**, 1474–1479.

List of Publications

Yuliia Kosto is an author and co-author of the following scientific works:

Kosto, Y., Franchi, S., Matvija, P., Matolínová, I., Prince K. C, Matolín, V., Skála, T., Tsud, N. (2021). Thermal stability of glycine on cerium oxide films of different stoichiometry and composition. *In preparation for Physical Chemistry Chemical Physics.*

Kosto, Y., Zanut, A., Franchi, S., Yakovlev, Y., Khalakhan, I., Matolin, V., Prince, K. C., Valinti, G., Paolucci, F., & Tsud, N. (2019). Electrochemical activity of the polycrystalline cerium oxide films for hydrogen peroxide detection. *Applied Surface Science*, *488*, 351-359.

Lykhach, Y., Kubát, J., Neitzel, A., Tsud, N., Vorokhta, M., Skála, T., Dvořák, F., Kosto, Y., Prince, K. C., Matolín, V., Johánek, V., Mysliveček, J., & Libuda, J. (2019). Charge transfer and spillover phenomena in ceria-supported iridium catalysts: A model study. *The Journal of chemical physics*, *151*(20), 204703.

Kúš, P., Ostroverkh, A., Khalakhan, I., Fiala, R., Kosto, Y., Šmíd, B., Lobko, Y., Yakovlev, Y., Nováková, J., Matolínová, I., & Matolín, V. (2019). Magnetron sputtered thin-film vertically segmented Pt-Ir catalyst supported on TiC for anode side of proton exchange membrane unitized regenerative fuel cells. *International Journal of Hydrogen Energy*, *44*(31), 16087-16098.

Lykhach, Y., Faisal, F., Skála, T., Neitzel, A., Tsud, N., Vorokhta, M., Dvořák, F., Beranová, K., Kosto, Y., Prince, K. C., Matolín, V., & Libuda, J. (2018). Interplay between the metal-support interaction and stability in Pt/Co_3O_4 (111) model catalysts. *Journal of Materials Chemistry A*, *6*(45), 23078-23086.

Leiko, O., Kosto, Y., & Mašek, K. (2018). Structural and photoelectron studies of Sn-SnO_x and SnO_2 nanoparticles on TiO_2 (110) surface. *Surface and Interface Analysis*, *50*(11), 1116-1121.

Ng, S., Krbal, M., Zazpe, R., Prikryl, J., Charvot, J., Dvořák, F., Strizik, L., Slang, S, Sopha, H., Kosto, Y., Matolín, V., Yam, F. K., Bures, F, & Macak, J. M. (2018). $MoSe_xO_y$-Coated 1D TiO_2 Nanotube Layers: Efficient Interface for Light-Driven Applications. *Advanced Materials Interfaces*, *5*(3), 1701146.

List of Tables

List of Abbreviations

AFM - atomic force microscopy

CA - chronoamperometry

CV - cyclic voltammetry

DFT - density functional theory

DOS - density of states

ECL - electrochemiluminescence

GC - glassy carbon

GI - grazing incidence

IMFP - inelastic mean free path

LEED - low energy electron diffraction

LOD – limit of detection

ML - monolayer

MSB - Materials Science Beamline

NEXAFS - near edge X-ray absorption fine structure

NI - normal incidence

NPs - nanoparticles

PBS - phosphate buffered saline

PCa - prostate cancer

PES - photoelectron spectroscopy

PSA - prostate specific antigen

RER - resonant enhancement ratio

RPES - resonant photoelectron spectroscopy

SEM - scanning electron microscopy

SRPES - synchrotron radiation photoelectron spectroscopy

TDS - temperature programmed desorption

TPrA - tripropylamine

UHV - ultra-high vacuum

UPS - ultraviolet photoelectron spectroscopy

VB - valence band

XPS - X-ray photoelectron spectroscopy